

University of Southampton Research Repository
ePrints Soton

Copyright © and Moral Rights for this thesis are retained by the author and/or other copyright owners. A copy can be downloaded for personal non-commercial research or study, without prior permission or charge. This thesis cannot be reproduced or quoted extensively from without first obtaining permission in writing from the copyright holder/s. The content must not be changed in any way or sold commercially in any format or medium without the formal permission of the copyright holders.

When referring to this work, full bibliographic details including the author, title, awarding institution and date of the thesis must be given e.g.

AUTHOR (year of submission) "Full thesis title", University of Southampton, name of the University School or Department, PhD Thesis, pagination

A Contribution to the Jet Noise Installation
Problem

By
Philip Mc Laughlin

A thesis submitted in partial fulfillment for the
degree of Doctor of Philosophy

in the

Faculty of Engineering Science and Mathematics
Institute of Sound and Vibration

December 16, 2010

To My Parents.

Declaration of Authorship

I, Philip Mc Laughlin, declare that this thesis titled, 'A Contribution to the Jet Noise Installation Problem' and the work presented in it are my own. I confirm that:

- This work was done wholly or mainly while in candidature for a research degree at this University.
- Where any part of this thesis has previously been submitted for a degree or any other qualification at this University or any other institution, this has been clearly stated.
- Where I have consulted the published work of others, this is always clearly attributed.
- Where I have quoted from the work of others, the source is always given. With the exception of such quotations, this thesis is entirely my own work.
- I have acknowledged all main sources of help.
- Where the thesis is based on work done by myself jointly with others, I have made clear exactly what was done by others and what I have contributed myself.
- Parts of this work have been published as:

P Mc Laughlin, R H Self, P J R Strange, A Moore. A 3-Dimensional Installation Effect Prediction Method for a Distributed Jet Source. *28th AIAA Aeroacoustics Conference*, 2007.

P. Mc Laughlin, R. H. Self, C. J. Powles, C. Wrighton. High Frequency Jet Noise Installation Effects for an Under Wing Mounted Aircraft. *28th AIAA Aeroacoustics Conference*, 2008.

Signed:

Date:

Abstract

The main objective of this thesis is to understand and predict jet noise installation effects for engines mounted below aircraft wings. This is done through a variety of empirical, analytical and computational methods.

Aspects of the jet source are examined and a jet source model, suitable for determining installation effects is derived.

As part of this research programme a novel and extensive set of model scale jet noise installation effects experiments were undertaken. These results are presented and analyzed in this thesis.

A new semi-empirical method, which can readily predict installation effects for heated coaxial jets is presented and validated using experimental data.

A new 3D ray theory jet propagation method for sources in a steady inhomogeneous moving medium is presented. This method is bench marked using an analytical solution of the Lilley equation. The 3-D method is further enhanced by combining it with realistic CFD jet velocity profiles, and bench marked using the data from the experimental programme.

Acknowledgements

I would like to thank my supervisor Dr. Rod Self for his guidance, patience and occasional enthusiasm provided throughout the duration of this research project. His door was always open and he was always happy to help, for which I will be forever greatful.

I would especially like thank Dr. Christopher Powles for his help, support and advice on a number of technical aspects of this research project. I would also like to thank Dr. Mahdi Azarpeyvand for help and advice with all Jet Noise related queries.

I also thank all my friends and work colleagues at the ISVR with whom I shared the good times, you know who are.

Finally I would like to thank both my parents and my wife, Edel, for the 5 years of love, support and encouragement, without whom this would not have been possible.

Nomenclature

| | |
|--------------------------------|---|
| μ | Fluid viscosity |
| ϕ | Azimuthal angle |
| ψ | Randomly varying phase function |
| ρ | Density |
| SPL | Sound pressure level |
| θ | Polar angle |
| A | Pressure amplitude function, factor of pressure |
| B | Blockage function, Δ SPL |
| b | Blockage function, factor of pressure |
| D | Directivity function, Δ SPL |
| d | Directivity function, factor of pressure |
| D_k | Velocity decay constant - Empirical Constant |
| e_{ij} | Viscous stress tensor |
| H | Heaviside function |
| $J_c = \{u_p, u_s, T_p, T_s\}$ | Jet conditions |

| | |
|-----------|--|
| k | Wavenumber |
| l | The turbulent length scale |
| M_c | Convective Mach number |
| p | Pressure |
| R | Distance traveled along a ray path between source and receiver. |
| r | Jet Radius |
| $r_{1/2}$ | Radial distance from the center line of jet at which the velocity is half of that at the centre line |
| Re | Reynolds Number |
| S_p | Jet spreading rate - Empirical Constant |
| St | Strouhal number |
| T_p | Primary jet temperature |
| T_s | Secondary jet temperature |
| T_{ij} | Lighthill stress tensor |
| U | The mean velocity |
| u | The jet velocity |
| U_j | Jet velocity along the centre line |
| U_p | Primary jet velocity |
| U_s | Secondary jet velocity |
| v | The turbulent velocity |

Contents

| | | |
|----------|---|-----------|
| 1 | Introduction | 1 |
| 1.1 | Thesis outline | 2 |
| 2 | Background and Problem Specification | 3 |
| 2.1 | Aircraft Noise | 3 |
| 2.2 | Noise Level Certification and Standards | 5 |
| 2.3 | Engine Noise Sources | 6 |
| 2.3.1 | Significance of different sources | 7 |
| 2.4 | Installation Effects | 8 |
| 2.5 | Problem Specification | 13 |
| 3 | The Jet Source | 16 |
| 3.1 | Jet Flow | 16 |
| 3.2 | Jet Velocity Profiles | 17 |
| 3.3 | Sound Generated by Flow | 20 |
| 3.3.1 | Lighthill's Acoustic Analogy | 21 |
| 3.3.2 | Jet Scaling | 24 |
| 3.3.3 | Lilley's Equation | 25 |
| 3.4 | Semi-Empirical Jet Noise Models | 25 |
| 3.4.1 | A Coaxial Jet Noise Model | 26 |
| 3.5 | Jet Noise Spectra | 29 |
| 3.6 | Jet Source Directivity | 30 |

| | | |
|----------|--|-----------|
| 3.7 | Jet Source Distribution | 32 |
| 3.8 | An Installations Jet Source Model | 35 |
| 4 | Experimental Programme and Results | 38 |
| 4.1 | Literature Review | 39 |
| 4.2 | Summary of Andante tests | 41 |
| 4.3 | QinetiQ Noise Test Facility | 42 |
| 4.4 | Details of Experimental Hardware | 44 |
| 4.4.1 | Jet Nozzle | 44 |
| 4.4.2 | Microphone Arrays | 44 |
| 4.4.3 | Loudspeakers | 46 |
| 4.4.4 | Flat Plate Wing | 47 |
| 4.5 | Data Processing | 48 |
| 4.6 | Results | 48 |
| 4.6.1 | Experiment 1 - Results | 49 |
| 4.6.2 | Experiment 1 - Discussion | 53 |
| 4.6.3 | Experiment 2 - Results | 55 |
| 4.6.4 | Experiment 2 - Discussion | 59 |
| 4.7 | Conclusions | 59 |
| 5 | A Semi-Empirical Model of Jet Wing Reflection | 61 |
| 5.1 | Introduction | 62 |
| 5.2 | Installations Model | 63 |
| 5.3 | Aircraft Geometry and Reflections | 65 |
| 5.4 | Jet Blockage Model | 67 |
| 5.4.1 | An Empirical Blockage Model | 67 |
| 5.5 | Jet Source Distribution | 74 |
| 5.6 | Jet Source Directivity | 78 |
| 5.7 | Prediction Method Summary | 81 |
| 5.8 | Validation of the Prediction Method | 83 |

| | | |
|----------|---|-----------|
| 5.9 | Further Validation | 91 |
| 5.10 | Conclusions | 92 |
| 6 | Propagation through Jets - Ray Approach | 95 |
| 6.1 | Background to Ray Theory | 96 |
| 6.2 | Acoustic Propagation Through Jets | 97 |
| 6.3 | Rays In a Moving Medium | 99 |
| 6.4 | Ray Equations | 101 |
| 6.5 | Numerical Solution Of Ray Equations | 104 |
| 6.6 | Amplitude Determination | 104 |
| 6.7 | Change in Sound Pressure Level | 105 |
| 6.8 | Multiple Ray Problem | 106 |
| 6.9 | A Two Dimensional Ray Solution | 108 |
| 6.9.1 | Validation of 2D Ray Code | 109 |
| 6.9.2 | A 2D Spreading Jet Velocity Profile | 114 |
| 6.9.3 | Trapped Rays | 115 |
| 6.9.4 | An Infinite Parallel Jet versus Realistic Spreading Jet | 116 |
| 6.10 | A Three Dimensional Ray Solution | 119 |
| 6.10.1 | Launching Rays in 3D | 119 |
| 6.10.2 | Validation of 3D Ray Code | 120 |
| 6.11 | Parallel versus Spreading Jet in 3D | 124 |
| 6.12 | Blockage Model Assumptions | 126 |
| 6.12.1 | Radial variation of the source location | 126 |
| 6.12.2 | Axial variation of the source location | 129 |
| 6.13 | Experimental Validation of ‘rayJet3D’ | 132 |
| 6.13.1 | Jet Profiles | 132 |
| 6.13.2 | Results | 134 |
| 6.14 | Jet Reflection Prediction | 139 |
| 6.15 | Conclusions | 143 |

CONTENTS

| | |
|--------------------------------------|------------|
| 7 Conclusions and Future Work | 145 |
| 7.1 Future Work | 146 |
| A | 148 |
| A.1 ANDANTE Wing | 149 |
| A.2 CFD | 150 |
| A.3 Sensitivity Study | 151 |

List of Figures

| | | |
|-----|--|----|
| 2.1 | Capacity growth without noise increase. Plot courtesy of Air- bus. | 4 |
| 2.2 | Aircraft noise certification reference points. | 5 |
| 2.3 | An identification of the engine components, listing the sub- components of each noise each source. | 6 |
| 2.4 | A breakdown of the noise components of a typical modern aircraft, at take off and at approach. Based on data published by ICAO in 2007. | 8 |
| 2.5 | A380 undercarriage at takeoff. | 9 |
| 2.6 | Graph outlining installation effects. Picture courtesy of Rolls Royce UK. | 13 |
| 2.7 | Diagram outlining the two parts of the of the jet installation effects problem for an under-wing mounted. a) Additional Sources, b) Propagation Effect | 14 |
| 3.1 | Diagram a simple jet flow, highlighting the main regions of the jet flow. | 17 |
| 3.2 | Coordinate system used to describe the jet, θ is the polar angle measured to the downstream jet axis, ϕ is the azimuthal angle measured in the y z plane, were 0 degrees is directly below the jet. | 18 |

LIST OF FIGURES

| | | |
|------|---|----|
| 3.3 | Radial profiles of the mean axial velocity, dashed lines indicate half width [1]. Mean axial velocity against radial distance, for a the same range of downstream axial positions [2] | 19 |
| 3.4 | Single Stream Jet. | 21 |
| 3.5 | Regions of a Coaxial Jet. | 26 |
| 3.6 | Jet Noise Spectra - Single stream, Isothermal, $M = 0.5$. Single stream, Temperature ratio 2.5, $M = 0.5$. Coaxial Jet , Area ratio 4, Temperature ratio 1 (isothermal), Velocity ratio 0.79. Coaxial Jet, Area ratio 4, Temperature ratio 2.8, Velocity ratio 0.79 | 29 |
| 3.7 | Jet Source Directivities- - Single stream, Isothermal, $M = 0.5$. Single stream, Temperature ratio 2.5, $M = 0.5$. Coaxial Jet , Area ratio 4, Temperature ratio 1 (isothermal), Velocity ratio 0.79. Coaxial Jet, Area ratio 4, Temperature ratio 2.8, Velocity ratio 0.79 | 31 |
| 3.8 | Isothermal single stream jet source distribution for a range of frequencies/Strouhal numbers - 2 kHz / 1 St , 5 kHz / 3 St , 10 kHz / 6 St , 20 kHz / 12 St | 33 |
| 3.9 | Heated coaxial jet source distributions for frequencies/Strouhal number - 1kHz / 0.5St , 2kHz / 1St , 10kHz / 5St , 20kHz / 10St | 34 |
| 3.10 | A discretised line source distribution, and an equivalent discretised ring source distribution. | 36 |
| 4.1 | Qinetiq's Noise Test Facility. | 42 |
| 4.2 | Diagram of a 1/16th model scale idealized jet engine nozzle. . | 44 |
| 4.3 | Traversing microphone array at QinetiQ's Noise Test Facility. | 45 |
| 4.4 | Diagram of external source positions. | 46 |
| 4.5 | Diagram of profile of the flat plate wing versus a realistic wing. | 47 |

LIST OF FIGURES

| | | |
|------|---|----|
| 4.6 | Jet Blockage Δ SPL contour maps for Sideline Powered Jet. Each sub-plot represents the source being driven at a different frequency. | 50 |
| 4.7 | Jet Blockage Δ SPL plotted against azimuthal angle, keeping all jet parameters constant while varying Core Temperature. Sub-plots represent polar angles of 90 and 60 degrees, for three separate frequencies. | 51 |
| 4.8 | Jet Blockage Δ SPL plotted against azimuthal angle, rang- ing through realistic jet conditions. Sub-plots represent polar angles of 90 and 60 degrees, for three separate frequencies. . . | 52 |
| 4.9 | Wing Δ SPL contour maps at Sideline Jet Condition. Each sub-plot represents different 1/3 octave band jet source fre- quencies. | 56 |
| 4.10 | Wing Δ SPL plotted against azimuthal angle, comparing lev- els at different jet condition, for three low frequencies, at polar angles of 90 and 60 degrees. | 57 |
| 4.11 | Wing Δ SPL plotted against azimuthal angle, comparing lev- els at different jet condition, for three high frequencies, at polar angles of 90 and 60 degrees. | 58 |
| 5.1 | Ray paths of sources which are reflected from surface/wing. . | 63 |
| 5.2 | Wing geometry is represented by a number of quadrilateral finite surfaces, each represented in the model by its four ver- tices. The flat plate wing used in the ANDANTE tests can be represented by two quadrilaterals. | 65 |
| 5.3 | The above diagram illustrates how the method determines if a reflection from a finite panel, for a particular source has reached an observer. | 66 |

LIST OF FIGURES

| | | |
|------|--|----|
| 5.4 | Jet blockage data and fitted curves for 10kHz(model scale) external source for a high powered jet. Δ SPL is plotted against azimuthal angle in degrees, where zero degrees is directly below the jet. | 69 |
| 5.5 | Empirical Hot Jet Blockage Map and Surface Plot for 10kHz(model scale) external source for a jet at realistic operating conditions, generated from curves in figure 5.4. | 70 |
| 5.6 | Diagram outlining angles used to scale jet blockage data. ϕ is any azimuthal angle, and ϕ_G is the angle of a ray at grazing incidence to the core. | 71 |
| 5.7 | Diagram demonstrating how the blockage is scaled. A) Measured blockage data B) Estimated blockage for increased jet radius C) Estimated blockage for change of source position. . . | 73 |
| 5.8 | Measured jet source distributions, at conditions Approach and Cutback, measured using polar correlation technique. . . | 75 |
| 5.9 | Measured jet source distributions, for a range of six Strouhal numbers. | 77 |
| 5.10 | Jet source directivity at Approach condition, measured on polar array during ANDANTE tests, normalised using the source strength at polar angle 90°. | 79 |
| 5.11 | Jet source directivity at cutback condition, measured on polar array during ANDANTE tests, normalised using the source strength at polar angle 90°. | 80 |
| 5.12 | OASPL jet source directivities at Approach, Intermediate and Cutback, and interpolated Intermediate prediction. | 80 |
| 5.13 | Flow diagram, outlining the primary survey used in the Fortran 90 prediction method. | 82 |

LIST OF FIGURES

| | |
|---|----|
| 5.14 Approach Jet condition at 792Hz, comparison of a prediction verses measured data, Δ SPL is plotted against azimuthal an- gle for a range of six polar angles. | 85 |
| 5.15 Approach Jet condition at 2.5kHz, comparison of a predic- tion verses measured data, Δ SPL is plotted against azimuthal angle for a range of six polar angles. | 85 |
| 5.16 Approach Jet condition at 5kHz, comparison of a prediction verses measured data, Δ SPL is plotted against azimuthal an- gle for a range of six polar angles. | 86 |
| 5.17 Approach Jet condition at 12.5kHz, comparison of a predic- tion verses measured data, Δ SPL is plotted against azimuthal angle for a range of six polar angles. | 86 |
| 5.18 Approach Jet condition at 15kHz, comparison of a prediction verses measured data, Δ SPL is plotted against azimuthal an- gle for a range of six polar angles. | 87 |
| 5.19 Approach Jet condition at 25kHz, comparison of a prediction verses measured data, Δ SPL is plotted against azimuthal an- gle for a range of six polar angles. | 87 |
| 5.20 Sideline Jet condition at 792Hz, comparison of a prediction verses measured data, Δ SPL is plotted against azimuthal an- gle for a range of six polar angles. | 88 |
| 5.21 Sideline Jet condition at 2.5kHz, comparison of a prediction verses measured data, Δ SPL is plotted against azimuthal an- gle for a range of six polar angles. | 88 |
| 5.22 Sideline Jet condition at 5kHz, comparison of a prediction verses measured data, Δ SPL is plotted against azimuthal an- gle for a range of six polar angles. | 89 |

LIST OF FIGURES

| | |
|---|-----|
| 5.23 Sideline Jet condition at 12.5kHz, comparison of a prediction verses measured data, Δ SPL is plotted against azimuthal an- gle for a range of six polar angles. | 89 |
| 5.24 Sideline Jet condition at 15kHz, comparison of a prediction verses measured data, Δ SPL is plotted against azimuthal an- gle for a range of six polar angles. | 90 |
| 5.25 Sideline Jet condition at 25kHz, comparison of a prediction verses measured data, Δ SPL is plotted against azimuthal an- gle for a range of six polar angles. | 90 |
| 5.26 Using a new data set - a comparison of prediction verses mea- sured, Δ SPL is plotted for a single microphone, at 90 degrees polar angle, and 60 degrees azimuthal angle, for a range fre- quencies. | 91 |
| 5.27 Using a new data set - a comparison of predicted verses mea- sured, Δ SPL is plotted against azimuthal angle for four differ- ent model scale frequencies, equivalent full scale frequencies are 111Hz, 277Hz, 555Hz, and 1.1kHz respectively. | 93 |
| 6.1 Contour plot of jet sound speed profile. | 107 |
| 6.2 Rays traced through sound speed profile, demonstrating mul- tiple rays turning up in a location. | 108 |
| 6.3 Source in parallel shear flow. | 109 |
| 6.4 Jet Velocity plotted using the error function profile, for two different shear layer thicknesses, $\delta = 1.0$ and $\delta = 0.2$ | 110 |
| 6.5 Validation of the 2D ray code using Lilley Solver, for six listed test cases, see table 6.1. Plotted for polar angles above and below the jet, where sources off the radius are above the jet. . | 113 |
| 6.6 2D Jet Velocity profile for a single stream, Isothermal $M=0.6$. jet, generated using equation 6.37 a function fitted to a RANS CFD prediction. a) Contour Plot b) Color Map. | 114 |

LIST OF FIGURES

| | | |
|------|--|-----|
| 6.7 | Rays traced from source at end of the potential core. At certain angle rays become trapped by the velocity profile. . . | 116 |
| 6.8 | Jet source positions for infinite versus spreading jet investigation, 0D, 4D, 8D, 12D, 16D, and 20D respectively. | 116 |
| 6.9 | Parallel versus spreading jet plots. In each sub-plot Δ SPL is plotted against polar angle for the six different source positions. | 118 |
| 6.10 | An icosahedron can accurately tessellate a sphere, by recursively sub-dividing each of the faces. | 120 |
| 6.11 | An example of the five neighbour aberrations on a geodesic sphere, generated by sub-dividing an icosahedron 3 times to give geodesic sphere with 642 vertices. | 121 |
| 6.12 | Surface plots using Ray Code and Lilley Solver. Comparison of the two solutions for a source $2D_j$ above an isothermal jet. . | 123 |
| 6.13 | Validation of the 3D ray solver. Delta SPL is plotted against polar angle, for a range of four azimuthal angle. Comparison of the two solutions for a source 2D above an isothermal jet. . | 123 |
| 6.14 | Comparison of Δ SPL of a parallel versus spreading Mach 0.8 jet, for a point source one nozzle diameter above the jet, 3 diameters downstream from the nozzle. | 125 |
| 6.15 | Test of data scaling factor for sources at fixed axial location with source 1, 2, and 3 at radial distances of 2, 3 and 4 nozzle diameters from the jet axis. Δ SPL is plotted against azimuthal angle for a range of 3 polar angles. | 128 |
| 6.16 | Comparison of Δ SPL of spreading jet, for a point source at $1D_j$ above the jet for a range of axial position(1,2,3 and $4D_j$). . | 131 |
| 6.17 | CFD for isothermal short cowl nozzle with VR 1.0. | 132 |
| 6.18 | Velocity profile from CFD for sideline jet condition with short cowl nozzle, VR = 0.7. | 133 |

LIST OF FIGURES

| | | |
|------|---|-----|
| 6.19 | Temperature profile from CFD for sideline jet condition with short cowl nozzle, TR=4.0. | 134 |
| 6.20 | Comparison of ‘rayJet3D’ with data from ANDANTE experiment 1, for ‘Isothermal’ Jet. | 136 |
| 6.21 | Comparison of ‘rayJet3D’ with data from ANDANTE experiment 1, for ‘Intermediate’ Jet. | 137 |
| 6.22 | Comparison of ‘rayJet3D’ with data from ANDANTE experiment 1, for ‘Sideline’ Jet. | 138 |
| 6.23 | Installation predictions with a ‘rayJet3D’ blockage model and an empirical blockage model compared with data from ANDANTE experiment 2, for ‘Intermediate’ Jet. | 141 |
| 6.24 | Installation predictions with a ‘rayJet3D’ blockage model and an empirical blockage model compared with data from ANDANTE experiment 2, for ‘Sideline’ Jet. | 142 |
| A.1 | Schematic of Flat Plate Wing manufactured for and used in the Andante Installations Tests. | 149 |
| A.2 | Short Cowl Nozzle used for CFD. | 150 |
| A.3 | Grid on which CFD data is projected onto. | 150 |
| A.4 | Example of convergence for a ring source distribution. | 152 |
| A.5 | Example of convergence for a line source distribution. | 152 |

List of Tables

| | | |
|-----|--|-----|
| 3.1 | Empirical Constants for spreading jet rate S and velocity-decay constant B | 20 |
| 4.1 | ANDANTE Jet Nozzle dimensions. | 44 |
| 4.2 | Jet Conditions used in model scale ANDANTE experiments. | 48 |
| 6.1 | Set of Test case Jet Conditions, used to validate the 2D ray code | 110 |

Chapter 1

Introduction

Aircraft engine noise is often assessed by measuring the noise in isolation from the aircraft. This can be done at full scale such as on an engine test bed or at model scale when individual engine components are tested, for example in a jet noise test facility. However measured flight data is significantly different from the simple combination of the noise from the isolated components. These changes arise for a number of reasons such as reflection of sound energy from and screening by the airframe, blockage of reflections by the jet, and various surface interaction effects. Collectively these effects are known as *installation effects* and their understanding and prediction represent an important problem in aeroacoustics.

This thesis presents a study on aspects of the jet noise installation problem. The project arose as aircraft and aircraft engine manufacturers had the requirement to understand and have the capability to quantify these effects. A number of approaches to aspects of this problem are presented in this thesis. Experimental data is examined, a semi-empirical prediction tool is developed and numerical ray tracing method to quantify refraction by the jet is presented. In the following section is an outline of the thesis highlighting key results and the original contribution of this work.

1.1 Thesis outline

In the following Chapter information on aspects of aircraft noise, putting the jet noise installation problem in context, are presented. Jet noise installation effects literature is reviewed and the installation effects problem is formulated.

In the following Chapter the jet source is examined. Some background theory on jet flow is presented. The reader is reminded of the fundamental concept of noise generation by jets, with the key results of Lighthill's Acoustic Analogy and Lilley's equation being outlined. Time is taken to discuss the jet noise source distribution and source directivity, as these two elements of the source will play a pivotal role in determining the installation effects. The first novel aspect of this work is presented; a jet source model, suitable for determining installation effects is derived.

In Chapter 3 previous experimental work quantifying jet noise installation effects is reviewed and discussed critically. The review highlights a number of shortcomings of the previous work. In addition a new set of model scale jet noise installation effects experiments designed to overcome the shortcoming of the previous work are described.

In Chapter 4 we develop a new fast and robust engineering tool, which can readily predict installation effects for heated coaxial jets installed under a realistic aircraft wing with the jet operating at realistic flight conditions. The model is developed and validated using the experimental data.

In Chapter 5 a new 3D ray theory jet propagation method for sources in a steady inhomogeneous moving medium is presented. This method is validated for a parallel sheared flow. We use a CFD isothermal jet profile to investigate the significance of the parallel jet assumption, and assess the spreading jet effects on the cone of silence effects.

Finally, in Chapter 6, a number of conclusions relating to the work are drawn and ideas for future developments of the work are presented.

Chapter 2

Background and Problem Specification

This chapter presents background information on aspects of aircraft noise putting the jet noise installation problem in context. Jet noise installation effects literature is reviewed and the installation effects problem is formulated.

2.1 Aircraft Noise

Aircraft cause a significant amount of environmental noise pollution. With an ever increasing number of people demanding to fly comes the expansion of airports and an increase in the number of aircraft in our skies. Thus reducing or limiting the effect of aircraft noise on communities is a major priority for aircraft manufacturers and aviation authorities alike.

The noise emanating from aircraft in and around an airport depends on a number of factors including: the type of aircraft, the number of flights, operating conditions, time of day, type of runway, weather condition, topography and airport specific flight procedures etc.

Significant progress in aircraft noise reduction has already been made

to date with current aircraft coming off the production line are about 75% quieter than they were forty years ago [3]. Figure 2.1 compares two previous generations of A340 with a new A380 jumbo aircraft, it shows the effective perceived noise (EPN) for each aircraft along with the potential weight written on each bar. It helps provide an illustration of how technological advances in noise efficiency can allow us to increase the number of passengers being transported without having a negative effect on the EPN level.

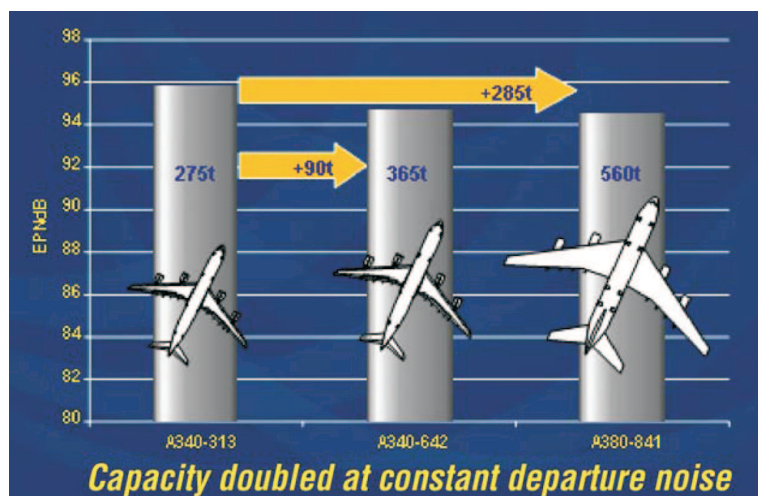


Figure 2.1 – Capacity growth without noise increase. Plot courtesy of Airbus.

The noise produced by aircraft is caused by both the airframe and the engine. A turbofan engine sucks in air and it is exhausted at a high velocity creating noise. The airframe generates noise as it moves through the air, the main causes of which are the high lift devices and landing gear. Modern trends in engine design have led to higher bypass ratios, which has meant great reductions in engine noise, and airframe noise has become more of a significant noise source in recent times. However engine noise is still a dominant aircraft noise source. A more detailed break down the different engine noise source components is given in section 2.3.

2.2 Noise Level Certification and Standards

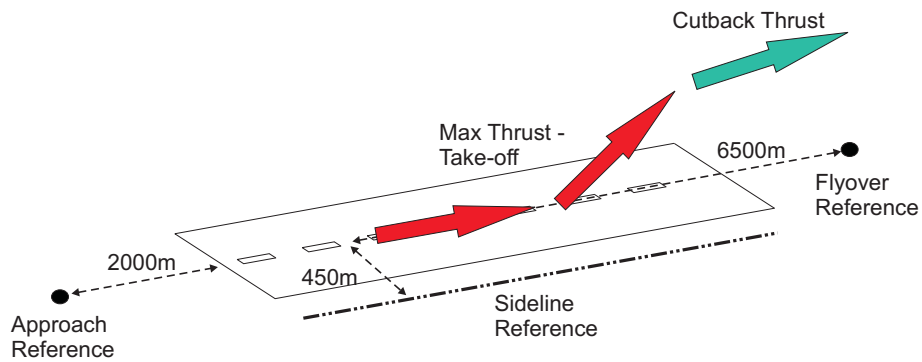


Figure 2.2 – Aircraft noise certification reference points.

Since the 1960s the International Civil Aviation Organization (ICAO) has been addressing the issue of aircraft noise levels and the first standards and recommended practices for aircraft noise certification were published in 1971. Since then they have been updated and developed to reflect improvements in technology. There are four adopted approaches to aircraft noise management: reduction of noise at the source; land-use planning and management; noise abatement operational procedures; and operating restrictions.

To encourage noise reduction at source ICAO has introduced standard noise certification positions. The three certification positions can be seen in figure 2.2. Fly-over is 6.5 km from the brake release point, under the take-off flight path. Sideline is a noise measurement recorded at a point 450m from the runway axis during takeoff. Approach is 2km from the runway threshold, under the approach flight path.

The large coloured arrows in figure 2.2 show the flight path of a plane taking off. The engines operate at full power along the runway and during the first stage of ascent, until a minimum safe altitude has been reached. This is why measurements made at the sideline position are usually the highest levels. The aircraft can then continue to climb at a lower thrust

setting, known as cutback. The cutback engine condition is used to help alleviate noise levels at the flyover reference point.

2.3 Engine Noise Sources

A modern turbofan has a number of different noise generating components, each generating different types of noise. A cutaway diagram of a typical turbofan is shown in figure 2.3. The different noise generating components are pointed out, and the type of associated noises are listed.

Engine Noise Source Components

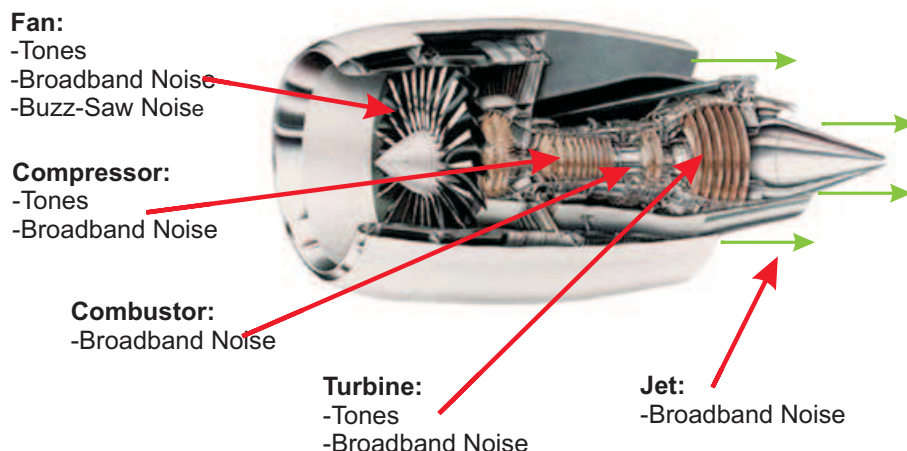


Figure 2.3 – An identification of the engine components, listing the sub-components of each noise each source.

Rotating machinery will generate noise, i.e. the fan compressor and turbine. This noise has both tonal and broadband characteristics.

The rotating fan has a number of associated noise generating mechanisms. Tones, which are both low and high frequency, are generated when there is an interactive effect between airflow perturbations in the path of rotating blade. The tones occur at multiples of the Blade Passage Frequency (BPF) and depend upon the number of rotor blades and the number of stator vanes.

At supersonic tip speeds, the tones occur at harmonics of the shaft rotation frequency and is called buzz-saw noise. Buzz-saw saw noise occurs when the relative speed of the inlet flow impinging on the fan blades is supersonic, this creates shocks, resulting in a noise like a chainsaw.

Fans produce broadband noise due to pressure fluctuations associated with turbulent flow near the surface of the blades. Three principal mechanisms of fan broadband noise have been identified [4] [5] as, rotor wake and stator interaction noise, rotor blade and boundary layer interacting with the trailing edge flow noise and inlet boundary layer turbulence-rotor tip interaction noise.

The exhaust flow or jet at the rear of the engine creates a broadband source due to the jet mixing process. Supersonic jets also have associated shock noise, however most civil aircraft today have sub-sonic jet, so shock noise not a major consideration.

Few other engine sources are relevant in the overall noise picture. Some sources which merit consideration at certain times in the flight cycle include; bleed valves that off load high-pressure from the compressor into the bypass duct, internal aerodynamic devices like exhaust mixers, and rough surfaces of acoustically absorbent liners that are introduced to suppress noise can become additional noise sources.

Different sources tend to dominant at different times in the flight cycle. In the next section we look at noise source component levels at takeoff and approach.

2.3.1 Significance of different sources

Figure 2.4 shows the relative EPN levels of the noise components of a typical modern turbofan aircraft at both take off and approach. The levels are based on measured flight data from ICAO. As can be seen from the plots the engine is the most significant noise source at both approach and take off. It is also

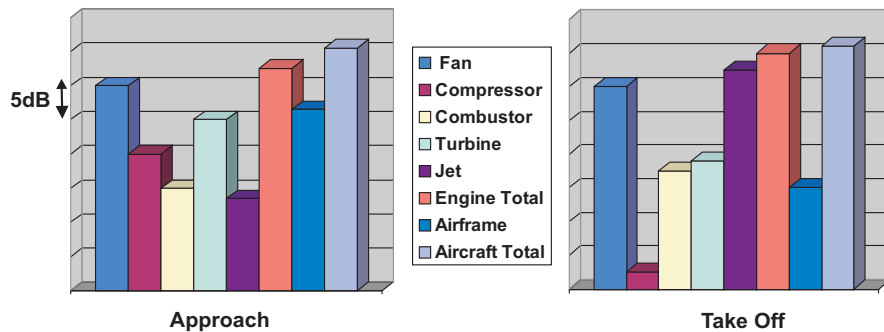


Figure 2.4 – A breakdown of the noise components of a typical modern aircraft, at take off and at approach. Based on data published by ICAO in 2007.

clear that of the different engine noise source components, the jet source is the most dominant source at take off. So understanding and predicting jet noise is an important aspect of aircraft overall noise prediction.

The noise source levels in figure 2.4 breakdown are based on measured flight data. Of course installed in flight data can be significantly different to an isolated engine source data as was explained above. Although a lot of work has been done trying to quantify and predict isolated jet noise, much less work has been done trying to quantify the installed jet noise levels. In the following section we review existing installations effects literature.

2.4 Installation Effects

When an engine is installed on an aircraft structure, many additional noise effects are introduced. Figure 2.5 shows a picture of the under carriage of an Airbus A380 taking off. As can be seen from the photo the four turbofan engines are installed on the underside of the leading edges of the wings. All engine sources will incur a degree of installation and flight effects, but particularly sources coming from the rear of the engine, as they can reflect from the wing and flaps.

The jet source itself is a distributed source, and due to installation, a large portion of the jet is positioned directly below the wing, meaning the



Figure 2.5 – A380 undercarriage at takeoff.

noise can be reflected to observers on the ground. Furthermore, the close proximity of the wing means that the jet source can be modified and new sources can be introduced (especially when the flaps are deployed).

The first work quantifying jet noise installation effects was published in the 1970s and the problem of significantly different installed levels was first identified by Bushell [6]. He noted that exhaust noise does not reduce in going from static to in flight conditions in line with predictions for the behavior of the jet. It was also noted by Szewczyk [7] in 1979, in a paper called Coaxial Jet Noise in Flight, that installation effects account for the differences between model simulation and flight data.

However it wasn't until 1980 that Way and Turner [8] published results, from model scale tests, which actually quantified the effects of installing a jet underneath a wing. Way and Turner measured the change in SPL due to the installation of a realistic wing above a coaxial jet using microphones positioned at different polar angles to the jet. It was noted that the measured levels of reflected jet noise were notably less than the expected 3dB, and this was likely to be due to the attenuation of the reflected signals propagating through the jet exhaust. At very low frequencies they noted large increases

in installed levels, which they attributed to an interaction between the jet and wing. Fortunately these effects are below noise certification levels at full scale frequencies. More importantly however, these effects did not correlate with equivalent single stream jet wing interaction noise levels, highlighting the importance of testing with a realistic coaxial jet [8].

Way and Turner also carried out a series of jet flap interaction tests, which involved comparing isolated jet levels with installed levels, where the wing included a flap impinged by the jet. They noted large increased levels in frequencies less than 400Hz at full scale.

Another early paper quantifying installed levels is that of Wang [9]. In this paper an idealised flat plate wing is placed above a single stream jet, and measurements were made on both a polar array directly below the jet, in the flyover plane, and an azimuthal array downstream of the jet, to take sideline readings. The results published generally agree with those of Way and Turner. Wang noted that installation effects can increase sideline levels, and that the low frequency jet wing interaction effects are at too low a frequency at full scale to be a significant source of annoyance.

A series of model scale tests to measure installed jet noise were published by Shivashankara and Blackner [10] in 1997. These tests involved a 1/20th scale full aircraft geometry in a flight stream above a heated coaxial jet. Installed jet noise levels were measured with an azimuthal array, and an acoustic mirror was used to determine source location. The authors noted that the presence of the airplane increases the jet noise levels, more so for the inboard engine than the outboard engine. They also commented on how the presence of the wing and the pylon supporting the wing can change the shape of the jet flow so that it is no longer axi-symmetric. The wing is thought to particularly effect the shape of the secondary shear layer, which generates much of the noise which is reflected from the wing.

An extensive published programme of model scale experiments measur-

ing installation effects on jet noise is that of Mead and Strange [11]. They measured the change in sound levels of a model engine exhaust due to the placing a number of different wing geometries above it, using a azimuthal microphone array. They noted a 2dB increase at higher frequency jet noise levels and an increase of up to 9 dB at the lowest frequencies. Most of tests were carried out at static conditions; however they also used a flight stream for some tests to simulate flight conditions. They noted that the flight stream did not effect the reflected higher frequency installed noise levels however it tended to alleviate the lower frequency jet wing interaction noise.

Although there have been a number of published papers based on measuring jet noise installation effects, there are few publications suggesting how to predict or model installation effects. Two such papers by Moore [12] and Moore and Mead [13] outline a method for predicting wing reflections of nozzle based sources. They present a 3-D ray-theory model, were a point source with an empirically prescribed directivity and strength, based on far field measurements, can represent any nozzle based source. The aircraft geometry, primarily the wing and flaps, is represented by a number of finite flat surfaces. The prediction method also includes a 2-D semi-empirical hot jet blockage model. Moore concludes that even an axisymmetric rear-arc source can produce highly non-axisymmetric installed directivity, and that the inclusion of the acoustic blockage by the hot jet is essential in any prediction of under wing reflection.

More recently there have been a number of papers investigating the engine installation effects for more novel aircraft geometries. A NASA publication by Berton [14] investigates the noise reduction potential of over wing mounted turbofans. Berton combined an existing full aircraft noise prediction scheme with an asymptotic method developed in optics to calculate the diffracted field of the shielded engines sources, to make predictions for the

novel aircraft geometry. Results suggested that over wing mounting a modern turbofan could achieve significant reductions in the total engine noise source, and avoid additional high frequency reflection incurred by mounting under the wing.

Chappuis et al. [15] present a paper on aft fan noise shielding by a wing. They present an analytical diffraction model based on diffraction by a semi-infinite plate. They highlight the importance of accurate source modeling, and by representing an aft fan modal source with a combination of monopole sources with predetermined phase difference, they show a marked improvement on simply using a single monopole source. The analytic model is compared with numerical (BEM) and experimental results, and gives reasonable agreement. The analytic model requires understanding of the source directivity, and assumes that the wing is a flat plate.

A more novel concept again is the so called blended wing body (BWB), a modern aircraft geometry concept designed to minimise the surface area per passenger for efficiency, with above body embedded high pass ratio engines for reduced noise. The first published experimental acoustic study on the BWB concept is that of Clark and Gerhold [16]. In this paper they measured the shielding effect using a model scale BWB aircraft with a compact source above the BWB, representing an aft fan source. They concluded that the BWB could reduce aft fan noise by up to 20dB in the forward arc, and 10dB in the rear arc. This preliminary work was followed up in a second paper by Gerhold and Clark et al. [17]. In this paper they develop a computational model to predict the shielding by the BWB. They use a boundary element method, which predicts the incident field due to a point source in a nacelle, combined with a equivalent source method, which determines the field scattered from the BWB. This captures the major features of an aft fan source above a BWB, which they then compare with more model scale experimental results. The experimental and computational results agree in

the overall shielding characteristics, and in some of the finer detail of the scattering from the structure. However, the results are limited to low frequencies due to computational power, and even though the geometry was kept relatively simple computation was slow.

Agarwal et al. [18] published a ray-tracing approach to calculate acoustic shielding by a BWB. In this paper the authors represent the forward propagating noise from the engine intake as a point source, using ray theory to calculate the scattered field. The model accounts for the field in the shadow zone using geometric theory of diffraction to calculate both edge diffracted and creeping rays. The method is validated using model scale experimental results, and numerical boundary element results.

2.5 Problem Specification

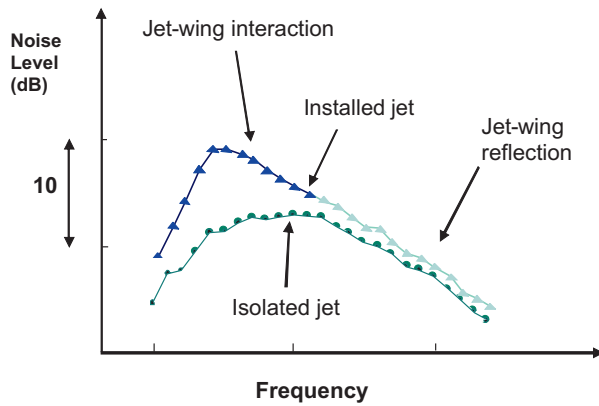


Figure 2.6 – Graph outlining installation effects. Picture courtesy of Rolls Royce UK.

Although all engine sources will exhibit installation effects to some extent, the focus of the work in this thesis concerns predicting and understanding the installation effects on jet mixing noise for a under-wing mounted engine. Figure 2.6 helps give us an appreciation of the problem. The lower line represents an isolated jet noise spectrum. The line above represents an installed jet noise spectrum. Regions of the installed jet noise levels have

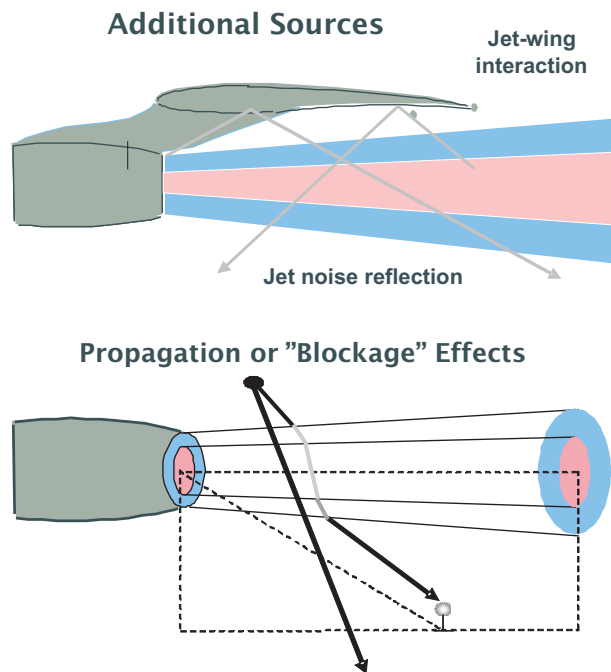


Figure 2.7 – Diagram outlining the two parts of the jet installation effects problem for an under-wing mounted. a) Additional Sources, b) Propagation Effect

been coloured to represent what is believed to be the dominant effect in those regions. As can be seen from the graph, at lower frequencies the dominant effect is what is known as “jet-wing interaction”, whereas at higher frequencies the dominant effect is considered to be jet wing reflection. The jet source is an axially distributed frequency dependent source, which is generally conceived to consist of a distribution of quadrupole sources. At high frequencies the majority of the source is concentrated close to the nozzle, i.e. under the wing, so reflections from the wing dominate. At lower frequencies the source is much more distributed and further down stream, thus less of the source is reflected. However, the lower frequency sources are caused by large scale turbulent structures within the jet, which interact with the wing, particularly the trailing edge, generating new low frequency sources. These new low frequency jet-wing interaction sources are thought to be caused by the wing surface (particularly the trailing edge of the wing) converting the

jet quadrupole sources to more efficiently radiating dipole sources.

Figure 2.7 helps give an appreciation for the jet noise installation effects problem for engines mounted beneath a wing. The problem can be divided into to separate parts, the additional sources problem and the propagation or jet blockage problem. The additional source include the portion of the jet reflected from the wing and the low frequency jet wing interaction effect. The low frequency interaction effect is only observed at the very lowest audible frequencies at full scale and is not the focus of this thesis, however it is something which is considered particularly when dealing with model scale data.

Chapter 3

The Jet Source

In this chapter we examine the jet source in more detail to gain a better understanding of the specific source with which we are concerned. We begin by defining what we mean by a jet, and cover some background theory on jet flow. The reader is reminded of the fundamental concept of noise generation by jets, with the key results of Lighthill's Acoustic Analogy and Lilley's equation being outlined. Time is taken to discuss the jet noise source distribution and source directivity, as these two elements of the source will play a pivotal role in determining the installation effects. Temperature effects on the jet source are discussed. A simple jet source model, suitable for determining installation effects is outlined.

3.1 Jet Flow

The simplest example of a jet is the discharge of a fluid with a uniform initial velocity field into a homogeneous medium with a constant velocity, see figure 3.1. Initially the boundary layer between the two fluids has zero thickness, however the instability of the separation causes eddies to form in the boundary layer which move in a disorderly fashion across the streams. This brings about an exchange of fluid between the jet and the ambient

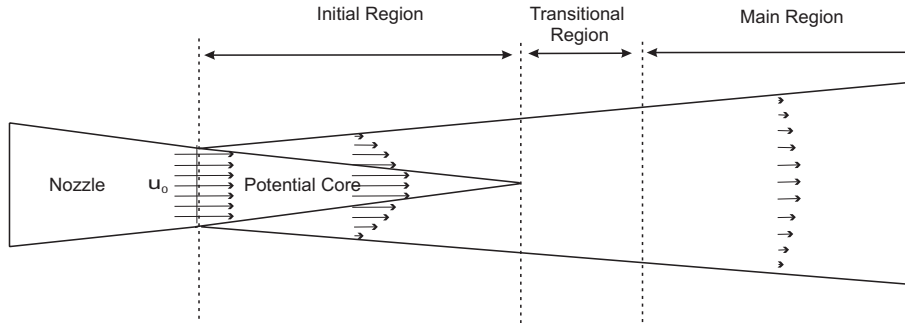


Figure 3.1 – Diagram a simple jet flow, highlighting the main regions of the jet flow.

medium. Thus a transverse transfer of fluid properties, i.e. momentum and heat. The potential core is a an initial region of parallel flow. The region between the potential core and ambient fluid, of sheared flow, is termed the turbulent boundary layer or shear layer.

Moving downstream the width of turbulent boundary layer increases, effectively causing the jet to widen or spread, but also causing the gradual mixing of the non viscous core - the region of potential flow between the two boundary layers. The names given to the different region of the jet flow are outlined in figure 3.1.

3.2 Jet Velocity Profiles

In a turbulent jet the components of velocity at any point can be decomposed into a time averaged or mean value component, plus a randomly varying or fluctuating component corresponding to the turbulent velocity:

$$u_i = \bar{U}_i + v_i, \quad (3.1)$$

where the fluctuating components can be averaged over some finite time interval making them equal zero:

$$\bar{v}_i = 0, \quad (3.2)$$

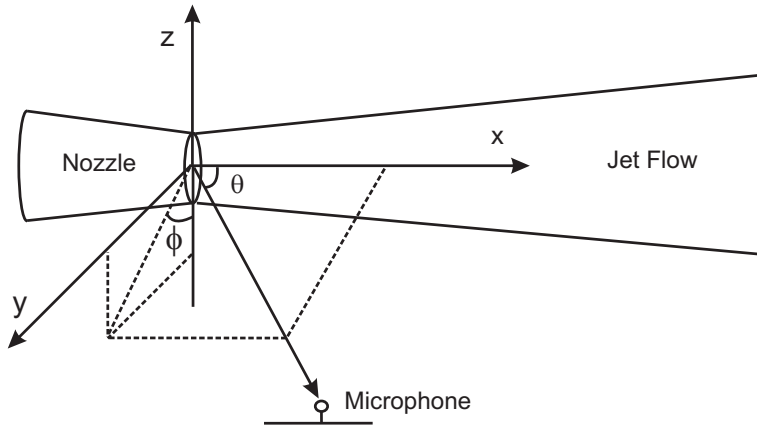


Figure 3.2 – Coordinate system used to describe the jet, θ is the polar angle measured to the downstream jet axis, ϕ is the azimuthal angle measured in the y z plane, were 0 degrees is directly below the jet.

$$\bar{u}_i = U_i. \quad (3.3)$$

If the mean free path of a fluid particle (mixing length) in a turbulent stream is l , when moved in a transverse direction the particle reaches a layer in which the mean velocity has changed,

$$\Delta U_y = l \frac{\partial U_y}{\partial y}. \quad (3.4)$$

As the fluid particle moves it merges with the mass of the new layer it moves into, which results in a discontinuous variation in the velocity

$$v_y = \Delta U_y. \quad (3.5)$$

Thus perturbations of the stream wise velocity components are of order

$$v_y \approx l \frac{\partial U_y}{\partial y}. \quad (3.6)$$

It is usually assumed that the transverse perturbations in velocity are proportional to the stream wise perturbations, but have opposite sign, i.e.

$$-v_x \approx l \frac{\partial U_y}{\partial y}. \quad (3.7)$$

Prandtl [19] assumed that the mixing length at any cross section of the stream was constant, i.e.

$$l(y) = \text{const.} \quad (3.8)$$

The variation in the mixing length along the jet axis can be established by experimental means. It has been shown [20] that beyond the potential core, in the developing region of the jet

$$\frac{U}{U_0} = f\left(\frac{r}{r_{1/2}}\right) \quad (3.9)$$

where U_0 is the velocity at the centre line of the jet, and $r_{1/2}$ is the radial distance from the centre line of jet at which the velocity is half of that at the centre line, see figure 3.3. The important conclusion is that the mean velocity profile is self-similar and that the jet exhibits this self-similar behavior, to within a good approximation, over a range of axial locations.

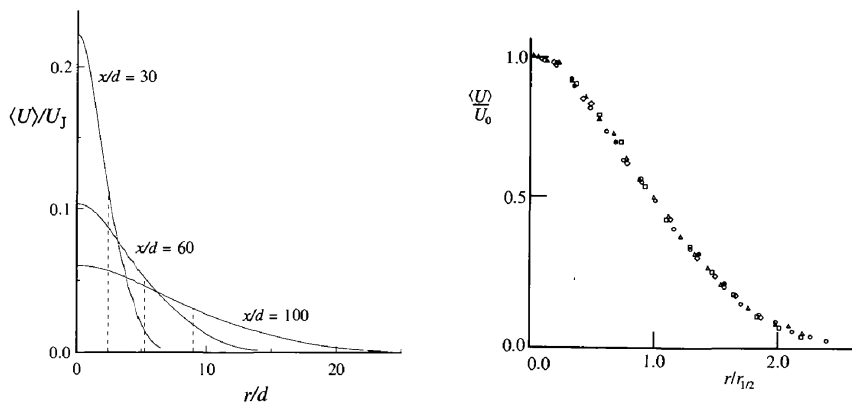


Figure 3.3 – Radial profiles of the mean axial velocity, dashed lines indicate half width [1]. Mean axial velocity against radial distance, for the same range of downstream axial positions [2]

| | Panchapakesan and Lumley [21] | Hussein et al [1], hot wire data | Hussein et al [1], laser-Doppler data |
|----|-------------------------------|----------------------------------|---------------------------------------|
| Re | 11000 | 95500 | 95500 |
| Sp | 0.096 | 0.102 | 0.094 |
| Dk | 6.06 | 5.9 | 5.8 |

Table 3.1 – Empirical Constants for spreading jet rate S and velocity-decay constant B

Experiments show that downstream of the potential core, the velocity along the jet axis can be approximated to

$$\frac{U_0}{U_j} = \frac{D_k}{x/d}, \quad (3.10)$$

where D_k is an empirically defined constant. Similarly the jet spreading rate

$$S_p = \frac{dr_{1/2}}{dx}, \quad (3.11)$$

where S_p is an empirical constants, see Table 3.1. We can see from the results that the velocity decay constant, D_k , and the jet spreading rate, S_p , are independent of the Reynolds number, Re . The Reynolds number can effect the flow - small scale turbulent structures are smaller at high Reynolds numbers. However, Reynolds number does not effect the mean velocity or jet spreading rate. $S_p = 0.1$ gives a jet spreading angle of about 6 degrees.

3.3 Sound Generated by Flow

Much of the noise created by a single stream jet comes from the mixing process between the exhaust flow of the engine and the atmosphere. Figure 3.4 represents a cross section of a single stream jet, outlining the main features. The potential core is a region of parallel flow, with velocity equivalent to that at the nozzle exit. As core flow is parallel it has very low turbulence intensity, thus it doesn't generate much noise. The layer between the core

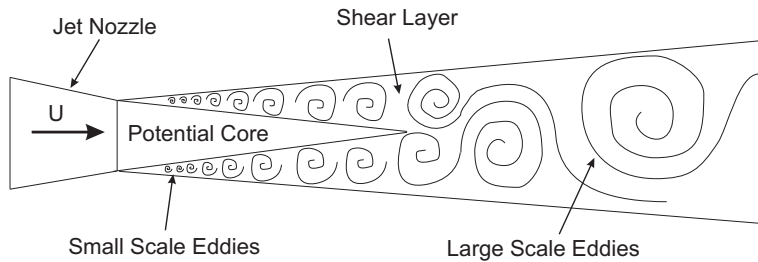


Figure 3.4 – Single Stream Jet.

and the atmosphere is a sheared flow, known as the shear layer. This has a high turbulence intensity, and generates much of the noise associated with sub-sonic single stream jets. Pressure fluctuations occur in an unsteady flow to balance the fluctuations in momentum. Some of these fluctuations will propagate outward from their source and be recognized as sound, and it is these fluctuations with which we are concerned.

The size of the turbulent structures or eddies in the shear layer are related to the frequency of the noise generated. The higher frequency broadband sources are generated by the small scale turbulent structures near the jet nozzle, while the lower frequency broadband sources are generated by the larger scale turbulent structures downstream of the nozzle.

3.3.1 Lighthill's Acoustic Analogy

It was Lighthill, in 1952, who first derived an equation to describe flow generated acoustic pressure fluctuations. Lighthill's acoustic analogy forms the basis of aeroacoustics. It was introduced to solve the problem of jet noise, but it can be applied to calculate acoustic radiation from any small turbulent flow region, embedded in an infinite homogeneous fluid.

Realizing that the pressure fluctuations in the farfield behave like acoustic waves, Lighthill combined the equations of continuity and momentum for a turbulent flow, and rearranged them so as to give a homogeneous wave equation at large distances from the turbulent flow. The derivation is as

follows: the equations of continuity and momentum are

$$\frac{\partial \rho}{\partial t} + \frac{\partial}{\partial x_j} \rho u_j = 0 \quad (3.12)$$

$$\frac{\partial}{\partial t} \rho u_i + \frac{\partial}{\partial x_j} (\rho u_i u_j + \delta_{ij} p - e_{ij}) = 0, \quad (3.13)$$

where e_{ij} denotes the viscous stress tensor, which can be expressed in terms of a velocity gradient

$$e_{ij} = \mu \left(\frac{\partial u_i}{\partial x_j} + \frac{\partial u_j}{\partial x_i} - \frac{2}{3} \delta_{ij} \frac{\partial u_k}{\partial x_k} \right), \quad (3.14)$$

where μ is the fluid viscosity.

Equation 3.12 can be differentiated with respect to t , where the divergence of ?? is taken and subtracted, to give Lighthill's equation

$$\frac{\partial^2 \rho'}{\partial t^2} - c_0^2 \nabla^2 \rho' = \frac{\partial T_{ij}}{\partial x_i \partial x_j}, \quad (3.15)$$

where

$$T_{ij} = \rho u_i u_j + \delta_{ij} [(p - p_0) - c_0^2 (\rho - \rho_0)] - e_{ij}, \quad (3.16)$$

is the Lighthill's turbulence stress tensor. The flow variables have been decomposed such that

$$p = p_0 + p' \quad (3.17)$$

$$\rho = \rho_0 + \rho' \quad (3.18)$$

where the zero subscript denotes the the reference values of the properties at large distance from the turbulent flow, and the dash denotes the small perturbations.

Lighthill's equation 3.15 has the same form as the wave equation that governs the acoustic field produced by a quadrupole source in a non-moving medium, which means that there is an analogy between the flow induced den-

sity fluctuations and a distribution of quadrupoles in a non-moving medium. Lighthill's equation is a consequence of the laws of conservation of mass and momentum, thus it is in effect an exact equation, i.e. it is satisfied for all real flows. Thus the $\frac{\partial^2 T_{ij}}{\partial x_i \partial x_j}$ term accounts for all acoustic waves interacting with the flow, but it cannot be predicted without some knowledge of the sound field. Solving for T_{ij} is equivalent to solving the complete non-linear equations for the flow problem, which is difficult for most realistic problems. However, by making some assumptions about T_{ij} we can obtain a reasonably good estimate of the sound field.

For isothermal flows T_{ij} is approximately equal to $\rho u_i u_j$ inside the flow, and approximately equal to zero outside the flow. Assuming the density fluctuations within the flow are negligible, we can use the following approximation

$$T_{ij} \approx \rho_0 u_i u_j. \quad (3.19)$$

With knowledge of the turbulent flow we can treat the right hand side of the Lighthill equation as a known source term.

In the absence of any solid boundary the solution to Lighthill's equation 3.15 can be expressed in terms of a free space Green's function as

$$\rho'(\mathbf{x}, t) = \frac{1}{4\pi c_0^2} \int \frac{1}{R} \left[\frac{\partial^2}{\partial y_i \partial y_j} \frac{T_{ij}(\mathbf{y}, t - R/c_0)}{R} \right] d\mathbf{y}, \quad (3.20)$$

where the integration ranges over all y in the volume, T_{ij} is non-zero, and $R = |\mathbf{x} - \mathbf{y}|$ is the distance between source and observer. This can be related to the farfield pressure [22] using the farfield relationship $p' = c_0^2 \rho'$,

$$p'(\mathbf{x}, t) = \frac{1}{4\pi} \frac{x_i x_j}{x^3} \int \frac{1}{c_0^2} \frac{\partial^2 T_{ij}}{\partial t^2}(\mathbf{y}, t - R/c_0) d\mathbf{y}. \quad (3.21)$$

Importantly this formulation is in a fixed reference frame, and although convection due to the mean flow can easily be included, it is much more

difficult to include refraction effects. The formulation is also restricted to subsonic flows, as it does not account for shock generated noise.

3.3.2 Jet Scaling

The simplest and most practical deduction which can be made from the theory derived by Lighthill is the dependence of the sound field on the dimension D , and velocity U of the flow. Lighthill [23] said that frequencies of the sound field

$$f \propto \frac{U}{D} \quad (3.22)$$

and that the fluctuations in

$$\frac{\partial^2 T_{ij}}{\partial t^2} \propto \frac{U^2}{D^2} \rho_0 U^2. \quad (3.23)$$

Equation 3.21 can then be rewritten

$$p' \propto \frac{\rho_0}{c_0^2} U^4 \frac{D}{x} \quad (3.24)$$

thus the acoustics Intensity is proportional to

$$I(R) \propto \rho_0 U^8 c_0^{-5} \frac{D^2}{R^2}. \quad (3.25)$$

This is Lighthill's celebrated eighth power law, which has been well confirmed experimentally [24–26].

Lighthill [23] also went on to demonstrate that an additional convection term could be included to give the source strength a dependency on the polar angle θ , such that

$$I(R, \theta) \propto \rho_0 U^8 c_0^{-5} \frac{D^2}{R^2} (1 - M_c \cos \theta)^6, \quad (3.26)$$

where M_c is the mach number.

3.3.3 Lilley's Equation

Lighthill's theory of jet noise treats the sound sources as if they were moving through a stationary medium, and the directivity is accounted for by convection amplification. However, the motion of the mean flow in the immediate vicinity of the source should have a strong effect on the sound emission process, and that cannot be accounted for when using Lighthill's theory without adjusting the source term.

Lilley derived a third order wave equation in which all the 'propagation effects' occurring in a transversely sheared mean flow are accounted for in the wave operator part of the equation

Tester and Morfey [27] provide a modified version of Lilley's equation for a single-frequency Greens function in a axisymmetric parallel sheared flow

$$\bar{\rho}Q = \left((1/c^2) \frac{\overline{D^3}}{Dt^3} + \frac{\overline{D^2}}{Dt^2} \nabla^2 + (1/\bar{\rho}) \frac{d\bar{\rho}}{dr} \frac{\overline{D}}{Dt} \frac{\partial}{\partial r} + 2 \frac{dU}{dr} \frac{\partial^2}{\partial x \partial r} \right) G \quad (3.27)$$

where, Q is a complex source term and

$$\frac{\overline{D}}{Dt} = \frac{\partial}{\partial t} + U \frac{\partial}{\partial x}. \quad (3.28)$$

A number of solutions to the Lilley equation have been presented [28], however they are somewhat beyond the scope of this chapter. The Powles solution is used Chapter 6 for the purpose of validation of a ray method.

3.4 Semi-Empirical Jet Noise Models

Jet noise prediction methods as employed in industry still rely on measured data. Empirical methods based on databases [29] and semi-empirical methods [30–32] using simple jet scaling laws combined with data still provide the most fast and reliable jet noise prediction schemes used in industry.

Stone's [30] semi-empirical model of jet noise, is based on a combina-

tion of analytical models modified using experimental data. The model can predict the scaling of jet noise based on change of parameters such as velocity, nozzle diameter, and density. Lighthill's eight power law is used to determine the OASPL at ninety degrees. Corrections for the shear layer are incorporated into an empirical spectral directivity function. Stone provides the function tabulated in terms of jet Strouhal Number, usually defined

$$St = \frac{fD_j}{U}. \quad (3.29)$$

The function can be integrated over the spectrum at any angle, to give an OASPL for a static jet.

3.4.1 A Coaxial Jet Noise Model

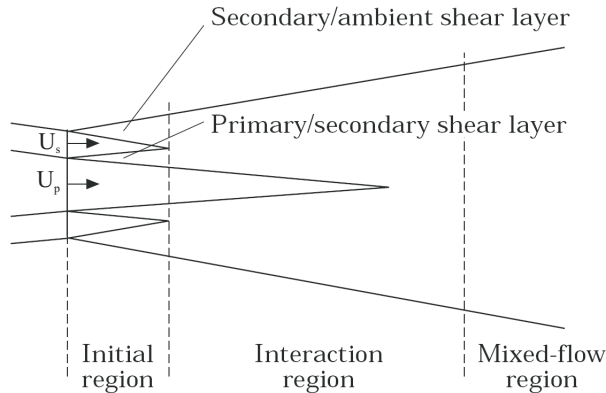


Figure 3.5 – Regions of a Coaxial Jet.

A coaxial jet, much like a single stream jet, generates noise due to mixing between the exhaust flows themselves and mixing of the exhaust flows with the atmosphere. First we consider the regions of a coaxial jet flow as described by Ko and Kwan [33] and then we show how the method of Fisher et al. [31] can be applied to predict the noise.

Figure 3.5 is a simple representation of the three different regions of a coaxial jet flow exhausted from a axisymmetric coplanar nozzle. In the

initial region close to the nozzle there is an mixing region that contains the potential cores of both the primary and secondary jets. Beyond the end of the potential core of the primary jet, in the mixed flow region, the the flow behaves as the flow of a fully mixed single stream jet. Between these two regions is a region of complex flow, known as the interaction region.

Firstly, considering the initial mixing region, we have two shear layers, primary and secondary. The primary shear layer is the region between the two potential cores. This region behaves as the initial part of single stream jet, with the sources strength a function of the relative jet velocity, i.e. $U_p - U_s$. This region is generally of little importance, relatively speaking, for two reasons. Firstly the velocity ratio of modern turbofans is often close to unity, thus noise levels are low relative to other jet sources. Secondly any source here is shielded by the secondary shear layer.

The secondary shear layer is created by the mixing of the secondary jet with ambient air. This effectively behaves like a single stream jet characterized by the secondary jet velocity. This secondary shear layer is of importance as it generates high frequency noise, which, due to its location on the outside of the jet, can propagate out of the jet without being attenuated.

In the far downstream mixed flow region of the jet, it will be the mixed flow jet velocity, temperature, and diameter that will characterize the noise. This region generates the principal source of low frequency of noise from a coaxial jet.

Between the initial and fully mixed regions lies the interaction region in which the primary and secondary shear layers merge. This important noise producing region, produces both high and low frequency noise. Characterizing the acoustic properties of this region based on jet parameters is difficult.

The four source model described by Fisher et al. [31, 32] identifies four equivalent jets in the three regions of the coaxial flow. These four sources

can be modeled as single stream jets, which can be combined to give a coaxial prediction. It is well known that the shear layer near the nozzle is the primary source of high frequency noise, and that further down stream the lower frequencies are the dominant sources. So in the model care is taken, as to only apply the part of the spectrum to each source which is relevant to the problem, this is accounted for by a filtering process.

In the initial region we have identified two acoustically equivalent jets, corresponding to the two shear layers. Generally only the secondary shear layer jet is included in the four source model, making it effectively a ‘three source model’, as at realistic jet operating conditions the contribution of the primary jet is negligible.

In the interaction region the flow is more complex, with the primary and secondary shear layers interacting and the primary core still present. This is the effective jet, the parameters are the same as the primary jet, however an analytical expression for a modified jet diameter is presented. Measurements show the turbulence in this region is lower than that of that of the effective jet defined, so a correction based on Lighthill’s stress tensor is also applied.

In the main jet region the equivalent jet parameters are based on the idea that the primary and secondary flow are fully mixed. The four source model provide analytic expressions for the mixed jet properties, based on the jet parameters.

Portions of the single stream jets representing the coaxial jet do not exist, i.e. upstream portion of fully mixed jet does not exist and downstream portion of secondary jet does not exist. To correct for this spectral filter functions are based on the a single stream jet source distribution are applied. The jet source distribution is considered in more detail in a subsequent section.

3.5 Jet Noise Spectra

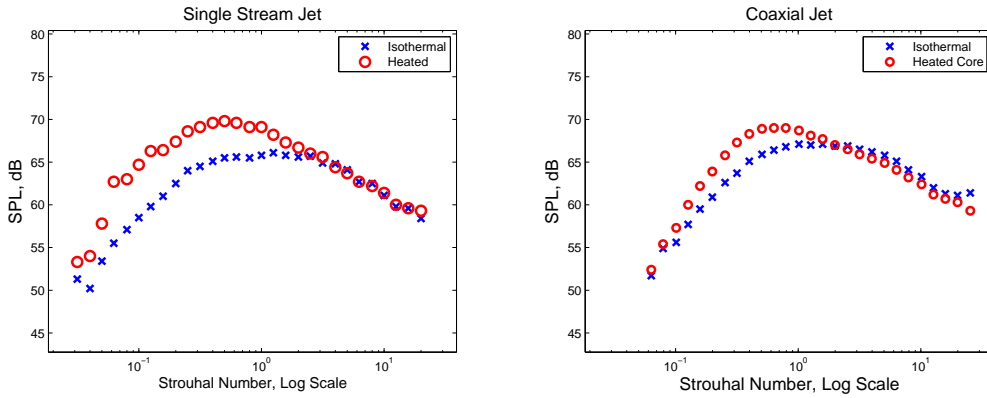


Figure 3.6 – Jet Noise Spectra - Single stream, Isothermal, $M = 0.5$. Single stream, Temperature ratio 2.5, $M = 0.5$. Coaxial Jet , Area ratio 4, Temperature ratio 1 (isothermal), Velocity ratio 0.79. Coaxial Jet, Area ratio 4, Temperature ratio 2.8, Velocity ratio 0.79

Jet noise prediction still relies heavily on empirical methods derived primarily from model-scale test data. Until recently the turbulence closure problem has meant that CFD methods could not yield the properties of the turbulent field in the sufficient detail required for noise calculation. Traditional Reynolds-Averaged Navier Stokes (RANS) based methods do not provide spectral or directivity information about the noise from the CFD [34, 35].

Recent advances in computational power have allowed Large Eddy Simulation (LES) [36] and Direct Numerical Simulation (DNS) methods [37] in which the aerodynamic field and the acoustic field are simultaneously calculated by solving the compressible unsteady Navier-Stokes equations, however calculations are painfully slow. The grid requirements of both are difficult to achieve, and their application is limited to some laboratory experiments with typical jet exit Reynolds numbers of about 10^5 , thus practical jet noise predictions are still semi-empirical.

Figure 3.6 shows typical jet noise spectra, for an single stream jet and a coaxial jet. The data is taken from CoJeN (European Sixth Framework

Project) model scale tests. The single stream jet had a Mach number of 0.5, with a temperature ratio of 2.5. The coaxial jet had a area ratio of 4, and velocity ratio of 0.79, with a temperature ratio of 2.8.

As can be seen from the figure the heating the jet, both single stream and coaxial, tends to increase the noise levels at lower frequencies, while decreasing the level at higher frequencies.

Increasing the temperature of a single stream jet can have variable effects on the noise levels, experiments have shown that at low jet velocities it tends to increase the noise level, while at high velocities it tends to decrease the noise level generated. Increasing the temperature introduces a new more efficient dipole source in the jet [38]. However increasing temperature of a jet means a decrease in density, and this has an effect on acoustic efficiency.

3.6 Jet Source Directivity

A jet source is highly directional, this is primarily due to the convective amplification, or Doppler amplification, of the sources by the flow, and also, to a lesser extent, due to acoustic mean flow interaction effects. Lighthill's Acoustic Analogy does not account for jet source directivity. When modeling jet noise using a Lighthill approach, we define an inherent directivity due to convective amplification, which is independent of the source as a function of angle and Mach number, such that

$$SPL_{jet}(\theta, M) = SPL(90, M) + D(\theta, M) \quad (3.30)$$

where D a directivity function, $SPL(90)$ is the sound pressure level at 90 degrees polar angle, M is the Mach number, and θ is the polar angle. Fowles Williams [22] defined the inherent directivity as

$$D(\theta, M_c) = 10 \log\left(\frac{1}{(1 - M_c \cos \theta)^5}\right) \quad (3.31)$$

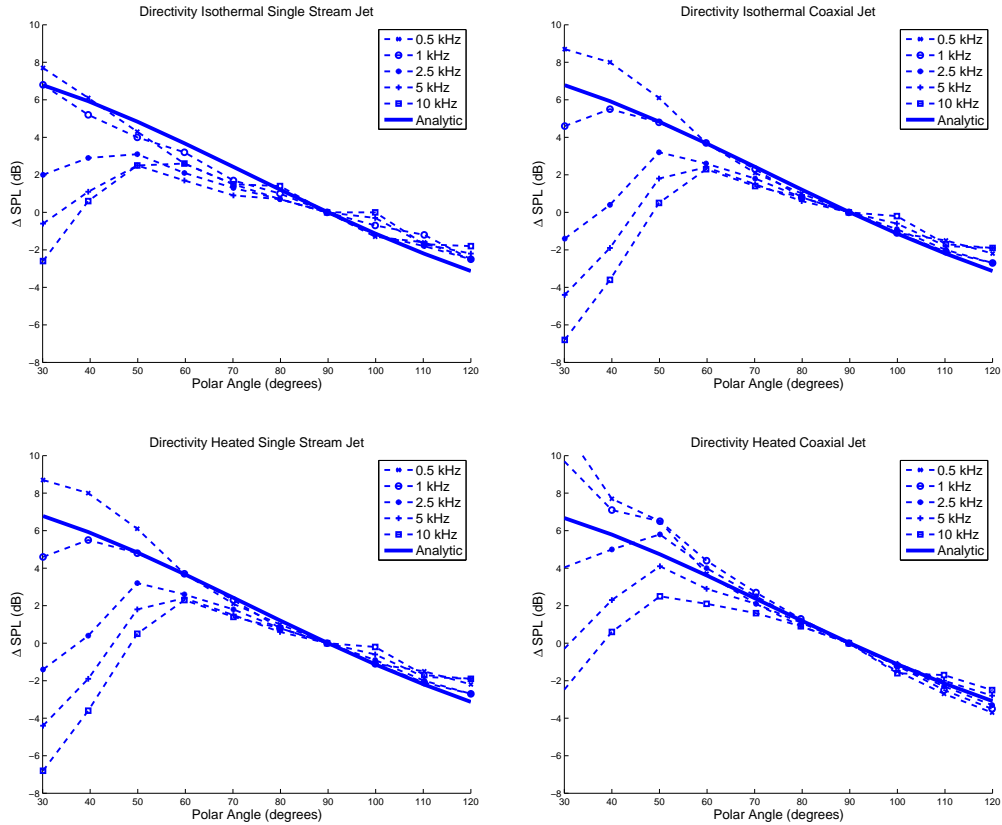


Figure 3.7 – Jet Source Directivities- - Single stream, Isothermal, $M = 0.5$. Single stream, Temperature ratio 2.5, $M = 0.5$. Coaxial Jet , Area ratio 4, Temperature ratio 1 (isothermal), Velocity ratio 0.79. Coaxial Jet, Area ratio 4, Temperature ratio 2.8, Velocity ratio 0.79

where M_c is the convective Mach number, i.e the mean flow velocity at the source position. For a single stream jet Lighthill [39] suggested, as most the sources are at the centre of the shear layer, that a good approximation was $M_c = 0.5U_j$, where U_j is the velocity at the at nozzle. Since then others [22] have shown using flow visualization techniques that $M_c = 0.62U_j$ is a better approximation for the velocity at the centre of shear layer.

Using CoJeN data for both isothermal and heated single stream and coaxial jets, Figure 3.7 shows four jet source directivity plots. Each plot contains a range of frequencies, a directivity ΔSPL , as defined in equation 3.30, is plotted against polar angle. Also included in the plot is an analytic

directivity calculated using equation 3.31. For the coaxial cases we assume that the dominant sources are in the secondary shear layer and use the secondary jet exit velocity to calculate the convective Mach number.

For all four jets the directivity is relatively independent of frequency over most polar angles. However at lower polar angles the curves drop away. This phenomenon is known as the ‘cone of silence’, caused by energy being reflected by the shear layer at low angles of incidence, i.e beyond a certain critical angle noise is reflected from the jet.

The analytic directivities fit the data well outside the cone of silence for both single stream and coaxial jets.

Changing the temperature of the jet changes the cone of silence angle, this can be observed for both the single stream and the coaxial jet. The source location also has an effect on this angle. Lower frequency sources are located further downstream, where the jet velocity is lower. As a result the cone of silence is at lower polar angles for lower frequency sources. The jet source distribution is considered in the following section.

3.7 Jet Source Distribution

When considering uninstalled jet noise the fact that the source is distributed becomes insignificant in the farfield. However, when predicting installed levels understanding the nature of the source distribution becomes very important, as the amount of the source which is reflected from the aircraft will be the most significant contribution to increased levels in the farfield.

Predicting the distribution of the jet noise source is a somewhat difficult task, simple semi-empirical models exist for isothermal single stream jets. A commonly used expression [31] to determine the shape of source distribution is

$$S(x) = x^{m-1} (m/x_c)^m e^{-mx/x_c}, \quad (3.32)$$

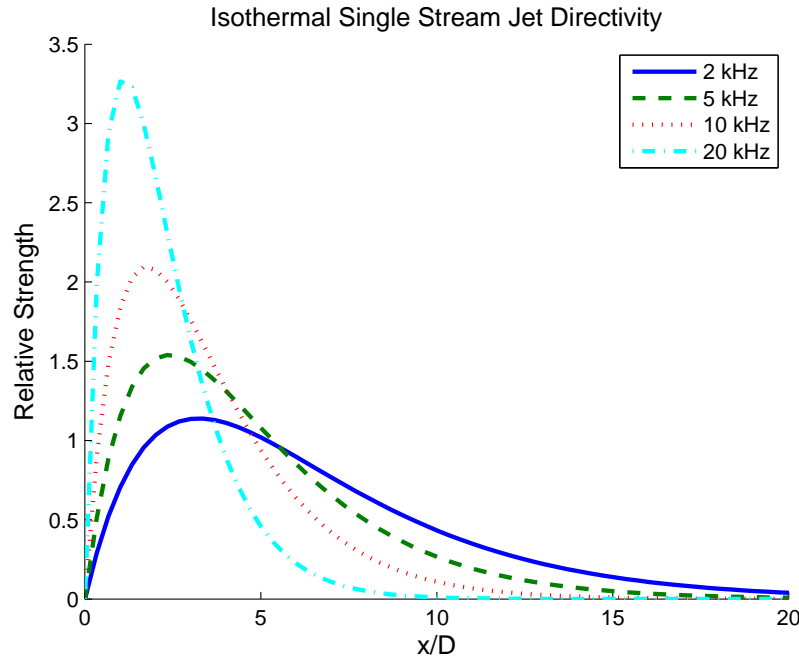


Figure 3.8 – Isothermal single stream jet source distribution for a range of frequencies/Strouhal numbers - 2 kHz / 1 St , 5 kHz / 3 St , 10 kHz / 6 St , 20 kHz / 12 St .

where S is relative strength per unit length, x_c is the centroid of the distribution, m is an adjustable shape factor in the range $m \leq 2$. This is a semi-empirical expression as it requires measurements to determine the centroid of the source distributions. Using a line of best fit to data Glegg [40] proposed this formula for determining the centroid

$$x_c/D_j = -1.8315 \log_e(St) + 6.7546. \quad (3.33)$$

Using this semi-empirical method figure 3.8 shows source distributions for an isothermal jet for a range of frequencies. As expected the higher frequencies are closer to the nozzle, while the lower frequencies are more distributed.

To determine the source distribution of an isothermal coaxial jet the expressions above can be combined with the well known four source model [31], to give a semi-empirical prediction for the source distribution.

However empirical methods are more accurate, particularly when considering more complex nozzle geometries. To date one of the most effective measurement methods for determining jet source distribution is the Polar Correlation technique (PCT), developed by Fisher et al. [41].

Figure 3.9 shows source distributions for a heated coaxial jet measured using the PCT, for a range of frequencies. The jet has velocity ratio 0.8 and temperature ratio 4. Like the single jet the coaxial source distributions are frequency dependent, with higher frequencies being closer to the jet nozzle. The lowest frequency distributions look much like that of a single stream jet, as most of the source is in fully mixed region. At medium to high frequencies the distributions appear to be composed of two distributed sources.

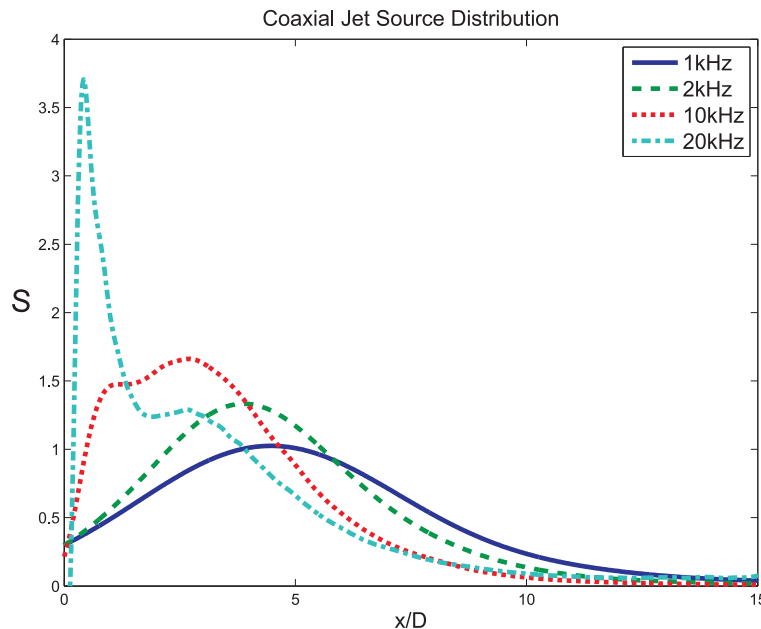


Figure 3.9 – Heated coaxial jet source distributions for frequencies/Strouhal number - 1kHz / 0.5St , 2kHz / 1St , 10kHz / 5St , 20kHz / 10St .

3.8 An Installations Jet Source Model

In this section we develop a jet source model which we can use to determine installation effects. The source model contains all the aspects of the source which are necessary to determine reflected levels.

A turbulent jet represents a broadband noise source distribution that is distributed over the volume of the jet. Matters can be simplified by assuming that the jet can be adequately approximated as a simple line source along the centre of the jet or as a line of ring sources.

A continuous line source distribution can be approximated by a number of discrete point sources, similarly a line of ring source can be approximated to a discrete number of point sources, see figure 3.10. Using the line source the energy concentrated at a point on the jet centerline can distributed about a ring of sources.

The Polar Correlation technique determines an equivalent line source strength to determine jet source distribution (results have been presented in the previous section). Similarly we assume that we can model the distributed jet source using a line source.

To determine a ΔSPL to the jet source, the overall source strength is unimportant, however the relative source distribution is important, i.e. all we need to know is what proportion of the source that is reflected from the wing to determine an installation delta SPL.

We also assume that the jet source can be represented by a distribution of monopoles. Given the random distribution and orientation of the jet source quadrupoles, this should accurately represent the energy distribution. Using a free field Greens function the total pressure field, at some point \mathbf{x} , due to distribution of the monopoles can be defined as

$$p' = \sum_{i=1}^n \frac{e^{ikR_i + \psi_i}}{4\pi R_i} A_i d_i, \quad \text{where } R_i = \mathbf{x}_i - \mathbf{x}, \quad (3.34)$$

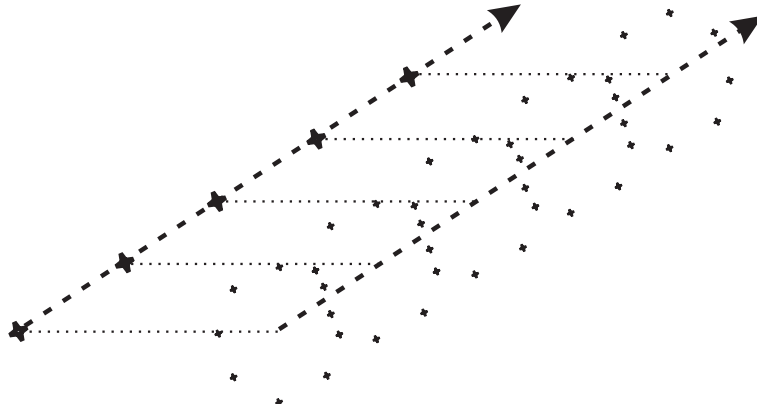


Figure 3.10 – A discretised line source distribution, and an equivalent discretised ring source distribution.

\mathbf{x}_i is the source position, n denotes the number of monopoles, A_i is the relative pressure amplitude factor, $d_i(\theta_i)$ is a pressure directivity function, and ψ_i is randomly varying phase function. The mean squared pressure is given by

$$\overline{p^2} = \frac{1}{2}pp^* = \frac{1}{2} \left(\sum_{i=1}^n \frac{e^{ikR_i + \psi_i}}{4\pi R_i} A_i d_i \right) \left(\sum_{j=1}^n \frac{e^{-ikR_j - \psi_j}}{4\pi R_j} A_j^* d_j^* \right), \quad (3.35)$$

assuming that the sources are totally incoherent we can write

$$\frac{1}{2}pp^* = \frac{1}{2} \sum_{i=1}^n \frac{|A_i|^2 d_i^2}{(4\pi)^2 R_i^2}. \quad (3.36)$$

Thus the sound pressure level is defined as

$$SPL_{jet} = 10 \log_{10} \left(\frac{1}{2} \frac{\sum_{i=1}^n \left| \frac{A_i d_i}{4\pi R_i} \right|^2}{p_{ref}^2} \right). \quad (3.37)$$

In performing such a discretization it is essential that a sufficient number of discrete sources is taken to ensure convergence, equally, speed of computation dictates that the minimum number required is chosen.

To determine the number of discrete sources required for the jet model

source distribution, sensitivity studies using this source model, in conjunction with the installations model developed in chapter 4, were conducted and published [42]. The results of this have been outlined in appendix A.3. The jet source is distributed over ten secondary nozzle diameters, as this adequately captures the distributed source down to lowest frequencies required. It was found that using 100 ring sources, each ring comprising of 50 monopole sources, give convergence of the solution to less than 0.01 dB. It was also found that giving the ring sources a radius equivalent to that of the primary nozzle gave the most accurate results, when using in combination with a jet installation effects prediction method.

The basic jet source model for installation effects has been outlined. In the following Chapter installations effects experimental data is reviewed. In Chapter 4 the jet source model is used as part of an installation effects prediction scheme, in this chapter we outline how we define the various functions describing the jet source.

Chapter 4

Experimental Programme and Results

In this chapter previous experimental work quantifying jet noise installation effects is reviewed and discussed critically. The review will highlight a number of shortcomings of the previous work, such as an insufficient number of microphones and the inability to distinguish between reflection and refraction effects. In addition a new set of model scale jet noise installation effects experiments designed to overcome the shortcoming of the previous work are described.

The layout of the chapter is as follows. Previous experimental work is critically reviewed. A new programme of installation experiments are outlined, the research was carried out under the UK Technology Strategy Board (TSB) project ANDANTE - Aircraft Noise Disturbance Alleviation by Novel TEchnology. The results of the experiment are analyzed and provide the reader with a greater depth of understanding of the installations problem.

4.1 Literature Review

As mentioned in the Introduction of the thesis, there have been a number of model scale tests to date quantifying installed jet noise levels.

The first comprehensive set of jet noise installation effects measurements published are those of Way and Turner [8]. These model scale tests quantified the effects of installing a jet underneath a wing. Way and Turner measured the change in SPL due to the installation of a realistic wing above a coaxial jet using microphones positioned at different polar angles to the jet. It was noted that the measured levels of reflected jet noise were notably less than the expected 3dB, which would represent a doubling of the pressure that one would expect if the total source is reflected from the wing. This was likely to be due to the attenuation of the reflected signals propagating through the jet exhaust. Taking data from a single polar array below the jet allowed the authors to draw this important conclusion. However it also highlights the shortcomings of the experiment. The problem being that the noise measured on a microphone directly beneath the wing and the jet has been both reflected by the wing and refracted by the jet, making it difficult to distinguish between the two effects.

Another early paper quantifying installed levels is that of Wang [9]. In this paper an idealised flat plate wing is placed above a single stream jet, and measurements were made on both a polar array directly below the jet, in the flyover plane, and an azimuthal array downstream of the jet, to take sideline readings. The results published generally agree with those of Way and Turner, which indicates that the flat plate wing is a good approximation to a real wing. Importantly he also noted that installation effects can increase the sideline levels. This could suggest the possibility that the reflected noise from the wing was being refracted to the sideline, creating a blockage region beneath the jet, however this is not a conclusion that has been drawn in this paper. The limited number of microphones used in the test makes

it difficult to separate the effects of refraction and reflection and to draw reliable conclusions.

It was not until the late 1990s that further jet noise installation effects measurements were published. A series of model scale tests to measure installed jet noise were published by Shivashankara and Blackner [10] in 1997. These tests involved a 1/20th scale model aircraft in a flight stream above a heated coaxial jet. Installed jet noise levels were measured on an traversing azimuthal array, and an acoustic mirror was used to determine source location on the geometry. The authors noted that the presence of the model aircraft increased the levels in jet noise, more so for the inboard engine, than the outboard engine. Using data taken from the acoustic mirror they suggested the presence of the wing and pylon supporting the wing changed the shape of the jet so that it was no longer axi-symmetric. The wing is thought to particularly effect the shape of the secondary shear layer, which generates much of the noise which is reflected from the wing. Unfortunately, although data was taken on the azimuthal array at a range of polar and azimuthal angles, only results from the flyover plane were published.

An extensive published programme of model scale experiments measuring installation effects on jet noise is that of Mead and Strange [11]. The aim of the test was to quantify installation effects at sideline. They measured the change in sound levels of a model engine exhaust, due to the placing a number of different wing geometries above it, using a azimuthal microphone array. They noted a 2dB increase at most high frequency jet noise levels and an increase of up to 9 dB at the lowest frequencies. Again the limited number of microphones restricts the conclusions one can draw and distinguishing between reflection and refraction effects is difficult, however there is clearly an azimuthal variation in the levels due to the refraction by the jet, i.e. there is a distinct reduction in reflected levels directly below the jet in the blockage region.

All the experimental work to date can only give us a limited understanding of the physics of the problem. There are two major reasons for this. Firstly because of the limitations due to the number of microphones, this has meant that we can only ‘see’ or measure at a limited sector of the farfield at anytime. Using a single polar array is fine for measuring an axisymmetric jet source, however once an irregularly shaped wing is placed above the jet the source is no longer symmetric. The installation effects are very much a three dimensional problem, i.e. the problem cannot accurately be reduced to simpler 2-D problem. The other major issue with existing experiments is the difficulty of distinguishing between reflection and refraction effects. For these reasons a new set of experiments has been designed and carried out under the UK Technology Strategy Board (TSB) project ANDANTE (Aircraft Noise Disturbance Alleviation by Novel TEchnology).

4.2 Summary of Andante tests

The aim of the new set of jet noise installation experiments was to gain a fuller understanding of the three dimensional nature of the problem. The tests involved the installation of hardware around a nozzle assembly, to represent the installation effects with various levels of complexity. The extensive programme included a range of hardware builds, progressing from simplistic fundamental configurations to more realistic fully 3D geometries with flight simulation flow. A report on the full set of tests has been published [43]. The focus of this thesis is on the more fundamental configurations to gain an insight to the underlying physics of the problem.

In order to gain an understanding of the distinction between the reflection and refraction effects it was decided to undertake two separate installation tests. The first experiment is a configuration studying propagation of known sources through the jet, to quantify refraction effects. The second is a configuration quantifying the effects of installing a scale plan-form 2D

‘flat plate’ wing geometry on the model scale jet.

Improvements in computing power and acoustic acquisition equipment allows the use of many more microphones than used in previous studies, giving a much greater resolution of sound pressure levels in the farfield. During both experiments farfield acoustic analysis of the jet noise was performed using two arrays of microphones: a large 47 microphone azimuthal array capable of traversing along the jet axis from 2m upstream of the jet exit to around 7m downstream, and a 17 microphone polar array at a nominal radius of 12m. The azimuthal array was used to make measurements at eight positions along the jet axis, corresponding to eight polar angles between 40° and 110° measured to the downstream jet axis.

4.3 QinetiQ Noise Test Facility

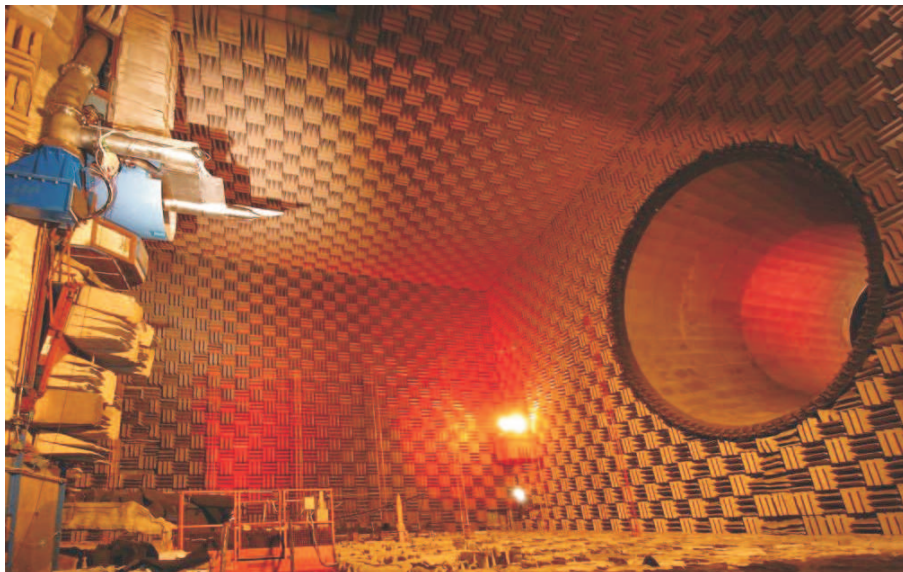


Figure 4.1 – QinetiQ’s Noise Test Facility.

QinetiQ’s Noise Test Facility (NTF), situated at Pyestock Hampshire, is a large high-quality anechoic chamber specifically designed for model-scale exhaust noise research. The facility has internal dimensions of 27m long by

26m wide by 17m high, making it suitable for far-field noise measurements. Twenty two thousand non-reflective wedges line the chamber, rendering it anechoic down to frequencies of 90Hz, and positive ventilation prevents hot-gas recirculation, providing a stable environment for acoustic experiments. A photograph of the chamber can be seen in figure 4.1.

The chamber can facilitate up to 1/10th-scale nozzle testing. The jet exhaust rig protrudes into the chamber at a height of 8.73m. Core and bypass air flows are supplied by a centrifugal compressor, to a maximum combined mass flow of 15kg/s at 3 bars. Core air is then heated to jet exhaust temperatures using an Avon combustion can, specially modified to burn LPG. Bypass temperatures are controlled by mixing in cooler air from a heat exchanger system. Test models are mounted onto a sting assembly which is cantilevered into the centre of the 1.8m diameter open jet used for flight simulation up to Mach 0.33. The air flow for this is supplied by a very large blower (350kg/s) through an extensive silencing arrangement such that the noise produced by the flight stream is effectively only due to that of the fundamental jet mixing. The test model protrudes from the flight-simulation duct by about one duct diameter, it can be seen protruding in the top right of figure 4.1, thereby enabling measurements to be made in the forward arc of the jet.

The target test conditions are corrected for day conditions, such that the acoustic Mach number remains constant. Aerodynamic data, in the form of multiple total pressure and temperature measurements, was acquired in real-time from rakes spanning the flows upstream of the nozzle assembly. The data was used to continually calculate and display the jet conditions, which were adjusted to match the corrected target conditions, in order to obtain a test point. Accurate pressure measurements are ensured by weekly calibration. Jet conditions were matched to tolerances of $\pm 3\text{m/s}$ on computed velocity and $\pm 5\text{K}$ on total temperature.

4.4 Details of Experimental Hardware

A number of new pieces of hardware were designed and manufactured by QinetiQ for the ANDANTE tests, including a model-scale exhaust nozzle, a plan-form model-scale wing, and a large-scale traversing azimuthal array.

4.4.1 Jet Nozzle

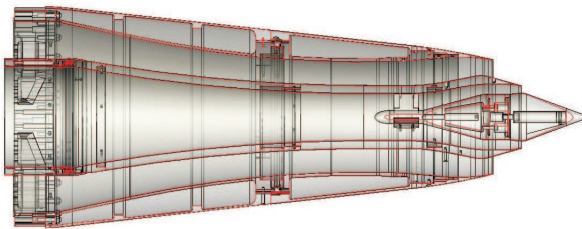


Figure 4.2 – Diagram of a 1/16th model scale idealized jet engine nozzle.

A 1/16th scale nozzle assembly was designed and manufactured for both sets of experiments. The nozzle is similar to that of a typical large four engined transatlantic airliner. A schematic of the axi-symmetric 3/4 cowell nozzle can be seen in figure 4.2. A table outlining aerodynamic nozzle parameters is given Table 4.1.

4.4.2 Microphone Arrays

Acoustic data from two arrays of microphones was acquired during the both experiments.

| Axisymmetric Nozzle Parameters | |
|--|----------|
| Core nozzle exit internal diameter (m) | 0.10173 |
| Core nozzle exit area (m^2) | 0.003158 |
| Core nozzle protrusion (from bypass) (m) | 0.0475 |
| Bypass nozzle exit internal diameter (m) | 0.18573 |
| Bypass nozzle exit area (m^2) | 0.013728 |

Table 4.1 – ANDANTE Jet Nozzle dimensions.

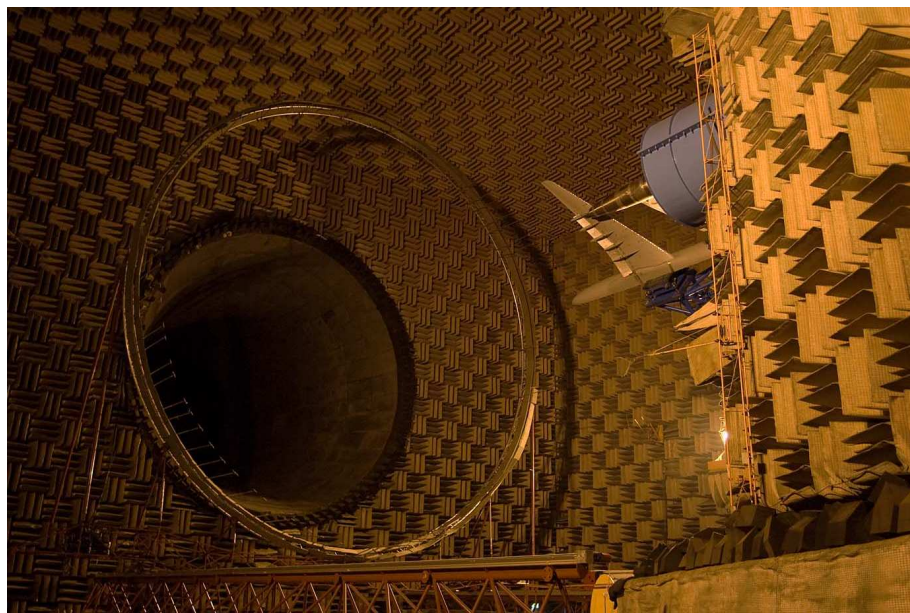


Figure 4.3 – Traversing microphone array at QinetiQ’s Noise Test Facility.

A conventional polar array was used to make measurements of the acoustic farfield. It centred on the bypass exit plane of the nozzle assembly. The masts supporting this array are a fixed feature of the NTF, and as such cannot be adjusted to give a constant polar distance to the nozzle exit, hence a variation in range is expected from the nominal 12m.

A traversing circular array shown in figure 4.3 was also used to acquire data. The array could traverse along two rails, parallel to the jet axis and extending the full length of the chamber. The microphones were supported on a 12m diameter open-lattice structure aluminum ring, centred on the jet axis. Independent motor drives on each of the rails were used to traverse the circular array along the jet axis, whilst bespoke software and an independent encoder system verified the accuracy of the drive system (better than $\pm 1\text{mm}$). During the test program, acoustic measurements were made at eight traverse positions, corresponding to polar angles 40° - 110° to the jet axis, in eight 10° steps.

Deflection of the ring from the vertical due to the entrained airflow

through the chamber was considered in the design, and estimated to be less than 5mm. Movements of the traverse during the testing were set to follow a profile of gentle acceleration and deceleration of 10mm/s^2 to minimize ring and microphone movement when measurements were being made. 47 free-field 1/4" microphones were positioned around the ring circumference, at a range of azimuthal angles.

4.4.3 Loudspeakers

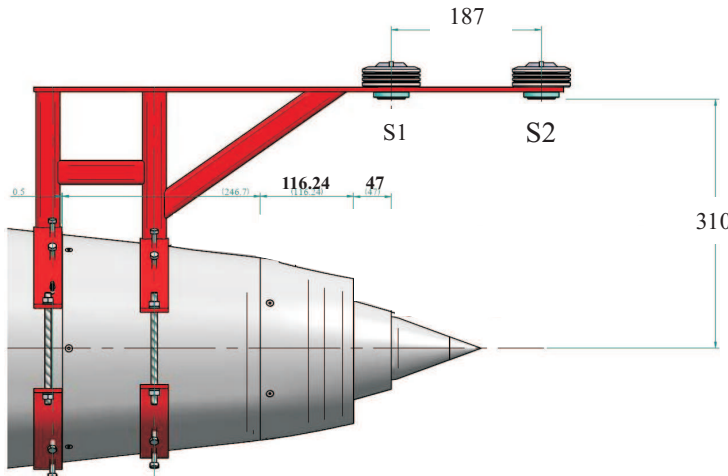


Figure 4.4 – Diagram of external source positions.

The first experiment (Experiment 1) designed to quantify the refractions effects due to the jet on a known source. It consisted of an external loudspeaker mounted above the jet, see figure 4.4. As can be seen from the diagram there are two external loudspeaker source positions, each of which was driven separately, so that blockage data could be taken from the two different source positions. However in this thesis we shall only consider data measured when the source at position S2 was being driven. This position was favored because of concerns that reflections from the nozzle, at position S1, would corrupt the data.

The speaker was then driven at a range of frequencies and measurements were taken at a full range of microphone positions using the traversing array, for a range of jet operating conditions. The source was driven at 1.25kHz, 2.5kHz, 5kHz, 10kHz, 15kHz and 20kHz, which at full scale is equivalent to 78Hz, 156Hz, 312Hz, 937Hz, and 1.25kHz respectively.

A change in sound pressure level, or blockage, due to the presence of the jet was measured according to,

$$B = \Delta \text{SPL} = \text{SPL}_{jet} - \text{SPL}_{ff}, \quad (4.1)$$

where SPL_{jet} is the sound pressure level due to the source propagating through the jet, and SPL_{ff} is the sound pressure level due to the source in the free field, i.e. in the chamber with jet switched off.

4.4.4 Flat Plate Wing



Figure 4.5 – Diagram of profile of the flat plate wing versus a realistic wing.

The second experiment (Experiment 2), was designed to measure the change in noise level due to the presence of the wing above the jet. Again the change in sound pressure level was measured at a full range of microphone positions using the traversing array. Which is defined as

$$\Delta \text{SPL} = \text{SPL}_{wing} - \text{SPL}_{iso}, \quad (4.2)$$

where SPL_{wing} is the sound pressure level due to the jet with the wing mounted above it, and SPL_{iso} is the sound pressure level due to the isolated

jet.

The wing used in experiment 2 was a plan-form wing typical of a 1/16th scale long range 4 engined jet airliner. Dimensions of the wing can be seen in figure A.1 in Appendix A. In figure 4.5 is a profile of the flat plate wing compared against a realistic wing profile which shows that flat plate wing is a reasonable approximation to realistic wing. Results from this experiment are used to validate the prediction methods developed in later Chapters. The wing was mounted so that the nozzle was at the inboard engine position.

4.5 Data Processing

Atmospheric attenuation has been accounted for during the post-processing of the polar and azimuthal array data using the Bazley model [44]. A level correction to 1m polar distance from the datum bypass nozzle exit, using the measured distance to each microphone, has been applied. Each test point has been corrected for the chamber background noise using data measured on the day of testing.

4.6 Results

In this section results from each experiment are presented. Each set of figures is followed by a discussion. The results are presented for a range of jet condition which are highlighted in Table 4.2.

| Name | U_p - m/s | T_p - K | U_s - m/s | T_s - K | U_s/U_p | T_s/T_p |
|--------------|-------------|-----------|-------------|-----------|-----------|-----------|
| Isothermal | 142 | 313 | 159 | 313 | 1.12 | 1.0 |
| Heated Core | 142 | 500 | 159 | 313 | 1.12 | 0.63 |
| Approach | 142 | 703 | 159 | 313 | 1.12 | 0.42 |
| Intermediate | 216 | 770 | 216 | 331 | 1.0 | 0.43 |
| Cutback | 275 | 770 | 254 | 331 | 0.92 | 0.43 |
| Sideline | 363 | 836 | 303 | 346 | 0.83 | 0.41 |

Table 4.2 – Jet Conditions used in model scale ANDANTE experiments.

4.6.1 Experiment 1 - Results

We now present the results from experiment 1, the experiment using a loud speaker above the jet, designed to quantify refraction effects in the jet.

Figure 4.6 contains blockage data taken using the traversing azimuthal array, for Sideline jet condition (jet conditions are outlined in table 4.2).

The figure contains six sub-plots, one for each different frequency at which the external source was driven, i.e. 1.25kHz, 2.5kHz, 5kHz, 10kHz, 15kHz, 20kHz. The change in SPL is shown by the contour lines, with the decibel color bar scale to the right of each figure. The figures show the change in SPL for a range of angles, with azimuthal angle on the horizontal axis and polar angle on the vertical. These type of contour plots have been used as they give a good overall view of the blockage region, allowing the reader to see the redistribution of the noise by the jet, however this makes reading absolute levels more difficult, thus more lines plot follow.

Figure 4.7 compares line plots of Δ SPL against azimuthal angle for two jet conditions, Isothermal and Approach. The only change between these two jet conditions is the temperature of the core. Results are plotted in six sub-plots, for three different frequencies, each for two separate polar angles, where each polar angle represents a single traverse position of the azimuthal array.

In the following figure 4.8, we compare blockage levels for the realistic jet operating conditions, Approach, Cutback and Sideline. Between these conditions both core and bypass, velocities and temperatures increase. Again results are plotted in six sub-plots, for three different frequencies, each for two separate polar angles, where each polar angle represents a single traverse position of the azimuthal array.

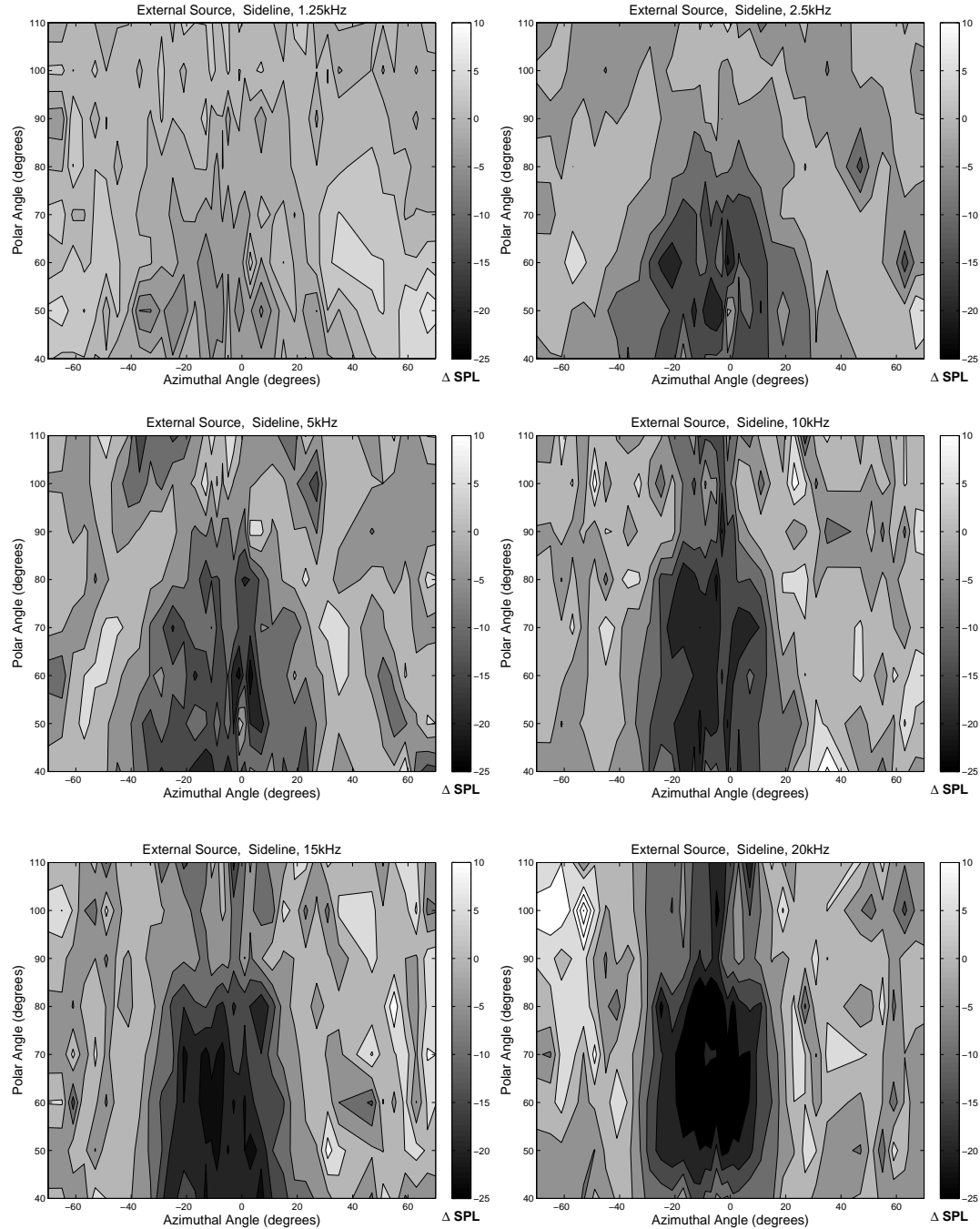


Figure 4.6 – Jet Blockage Δ SPL contour maps for Sideline Powered Jet. Each sub-plot represents the source being driven at a different frequency.

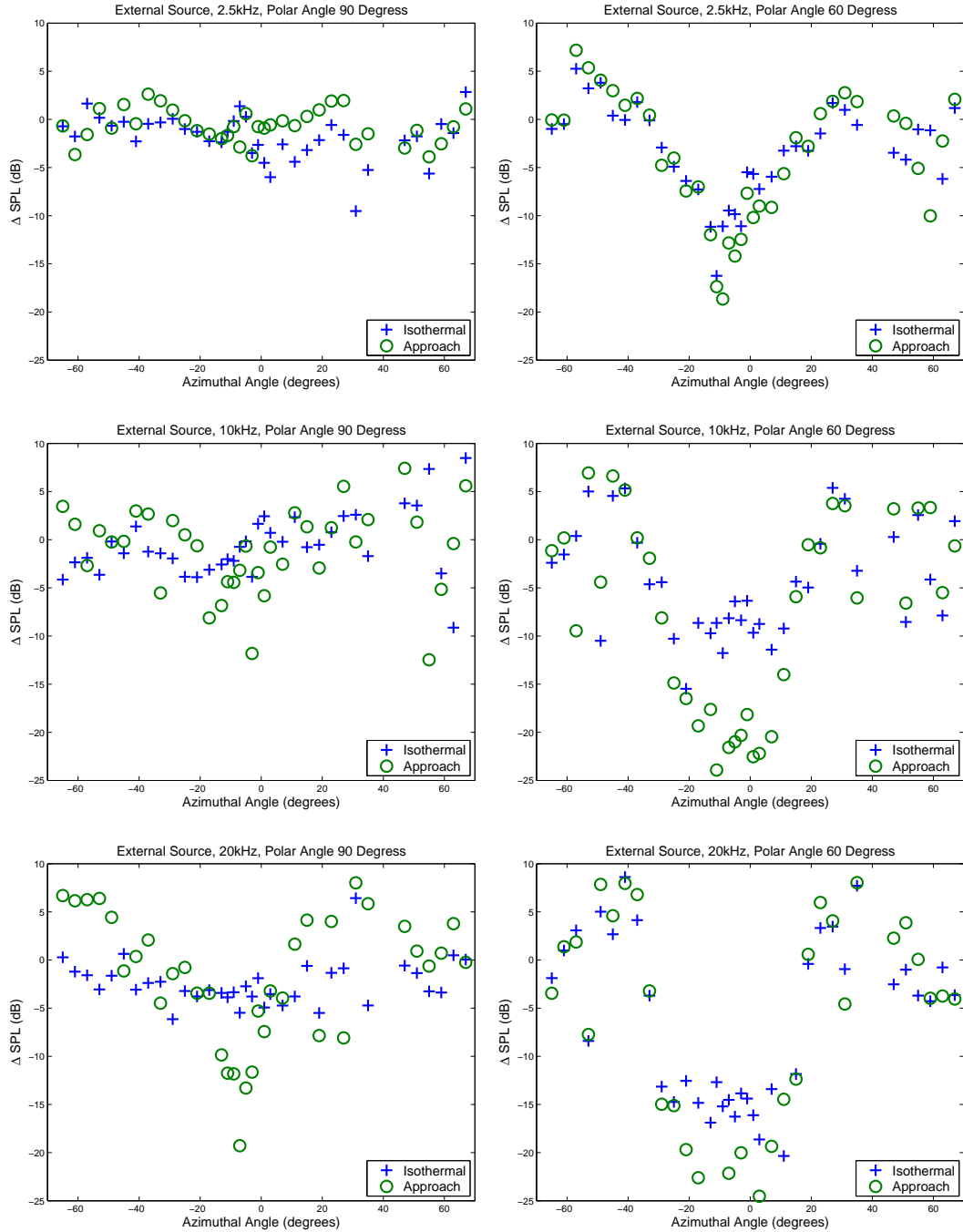


Figure 4.7 – Jet Blockage ΔSPL plotted against azimuthal angle, keeping all jet parameters constant while varying Core Temperature. Sub-plots represent polar angles of 90 and 60 degrees, for three separate frequencies.

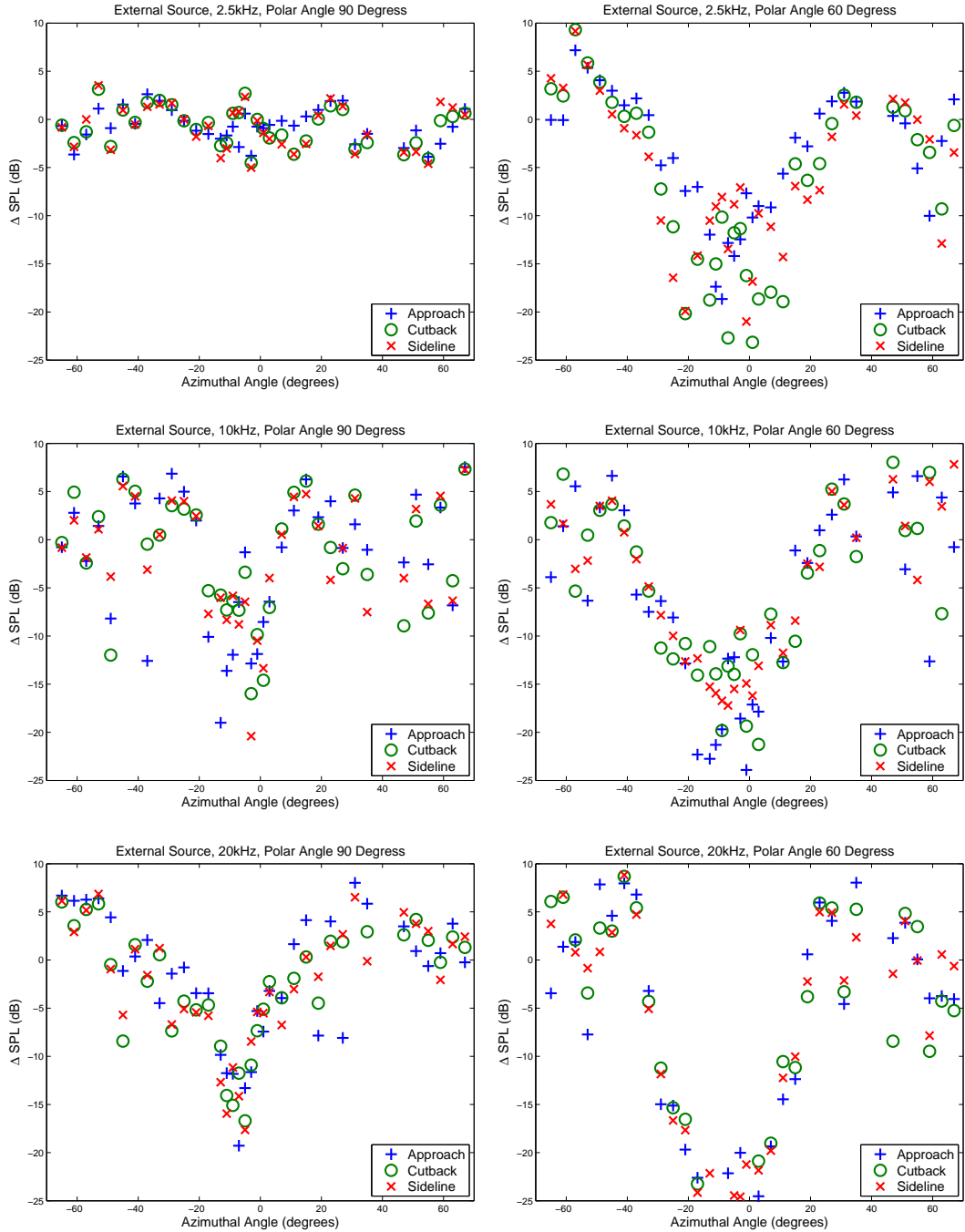


Figure 4.8 – Jet Blockage ΔSPL plotted against azimuthal angle, ranging through realistic jet conditions. Sub-plots represent polar angles of 90 and 60 degrees, for three separate frequencies.

4.6.2 Experiment 1 - Discussion

Simply looking at the highest powered jet condition, Sideline, in figure 4.6 using these plots demonstrates that the blockage region changes significantly with frequency. At low frequencies the blockage region is much further down stream, and much wider, consequently the blockage levels are shallow(down to -12dB) at low frequencies. This is a result of the lower frequencies diffracting around the jet, smearing the shadow region.

At higher frequencies, the blockage region is much more defined, blockage levels are deeper (down to -24dB) in the blockage regions, but there is also a clear redistribution of this energy. Along with the decrease in noise levels in the blockage region, we also have rises in noise levels outside the blockage region(up to +12dB), due to the redistribution of energy from the blockage region. This is caused by refraction of the acoustic rays which are trying to pass through the jet.

The loud speaker did not behave like a perfect monopole(having viewed the directivity it was considered reasonable) and the jet was not perfectly axisymmetric, thus accounting for the fact that the results are not perfectly axisymmetric.

By comparing jet conditions Isothermal and Approach, the effects of varying the core temperature of the jet can be observed, as this was the only parameter which changed between these two conditions. Figure 4.7 compares line plots of Δ SPL against azimuthal angle for each of the two jet conditions. Results are plotted in six sub-plots, for three different frequencies, each for two separate polar angles, where each polar angle represents a single traverse position of the azimuthal array. There is a certain amount of scatter on the data due to the turbulent fluctuations of the jet flow. However, we can note some distinct effects of changing the core temperature. At 90 degrees polar angle, the isothermal jet has almost no effect at any frequency, as expected Snells law tells us that rays should straight pass

through. Increasing the temperature causes levels in the blockage region to decrease, which in turn causes levels outside the blockage region to increase. These effects become more distinct with increasing frequency.

In the following figure 4.8, we compare blockage levels for the realistic jet operating conditions, Approach, Cutback and Sideline. Between these conditions both core and bypass, velocities and temperatures increase. Again results are plotted in six sub-plots, for three different frequencies, each for two separate polar angles, where each polar angle represents a single traverse position of the azimuthal array. There is a certain amount of scatter on the data, and no clearly distinct patterns relating to change in jet condition, at these realistic jet operating conditions. The shape of the blockage plots are consistent for the range of realistic jet condition shown in figure 4.8, and levels vary between conditions on average around 3dB.

This is likely to be a result of the fact that for all these jet conditions almost no sound passes through the core of the jet, and the blockage levels are a result of refraction by the shear layer. The shear layer is related to velocity and temperature ratio of the jet. As can be seen from table 4.2, there is almost no variation in the temperature ratio between jet conditions Approach and Sideline. There is a small variation in the velocity ratio. Comparing these results with figure 4.7, were the velocity ratio is constant but the temperature ratio is varied, we can certainly say that variations in the temperature ratio tend to be the more dominant effect.

4.6.3 Experiment 2 - Results

We now present the results from experiment 2, the experiment using a flat plate wing above the jet, designed to quantify jet noise reflection from a wing.

Figure 4.9 contains contour maps of Δ SPLs caused by placing the plan-form wing above the jet, for a jet Sideline condition, with data taken using the traversing azimuthal array. Each figure contains six sub-plots for a range of 1/3 octave band model scale frequencies, 1.25kHz, 2.5kHz, 5kHz, 10kHz, 15kHz, and 20kHz, respectively.

Figures 4.10 and 4.11 compare single polar angles from the Δ SPL contour maps, for all four realistic jet conditions, outlined in table 4.2.

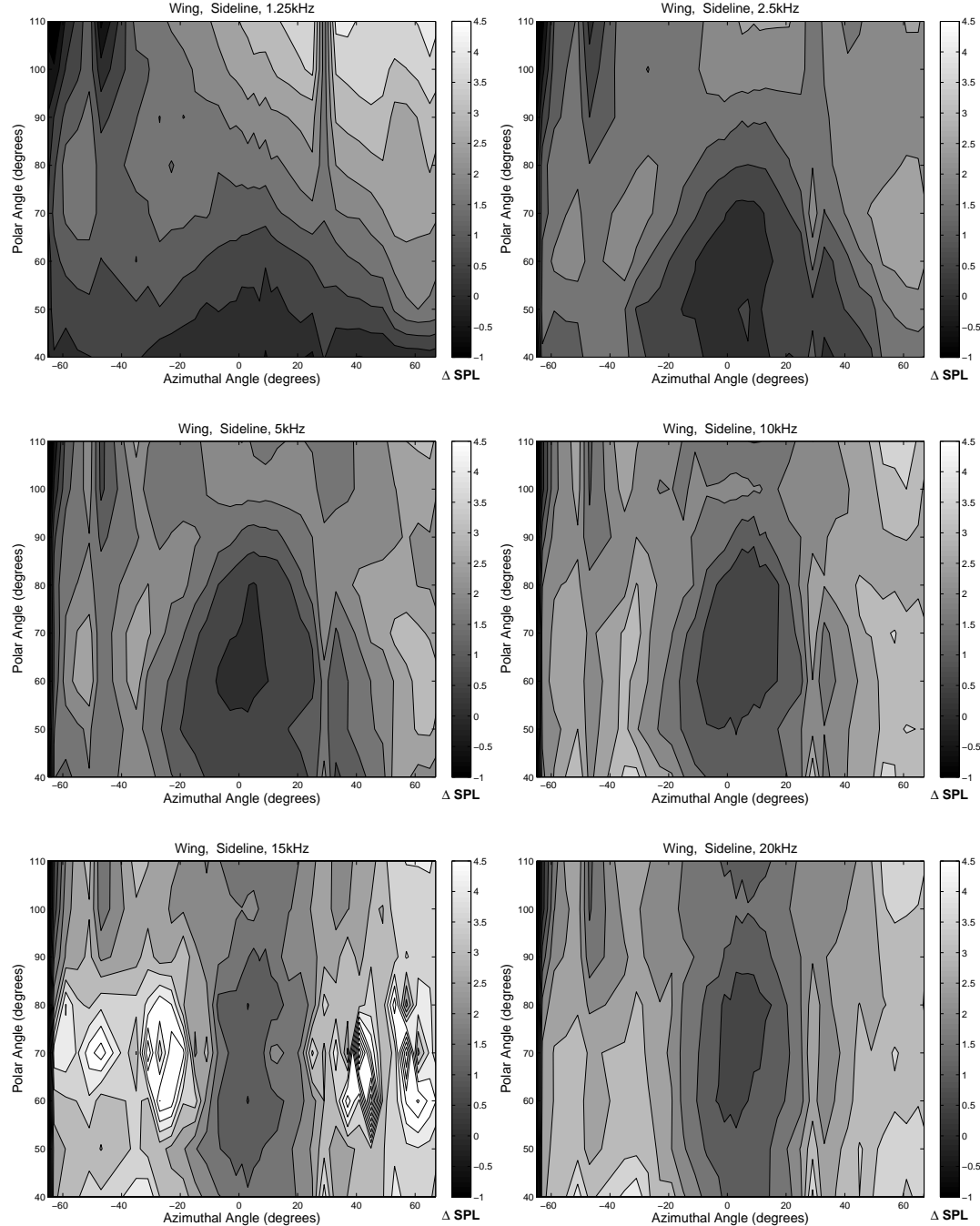


Figure 4.9 – Wing Δ SPL contour maps at Sideline Jet Condition. Each sub-plot represents different 1/3 octave band jet source frequencies.

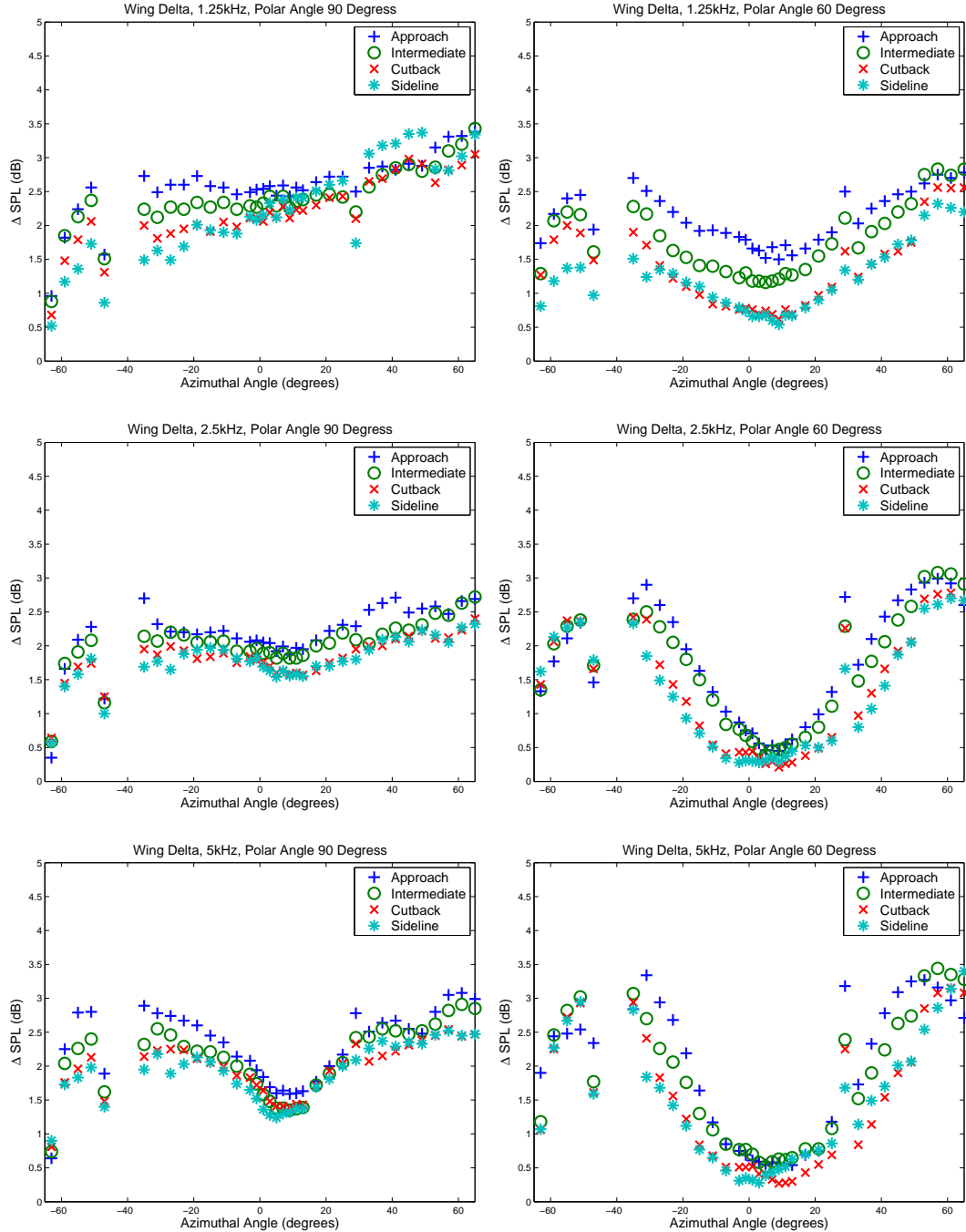


Figure 4.10 – Wing Δ SPL plotted against azimuthal angle, comparing levels at different jet condition, for three low frequencies, at polar angles of 90 and 60 degrees.

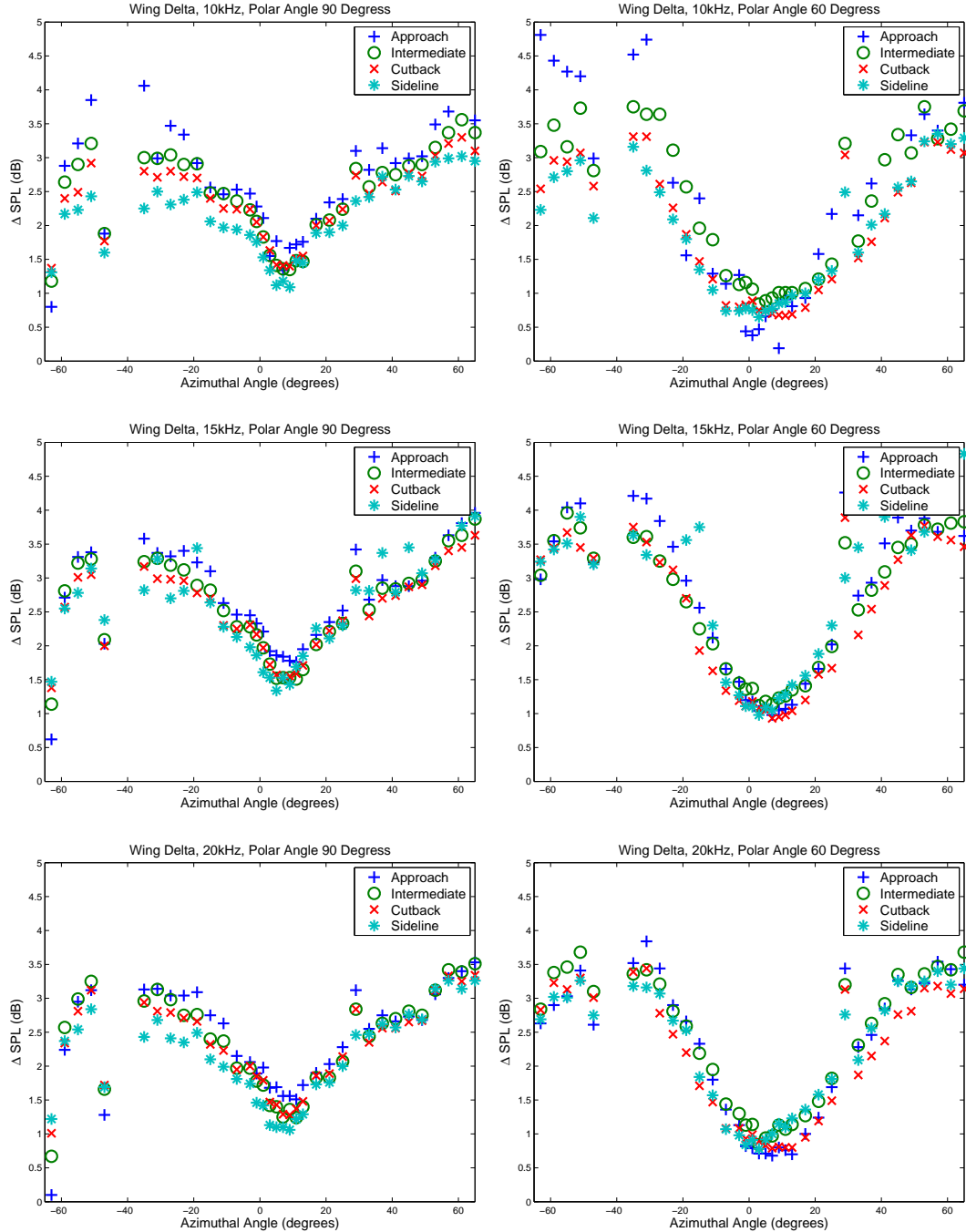


Figure 4.11 – Wing Δ SPL plotted against azimuthal angle, comparing levels at different jet condition, for three high frequencies, at polar angles of 90 and 60 degrees.

4.6.4 Experiment 2 - Discussion

Figure 4.9 demonstrates the effects of jet noise reflecting from the wing. It shows an increase in installation levels at all frequencies, with higher reflected levels at higher frequencies. This is expected as at high frequencies the jet source distribution is more compact, thus more of the source is underneath the wing. One can also clearly see the jet blockage effects, with the lowest Δ SPL levels being just off centre, of zero azimuthal degrees. This is due to the 6 degree dihedral angle of the wing. The redistribution of energy by the jet is also noted, with Δ SPLs of up to 3.5dB at low polar angles outside of the blockage region, particularly at higher frequencies.

Figures 4.10 and 4.11 compare single polar angles from the Δ SPL contour maps, for all four realistic jet conditions. In the first figure 4.10 the lower frequency Δ SPLs are plotted against azimuthal angle, with the traversing array at 90 degrees and 60 degrees polar angle. As can be seen from the plot there is distinct increase in level between jet conditions Approach and Cutback, consistently around 0.5dB at 90 degrees. At 60 degrees the difference is over 1.5dB at the lowest frequency, and just over 0.5dB at 5kHz.

In the following figure 4.11 the higher frequency Δ SPLs are plotted against azimuthal angle, with the traversing array at 90 degrees and 60 degrees polar angle. Again at 90 degrees there is an increase in level between jet conditions Approach and Cutback, consistently around 0.5dB. At 60 degrees the first frequency, 10kHz, has a difference of around 0.5dB between jet conditions, but we can see the difference diminishes as frequency increases.

4.7 Conclusions

In this chapter we have outlined a novel set of static rig model scale jet noise Installation effects experiments, which have been carried out under the

ANDANTE program. The experiments were novel in that they have broken down the under wing installation problem into two separate experiments, to allow us to distinguish between the wing reflection and jet refraction effects. Also advances in computational power has meant that many more microphones could be used during the tests, than has done in the past. This has given a much better resolution over a wider range of polar and azimuthal angles than ever before giving an unprecedented picture of the fully 3-D nature of installation effects problem.

We have reviewed the blockage data for a range of jet conditions, and have noted that a significant portion of the energy from the blockage region is redistributed by the jet. The effects of changing the temperature of the core have been noted to decrease the Δ SPL levels in the blockage region, while increasing Δ SPL levels outside of the blockage region. At realistic jet operating conditions, the changes made to the core and bypass temperatures and velocities, did not have a noticeable effect on the blockage Δ SPL levels or region. It should also be noted that at the lowest polar angles in the blockage region the results may be effected by the signal to noise ratio.

The data from the jet wing experiment has been reviewed for a range of realistic jet operating conditions. An understanding of the blockage problem has allowed for better interpretation of the jet wing results. Consistent difference in installed noise levels between jet conditions has been noted.

Having gained a better understanding of the problem we can now begin to predict these effects.

Chapter 5

A Semi-Empirical Model of Jet Wing Reflection

The focus of this chapter is the development of an engineering model which predicts jet noise installation effects for under wing mounted engines. The requirements of this model are that it be fast and robust, and that it can deal with a heated coaxial jet operating at realistic flight conditions. The structure of this chapter is as follows. In the introduction relevant literature on predicting installation effects is reviewed. Then an engineering installation effects model is described. The representation of the aircraft geometry is described. The following sections describe a number of the individual components of the installation model, including the jet blockage model, jet source distribution and directivity model. The installations model is then summarized, and validated using data from the ANDANTE programme of experiments. A further validation of the model is provided using a separate data set from an older experiment, followed by conclusions.

5.1 Introduction

It is the jet noise radiating close to the nozzle that suffers the most severe installation effects and this noise is of relatively high frequency. Thus a ray based approach is a natural choice and is the method adopted for the installation model.

The requirement is to model or predict the change in SPL (i.e. Δ SPL) occurring between isolated and installed engine noise sources, and in particular changes to the jet noise. As can be seen from the experimental data in the previous chapter the jet source reflects from the wing, and the reflected noise is refracted when propagating back through the jet to observers on the ground.

The method outlined in this chapter is an extension of the method outlined by Moore [12]. Moore describes a ray theory based model for predicting the reflection of engine noise by the underside of an aircraft wing. The model considers wing reflection for nozzle-based sources, combined with a 2-D empirical ‘acoustic blockage’ model, accounting for attenuation by the hot jet. In the model Moore represents the source by a monopole and assumes the medium is homogeneous, propagating the rays as straight lines.

The method outlined in this chapter extends the model developed by Moore, by considering the axially distributed jet source. Furthermore, using the newly acquired data from the ANDANTE tests, we develop a new point source blockage model, which importantly captures the redistribution of energy by the jet, something which was lacking from the Moore model. It is shown in this chapter that this point source blockage model can be applied effectively to the discretized jet source model outlined at the end of Chapter 2.

Another important ray-tracing approach to calculate installation effects is that of Agarwal et al [18]. The authors represent the forward propagating noise from the engine intake as a point source, using ray theory to calculate

the scattered field. Assuming that rays can be propagated as straight lines, the geometrical optics solution is extended to include the geometric theory of diffraction (GTD). This allows the model to account for the field in shadow zone using both edge diffracted and creeping rays. The method is validated using model scale experimental results, and numerical boundary element results. The extension of ray theory to include diffracted rays is omitted in our model, as the aircraft geometries we consider mean that the jet source is not shielded by the wing or fuselage, i.e. no shadow regions exist. Essentially this means that the direct and/or reflected rays can reach all parts of the field with which we are concerned. If we were to consider more novel aircraft geometries, GTD would be the natural extension of the theory.

In the following section the installations model is developed by extending the jet source model from chapter 2.

5.2 Installations Model

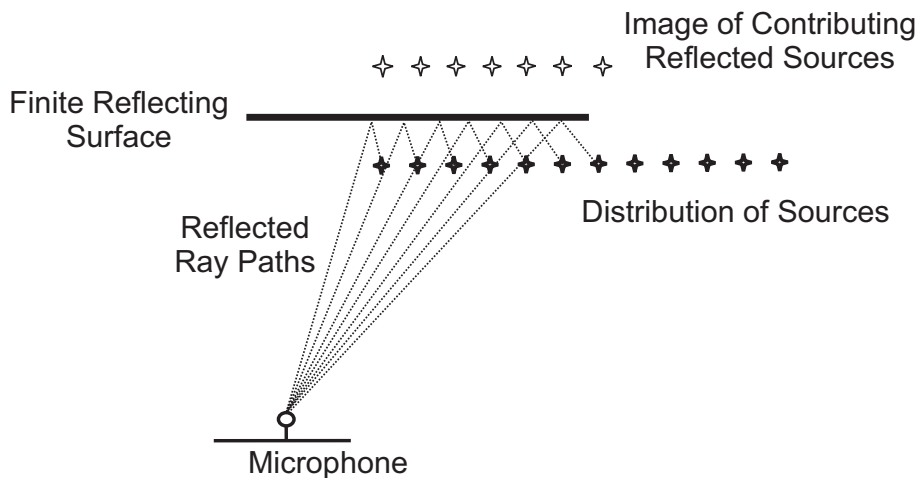


Figure 5.1 – Ray paths of sources which are reflected from surface/wing.

The requirement is to develop a model which can predict the change in sound pressure level due to the installation of the jet source below the wing. In the ANDANTE jet wing experiment outlined in chapter 3, this change in

sound pressure level is measured, and it was previously defined in equation 4.2 as

$$\Delta SPL = SPL_{installed} - SPL_{jet}. \quad (5.1)$$

A simple jet source model was outlined in chapter 2. Equation 3.37 defined the sound pressure level due to the jet source as

$$SPL_{jet} = 10 \log_{10} \left(\frac{\sum_{i=1}^n \left| \frac{A_i d_i}{4\pi R_i} \right|^2}{p_{ref}^2} \right). \quad (5.2)$$

The installed level can be defined as the isolated jet source plus some addition reflected source, the ray paths of the reflected sources are outlined figure 5.1.

The reflected rays may pass through the jet after being reflected and this is something that also need to be considered in the model.

Assuming that the reflected source is totally incoherent from the jet source in far field, the pressure amplitudes can be summed, to give the installed sound pressure level as

$$SPL_{installed} = 10 \log_{10} \left(\frac{\sum_{i=1}^n \left| \frac{A_i d_i}{4\pi R_i} \right|^2 + \sum_{j=1}^m \left| \frac{A_j d_j b_j}{4\pi R_j} \right|^2}{p_{ref}^2} \right), \quad (5.3)$$

where m are the number of reflected sources, and $b_j(\theta, \phi, f, J_c)$ is a jet blockage function of position, frequency and jet conditions $J_c = \{u_p, u_s, T_p, T_s\}$, which is yet to be defined. Combining the three previous equations, the installation change in sound pressure level can now be written independently of a reference pressure as

$$\Delta SPL = 10 \log_{10} \left(1 + \frac{\sum_{j=1}^m \left| \frac{A_j d_j b_j}{R_j} \right|^2}{\sum_{i=1}^n \left| \frac{A_i d_i}{R_i} \right|^2} \right). \quad (5.4)$$

The basic equation for determining installation levels has been formulated.

In the following sections some time is taken to explain how the individual components of the model are determined, principally the source distribution, directivity and blockage functions.

In the next section the aircraft geometry and reflections from multiple panels are considered.

5.3 Aircraft Geometry and Reflections

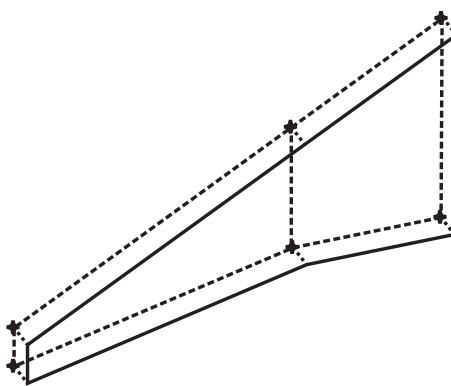


Figure 5.2 – Wing geometry is represented by a number of quadrilateral finite surfaces, each represented in the model by its four vertices. The flat plate wing used in the ANDANTE tests can be represented by two quadrilaterals.

For the purposes of our model the geometry is represented by a number of finite quadrilateral panels, each one is defined using its four vertices, see figure 5.2. This allows us to represent the flat plate wing geometry used in the experiment almost perfectly, which in turn is a reasonable approximation to a realistic aircraft geometry.

By keeping the geometry relatively simple, secondary reflections from panel to panel need not be considered. The total reflected source is equivalent to the sum of the sources reflected from each panel.

For each of the discretized monopole sources representing the jet, the model assumes perfect reflections from the aircraft geometry. If we consider one source reflecting from one panel, we can use the image source to deter-

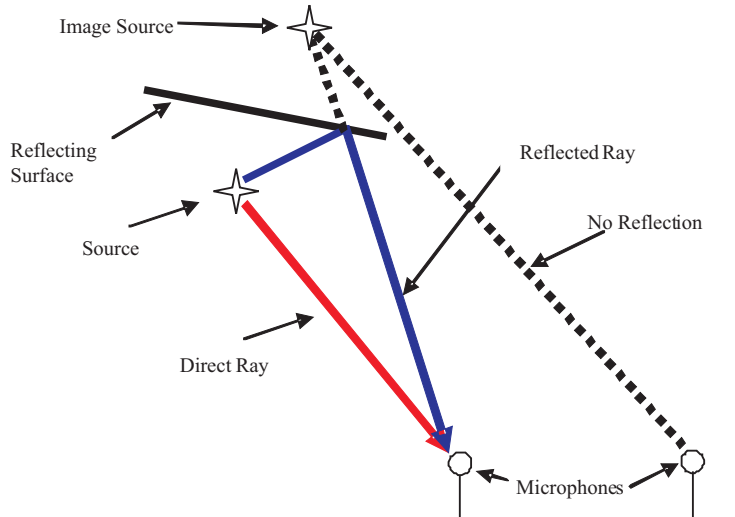


Figure 5.3 – The above diagram illustrates how the method determines if a reflection from a finite panel, for a particular source, has reached an observer.

mine if a particular observer can see a reflection, see figure 5.3. Thus for a geometry with multiple panels the total reflected pressure amplitude pressure, for a fixed observer position, can be written as the sum of the reflected source from each panel. That is to say,

$$\text{SPL}_{\text{installed}} = 10 \log \left(\frac{\sum_{i=1}^n \left| \frac{A_i d_i}{4\pi R_i} \right|^2 + \sum_{i=1}^p \sum_{j=1}^{m_i} \left| \frac{A_j d_{ij} b_{ij}}{4\pi R_{ij}} \right|^2}{p_{\text{ref}}^2} \right), \quad (5.5)$$

where R is the distance traveled along the reflecting ray path, p is the number of panels, m_i are the number of reflected sources from a particular panel, and where the subscript i denotes it the particular panel upon which m is dependent. This allows us to rewrite equation 5.4 as:

$$\Delta \text{SPL} = 10 \log \left(1 + \frac{\sum_{i=1}^p \sum_{j=1}^{m_i} \left| \frac{A_j d_{ij} b_{ij}}{R_{ij}} \right|^2}{\sum_{i=1}^n \left| \frac{A_i d_i}{R_i} \right|^2} \right). \quad (5.6)$$

Of course reflected rays may pass through or be refracted by the jet after being reflected, as represented by the blockage b_{ij} . This is something which

is considered in the following section.

5.4 Jet Blockage Model

The hot jet exhaust can have a temperature and velocity gradient which causes refraction or ‘blockage’ of the reflected noise, such effects have been described by Moore and Mead [13]. A number of approaches to modeling this have been adopted and are outlined by Powles and Tester [28]. In this section of the chapter a more pragmatic approach has been adopted for the purposes of including in the engineering model.

Using the data from ‘the point source above the jet experiment’, which was experiment 1 outlined in chapter 3, a semi-empirical point source blockage model is developed in the following sub-section.

5.4.1 An Empirical Blockage Model

Although the blockage effects can be modeled numerically and analytically [28] , these methods have proven to be both computationally expensive and time consuming. Basic ray theory for an idealised ‘plug flow’ jet has also been shown to have significant limitations [45]. For these reasons it was decided that for the purpose of this engineering model it would be more accurate and involve fewer assumptions to implement a semi-empirical model developed using data from experiment 1. The experimental blockage measured was defined in chapter 4 as

$$B(\phi, \theta, f, J_c) = \Delta \text{SPL} = \text{SPL}_{jet} - \text{SPL}_{ff}, \quad (5.7)$$

where SPL_{jet} is the sound pressure level due to the source propagating through the jet, and SPL_{ff} is the sound pressure level due to the source in the free field, i.e. in the chamber with jet switched off. This measurement can be applied to our installations jet noise model as a correction. This can

be related the blockage function defined in equation 5.4 by

$$b(\phi, \theta, f, J_c) = 10^{(B/20)}. \quad (5.8)$$

The blockage data from experiment 1 was reviewed in chapter 4 where it was concluded that at the realistic jet operating conditions, i.e. conditions ranging from approach to sideline, the variation in blockage levels is small, see figure 4.8.

Thus for the the purposes of the installation prediction model it can be assumed that the blockage is independent of jet condition, at the range of realistic jet operating conditions for which the model is required to predict for, i.e.

$$b(\phi, \theta, f) = b(\phi, \theta, f, J_c) \quad (5.9)$$

It was decided to take an average of the blockage data for jet conditions ranging from approach to sideline. This has two advantages, firstly it would give a more accurate result when applying the model to the same range of realistic jet conditions, and secondly it helps smooth the interference pattern which is a feature of harmonic point sources but would not be a feature of broadband jet sources to which the end result will be applied.

Taking the average of the four blockage maps, for conditions ranging from approach to sideline, fourth-order polynomials are fitted using a least-squares fit to the data at each polar angle for a range of azimuthal angle. This generates a family of eight curves, which describe the change in SPL at eight polar angles and for a range of azimuthal angles, for each of the six measured frequencies. It was decided to use fourth order polynomials as it was though that they would adequately capture the two hump shape of the data. The derivatives of the curves were forced to zero at zero azimuthal angle, to make the blockage curves axi-symmetric.

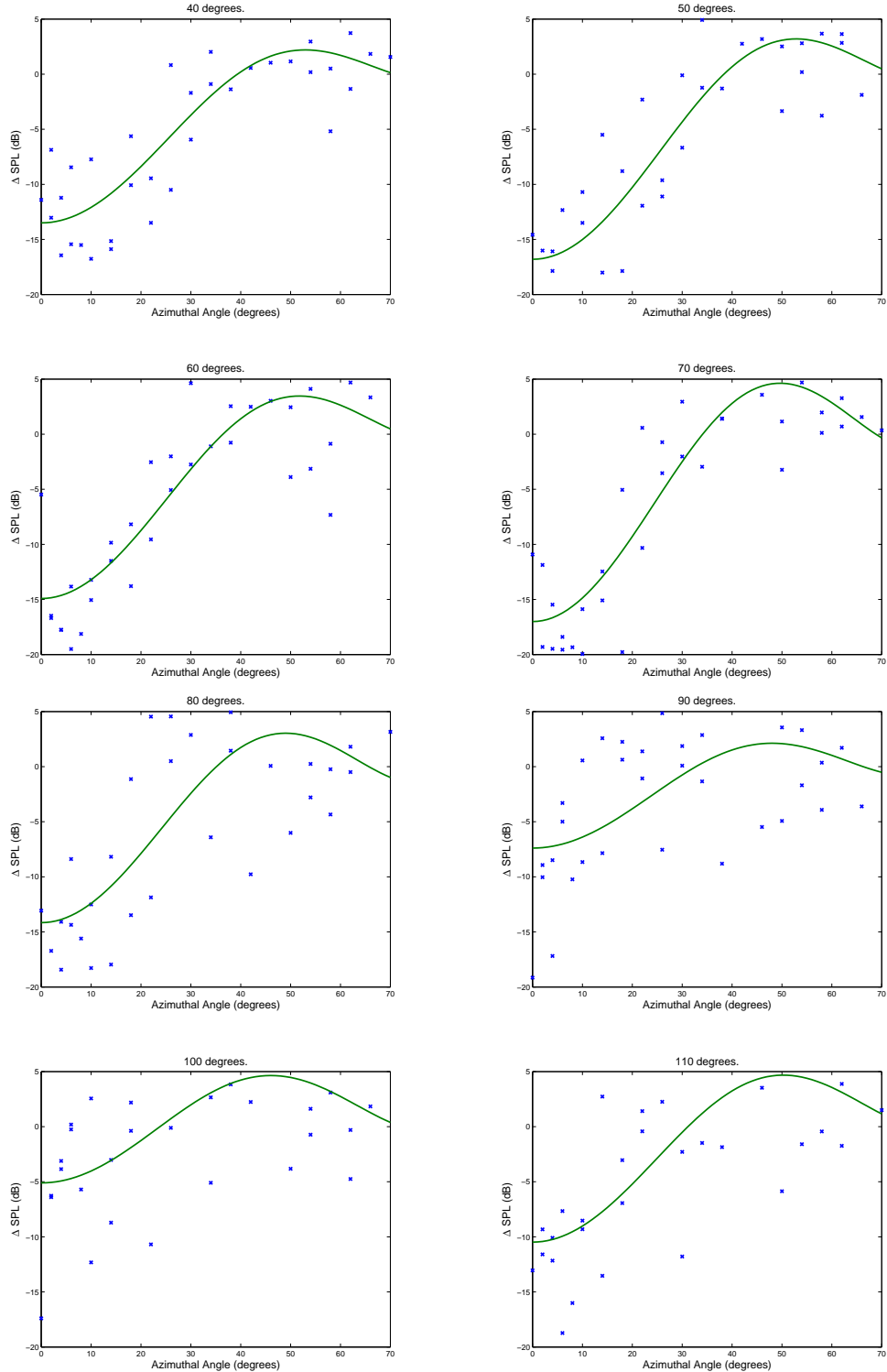


Figure 5.4 – Jet blockage data and fitted curves for 10kHz(model scale) external source for a high powered jet. ΔSPL is plotted against azimuthal angle in degrees, where zero degrees is directly below the jet.

Figure 5.4 shows the curves fitted to the data for the external source driven at 10kHz. Although the data has some scatter, the general trend of the fitted curves behave as expected, ie the blockage and refraction effects are more significant at lower polar angles. The graphs are plotted over polar angles ranging from zero to sixty degrees. There was good microphone resolution over that polar range in experiment 1, as this is the region of interest.

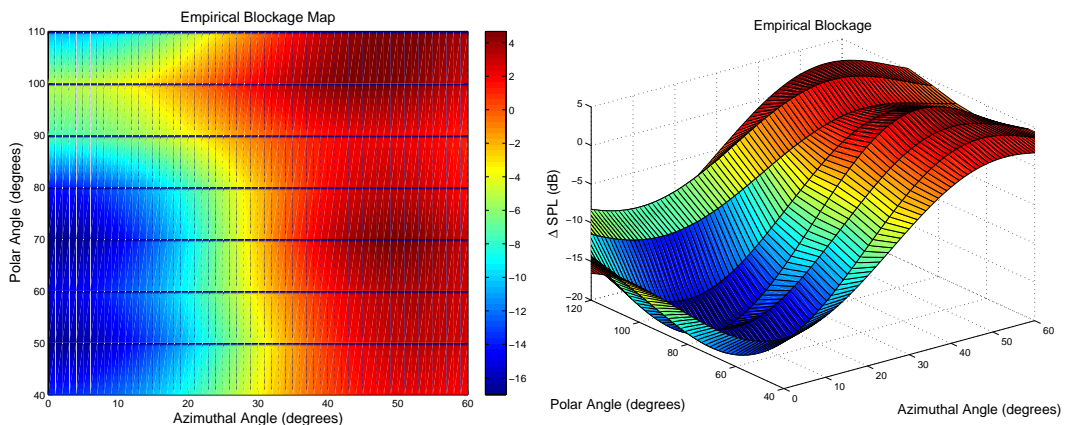


Figure 5.5 – Empirical Hot Jet Blockage Map and Surface Plot for 10kHz(model scale) external source for a jet at realistic operating conditions, generated from curves in figure 5.4.

Using each family of curves we can create a fully interpolated map of the blockage region which can then be used to create a semi-empirical blockage model for a single frequency point source, figure 5.5 shows plots of the 10kHz blockage map. The has figure also been plotted as a surface plot to provide a better visual impression of the redistribution of the sound. Note that this is model-scale frequency, equivalent to 938Hz at full scale.

This process was repeated to create a blockage map for each of the six measured external source frequencies. These blockage maps for six discrete frequencies can be then linearly interpolated between, to give an estimate of the blockage at any frequency, for any polar and azimuthal angle within the given range of the blockage maps. That is to say the blockage at any

frequency f , can be defined as

$$B(\theta, \phi, f) = B_m(\theta, \phi, f_L) + \frac{(f - f_L)}{(f_H - f_L)}(B_m(\theta, \phi, f_H) - B_m(\theta, \phi, f_L)) \quad (5.10)$$

where B_m is the measured blockage data, f_L and f_H are the two discrete frequencies at which data was taken, closest to the required frequency f . f_H represents the higher of the two measured frequencies, and f_L is the lower of the two measured frequencies.

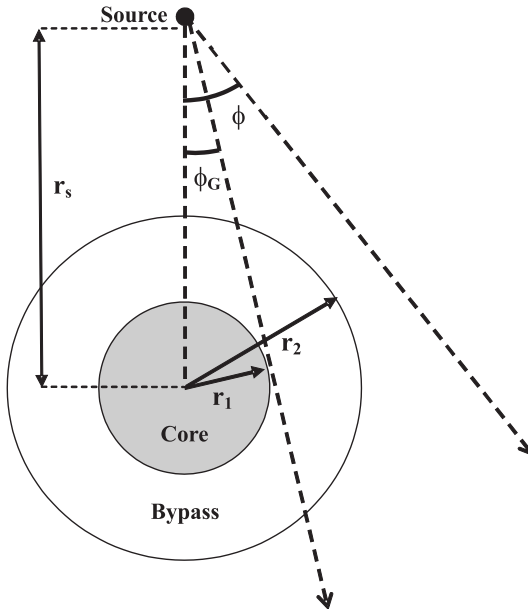


Figure 5.6 – Diagram outlining angles used to scale jet blockage data. ϕ is any azimuthal angle, and ϕ_G is the angle of a ray at grazing incidence to the core.

When considering a heated coaxial jet the number of parameters which can vary is large. There are two temperatures, two velocities, and two diameters, and obviously the position of the source can also vary. This can make scaling the empirical blockage map difficult, thus a number of assumptions are made.

As data used for the blockage maps are for a fixed source position we

require some method to scale these results so that we can apply them to a source in any position for a range of different jet nozzles. Having already assumed that the blockage does not change at the realistic jet operating conditions, we assume that the model can be applied to a range of similar jet conditions on other jet nozzles. Given that the model is only based on data from one nozzle, we assume that we can only apply the model to nozzles with the same ratio of bypass to core radius, ie $r_1/r_2 = \text{const}$ see figure 5.6. It is also assumed that there is no variation when the source is moved in the axial direction, and that the jet is perfectly axi-symmetric. Given these assumptions we can then scale these results using the angle of the ray grazing the core of the jet. The angle of the ray grazing the core, ϕ_G , is a function of the radius of the core, r_1 , and distance of the source from the center line of the jet, r_s . This particular angle is used as changing the source position or changing the jet radius is effectively the same thing for an axi-symmetric problem. Thus we are also assuming that changing the source position does not change blockage levels, but simply the shape of blockage region. We can stretch or compress the azimuthal angle of the measured data using a scaling factor based on the ratio of the grazing angles.

That is to say for a different jet with a source in a new position, and the receiver at an angle ϕ_{new} , the angle to be taken from the blockage map, ϕ_{map} , is

$$\phi_{map} = \alpha \phi_{new}, \quad (5.11)$$

where α is scaling factor given by

$$\alpha = \frac{\phi_{G_{new}}}{\phi_{G_{map}}} \quad (5.12)$$

where $\phi_{G_{new}}$ is the grazing angle of the new source and jet, and $\phi_{G_{map}}$ is the grazing angle of the source and jet used in experiment 1. Figure 5.7 demonstrates how the scaling factor work.

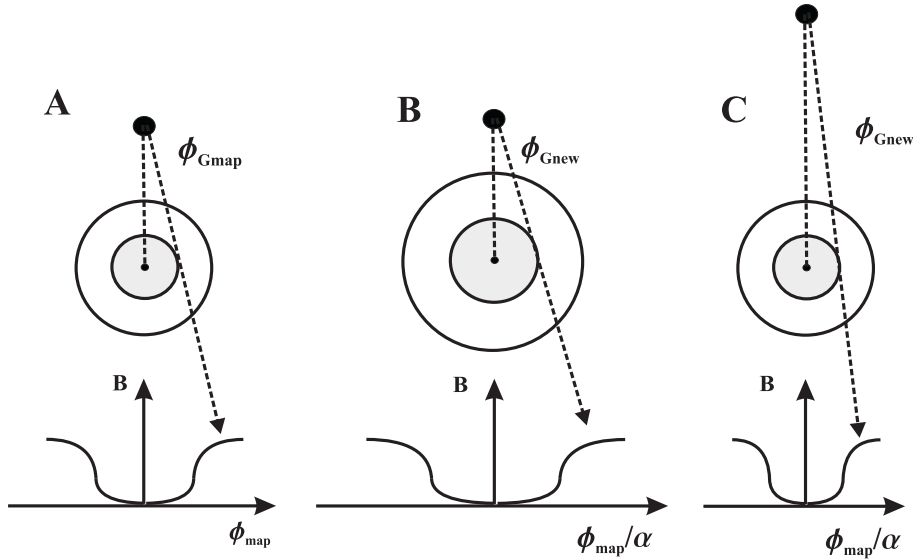


Figure 5.7 – Diagram demonstrating how the blockage is scaled. A) Measured blockage data B) Estimated blockage for increased jet radius C) Estimated blockage for change of source position.

In summary, we can use this angle to normalize the absolute angle of the empirical jet blockage results, so that they can be used for a point source in any location for a jet of any radius, given the following assumptions:

- the jet is axi-symmetric,
- the jet has similar core to bypass radius ratio,
- the source is in a similar axial position as the measurements,
- the jet has similar operating conditions as to that of the measurements,
- changing source position or jet radius does not change the blockage level, but only the shape of the blockage region.

Thus using the data base from experiment 1, the blockage function can be defined

$$B(\theta, \phi, f) = B_m(\theta, \alpha\phi, f_L) + \frac{(f - f_L)}{(f_H - f_L)}(B_m(\theta, \alpha\phi, f_H) - B_m(\theta, \alpha\phi, f_L)). \quad (5.13)$$

5.5 Jet Source Distribution

It was mentioned in Chapter 3 that predicting the distribution of the jet noise source is a difficult task, and we outlined some semi-empirical methods.

However, for a heated coaxial, given all the parameters which may vary, accurately determining the source distribution using a semi-empirical model becomes impractical. For this reason we rely on empirical jet source distributions measured using polar correlation techniques. The measurements were made on a static rig tests using a nozzle which has a similar geometry to the nozzle used in the ANDANTE tests, i.e. the ratio of core diameter to bypass diameter.

The polar correlation technique determines, S , source strength per unit length. This is an extension of the basic concept to a line array of uncorrelated harmonic sources (i.e with random phase) representing the jet source [31]. This quantity can be related to our relative amplitude function from equation 5.4, where the relative amplitude of portion of the jet of length Δx at a position x is

$$A_{\Delta x}(x, f, J_c) = \frac{\int_x^{x+\Delta x} S(f, J_c) dx}{\int_0^\infty S dx}. \quad (5.14)$$

Examples of measured jet source distributions used can be seen in figure 5.8. There are two contour plots showing the axial source distribution, for a range of frequencies, measured at jet conditions approach and cutback respectively. It is clear from the both plots that the source distribution is frequency dependent. It is also clear that the source distribution changes with jet condition.

A Strouhal number for a coaxial jet can be defined

$$St = f D_s / U_s \quad (5.15)$$

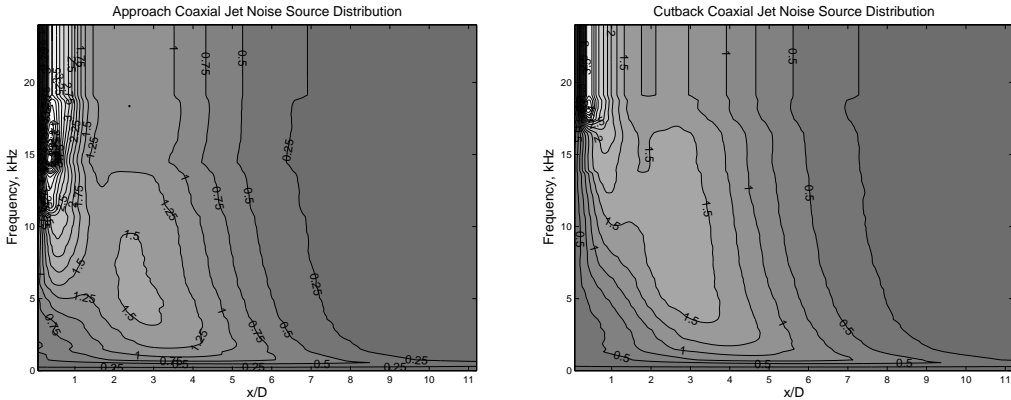


Figure 5.8 – Measured jet source distributions, at conditions Approach and Cutback, measured using polar correlation technique.

where f is the frequency, D_S is the secondary nozzle diameter, and U_S is the velocity of bypass. The Strouhal number is based on the parameters of the engine bypass as that is where the majority of high frequency sources lie, which are subject to wing reflections.

Figure 5.9 shows line plots for the measured source distributions for a range of Strouhal numbers for conditions equivalent to the Approach and Cutback jet conditions in experiment 2, outlined in chapter 3. Although source distributions for specific frequencies at both conditions can be quite different, as one would expect the plots for equivalent Strouhal numbers show little difference.

Thus in the installations prediction method the relative amplitude, is a function of axial position and Strouhal number. The distribution is approximated to one of a series of polynomials fitted to the average of the two measured conditions, based on discrete Strouhal number ranging from 1 to 10. The average polynomials have also been plotted in figure 5.9, and can be seen to give an accurate representation of the measured data, at a selected range of six discrete Strouhal numbers.

Now

$$A_{\Delta x}(x, St) = \frac{\int_x^{x+\Delta x} S_p(St) dx}{\int_0^{\infty} S_p dx}, \quad (5.16)$$

where S_p represents a polynomial fit to the measured source distributions.

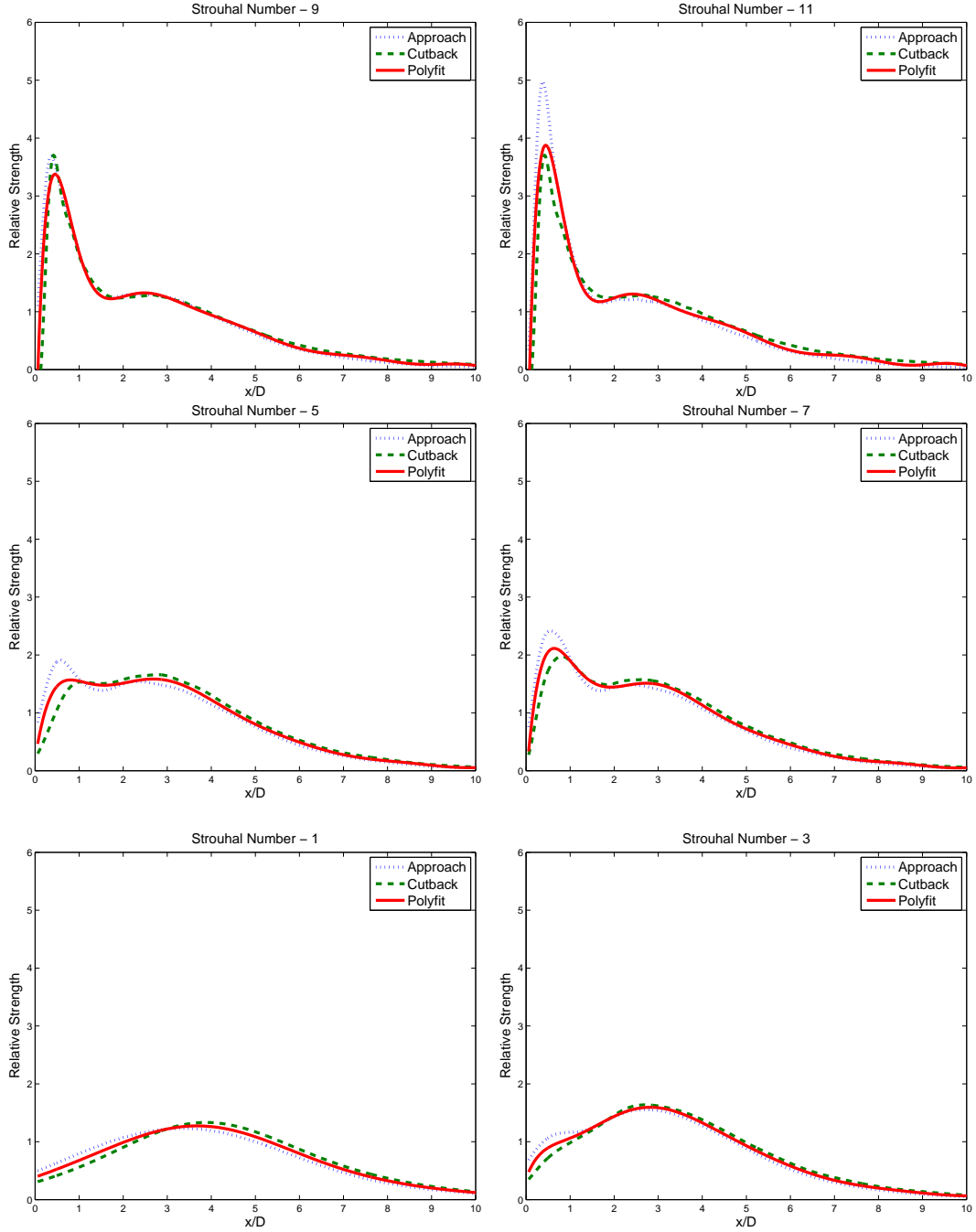


Figure 5.9 – Measured jet source distributions, for a range of six Strouhal numbers.

5.6 Jet Source Directivity

A distributed jet source is highly directional and understanding the directivity is important when determining the three dimensional nature of the installed levels.

Experimentally the directivity for an axisymmetric jet was defined as

$$D(\theta, f, J_c) = \Delta SPL(\theta, f, J_c) = SPL(\theta, f, J_c) - SPL(90). \quad (5.17)$$

which can be related to the directivity function defined in equation 3.37, the jet source model in chapter 2, by

$$d(\phi, \theta, f, J_c) = 10^{(D/20)}. \quad (5.18)$$

Measured directivities for jet conditions Approach and Cutback from the experiment 1 of ANDANTE tests, for a range of 1/3 octave band frequencies, are plotted in figures 5.10 and 5.11 respectively.

As can be seen from the plots, the directivity is generally independent of frequency (particularly at higher frequencies) at most angles, hence we define a directivity function independent of frequency. However it is noted that directivity does change with jet condition. The average of the directivities was taken to give an OASPL directivity. A polynomial was fitted to the OASPL directivity. The OASPL has been overlaid on the data sets in both figures 5.10 and 5.11.

To make directivity predictions at different engine conditions the prediction method uses the polynomials fitted to the cutback and approach OASPL directivities. For a fixed polar angle the method linearly interpolates between the two curves using the secondary velocity of the jet, i.e.

$$D(\theta, u_s) = D_m(\theta, u_a) + (D_m(\theta, u_c) - D_m(\theta, u_a)) \frac{(u_s - u_a)}{(u_c - u_a)}, \quad (5.19)$$

where D is the OASPL directivity, u_s is the secondary velocity of the jet, subscript m denotes measured OASPL directivity, and subscripts a and c , refer to measured approach and cutback secondary jet velocities respectively.

Again the reason that this parameter was used when scaling the result, was because the majority of the high frequency sources are in the secondary shear layer, thus one would expect them to be a function of secondary velocity. Figure 5.12, shows that scaling based on the secondary velocity gives very good agreement with the measured OAPSL directivity data at the intermediate condition.

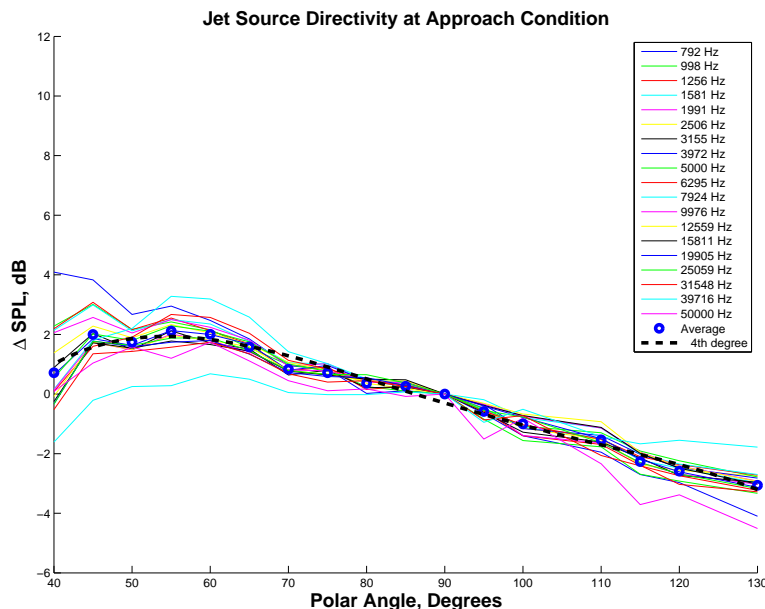


Figure 5.10 – Jet source directivity at Approach condition, measured on polar array during ANDANTE tests, normalised using the source strength at polar angle 90°.

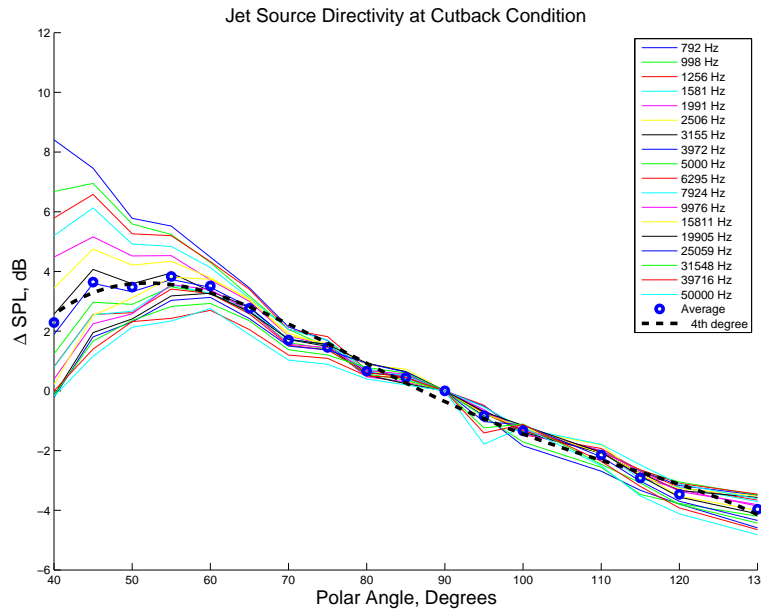


Figure 5.11 – Jet source directivity at cutback condition, measured on polar array during ANDANTE tests, normalised using the source strength at polar angle 90° .

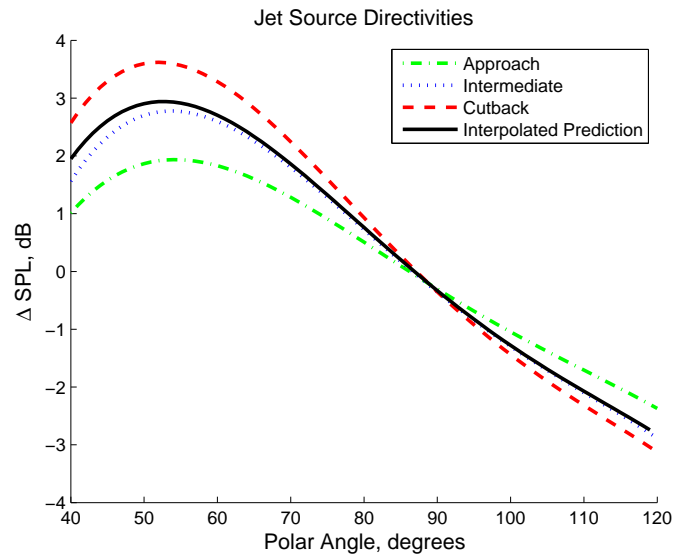


Figure 5.12 – OASPL jet source directivities at Approach, Intermediate and Cutback, and interpolated Intermediate prediction.

5.7 Prediction Method Summary

The purpose of the model is to determine the change in sound pressure level (ΔSPL) at a given ground microphone position due to the installation effects, for a jet source mounted below a wing. The installation model was defined in equation 5.4. Having reviewed and described each of the individual components of the model in the previous four sections, the model can now be written

$$\Delta SPL(D_s, u_s, f, \theta, \phi) = 10 \log \left(1 + \frac{\sum_{i=1}^p \sum_{j=1}^{m_i} \left| \frac{A_j(x, St) d_{ij}(\theta, u_s) b_{ij}(\theta, \phi, f)}{R_{ij}} \right|^2}{\sum_{i=1}^n \left| \frac{A_i(x, St) d_i(\theta, u_s)}{R_i} \right|^2} \right), \quad (5.20)$$

where each component is defined solely as function of the specific jet parameters which we have determined they are dependent.

As part of the ANDANTE project a Fortran 90 prediction code was developed. The purpose of the model is to determine the change in sound pressure level (ΔSPL) at a given ground microphone position due to the installation effects. The structure of the code is outlined in figure 5.13.

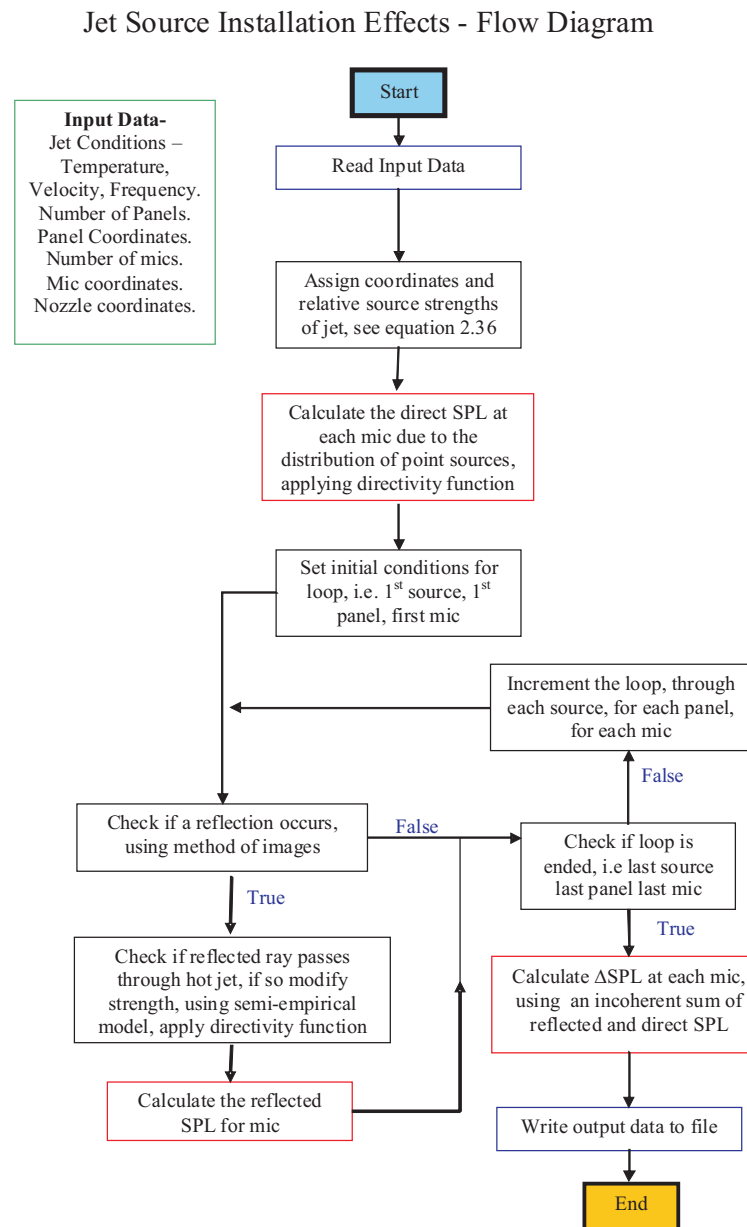


Figure 5.13 – Flow diagram, outlining the primary survey used in the Fortran 90 prediction method.

5.8 Validation of the Prediction Method

The installation effects prediction method is firstly validated using data from the ANDANTE tests outlined in chapter 2, experiment 2, quantifying the effects of placing a model wing above a jet. All the figures presented in the results section, are presented for predicted and measured values of ΔSPL . Results are plotted for two jet operating conditions approach, in figures 5.14 - 5.19, and sideline, in figures 5.20 - 5.25. For each jet condition noise levels are plotted for a range of six 1/3 octave band frequencies. The model scale frequency range is 792 Hz - 25059 Hz, which relates to a full scale frequency range of 49.5 Hz - 1566 Hz.

Each figure contains six sub-plots, where each sub-plot has ΔSPL plotted against azimuthal angle for a single polar angle, where the polar angle relates to a single traverse position of the axially traversing array.

The predictions at the lower powered approach jet condition are accurate across the full range of frequencies, generally predicting the measurements to within less than a decibel, particularly at higher polar angles where the method predicts to within less than half a decibel. At the very lowest frequency, 792 Hz figure 5.14, the prediction is good at lower polar angles. At higher polar angles, i.e. below the jet nozzle and upstream of the nozzle, we can see the method under predicting. This is likely to be due to jet wing interaction, a low frequency phenomenon, which is not considered in this model. However, at all frequencies above this the prediction method captures the shape of data well at most polar and azimuthal angles. There does seem to be some consistent disagreement with the prediction and measured data at lower polar angles, i.e. 50 and 60 degrees. This may be due to the assumption that jet source directivity is independent of frequency, as this assumption does seem to break down at lower polar angles, i.e. in the cone of silence, see figure 5.10.

At the higher powered sideline jet condition, we again see good agreement

generally across the full range of frequencies, less than a decibel between predicted and measured data, with the exception of the lowest frequency, 792 Hz figure 5.20. At this higher powered jet setting the low frequency jet wing interaction noise is much more dominant, and as we previously mentioned this is not included in the model. There also seem to be some scatter in the data at 15881 Hz in figure 5.24, which may be due to a core siren in the experiment which began to misbehave at the more extreme temperature setting of the sideline jet condition.

At the sideline jet condition the results are also accurate at lower polar angles of 50 and 60 degrees. This would suggest that the assumption of the directivity being independent of frequency was not the cause of the method under predicting at low polar angles at the lower jet powered jet condition approach. Another possible assumption which could lead to this error, was the assumption that the jet blockage was independent of jet condition.

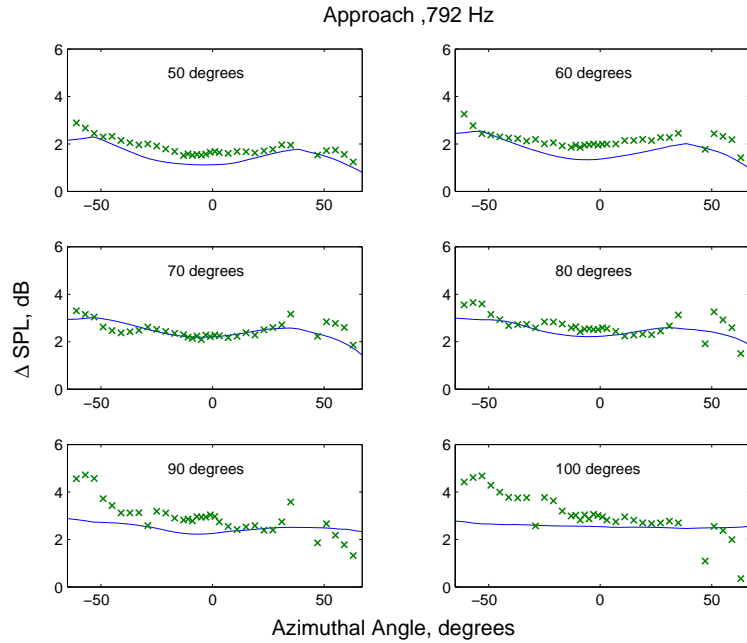


Figure 5.14 – Approach Jet condition at 792Hz, comparison of a prediction versus measured data, ΔSPL is plotted against azimuthal angle for a range of six polar angles.

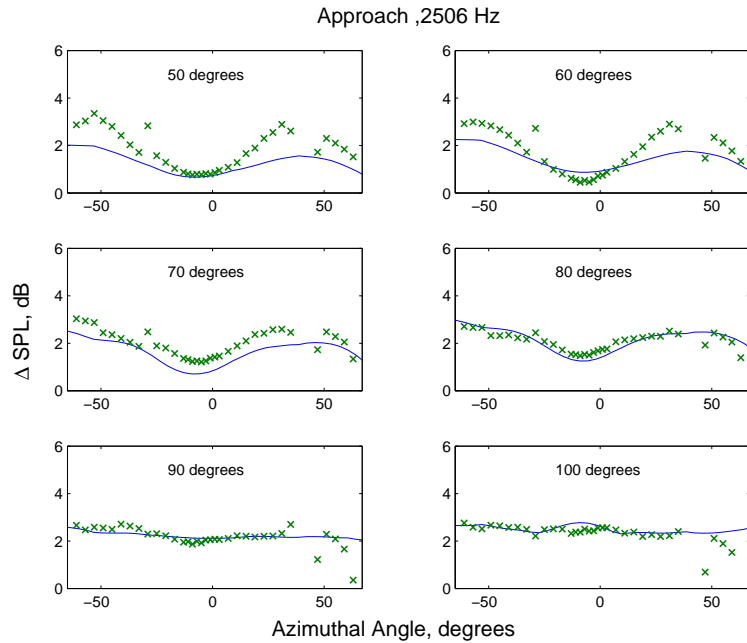


Figure 5.15 – Approach Jet condition at 2.5kHz, comparison of a prediction versus measured data, ΔSPL is plotted against azimuthal angle for a range of six polar angles.

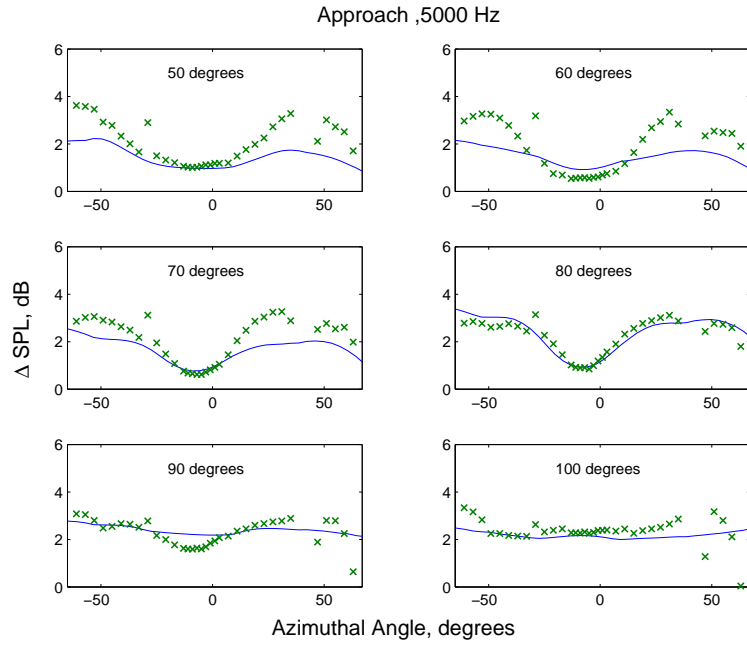


Figure 5.16 – Approach Jet condition at 5kHz, comparison of a prediction versus measured data, Δ SPL is plotted against azimuthal angle for a range of six polar angles.

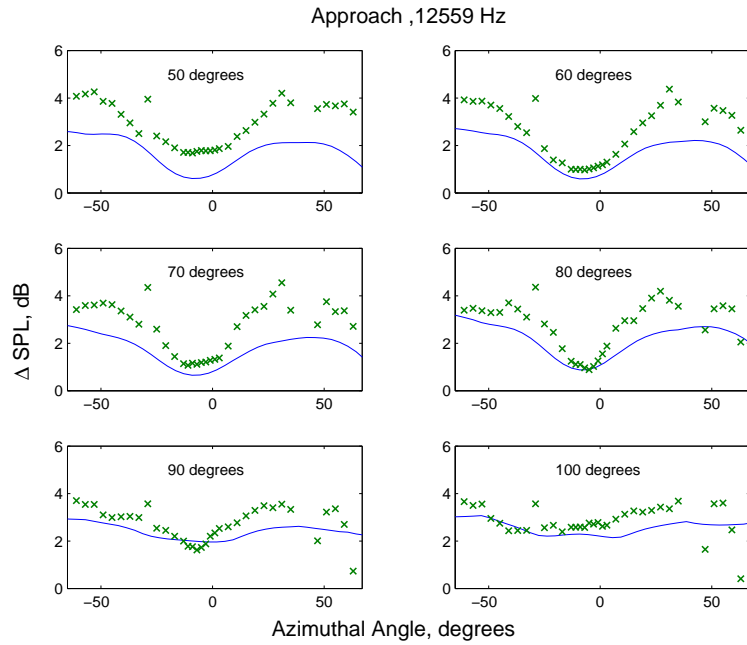


Figure 5.17 – Approach Jet condition at 12.5kHz, comparison of a prediction versus measured data, Δ SPL is plotted against azimuthal angle for a range of six polar angles.

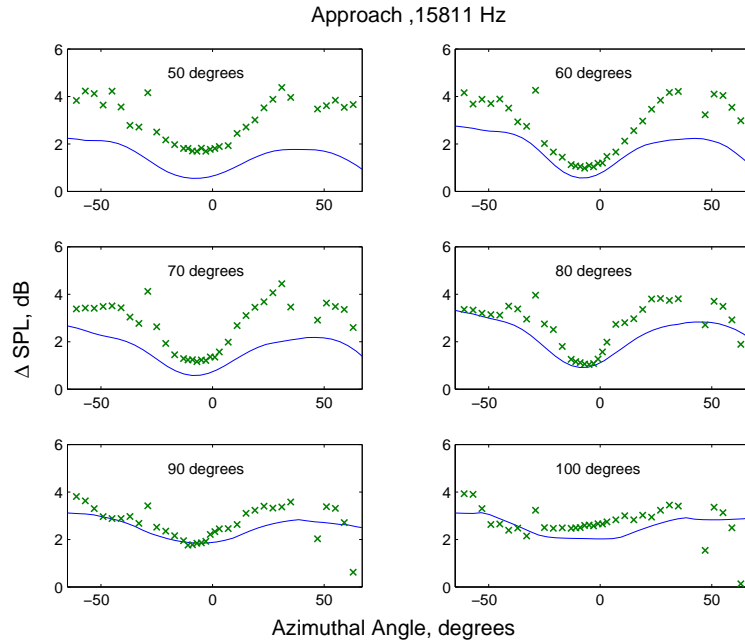


Figure 5.18 – Approach Jet condition at 15kHz, comparison of a prediction versus measured data, ΔSPL is plotted against azimuthal angle for a range of six polar angles.

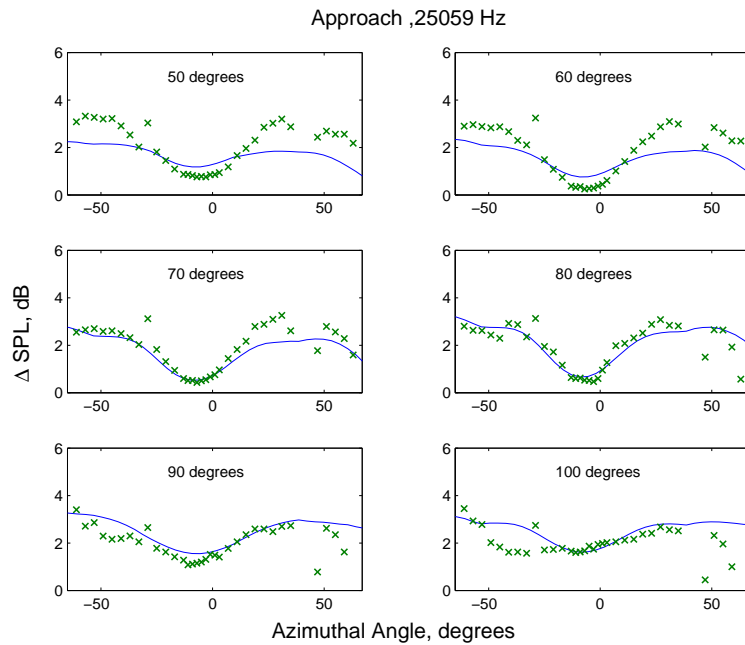


Figure 5.19 – Approach Jet condition at 25kHz, comparison of a prediction versus measured data, ΔSPL is plotted against azimuthal angle for a range of six polar angles.

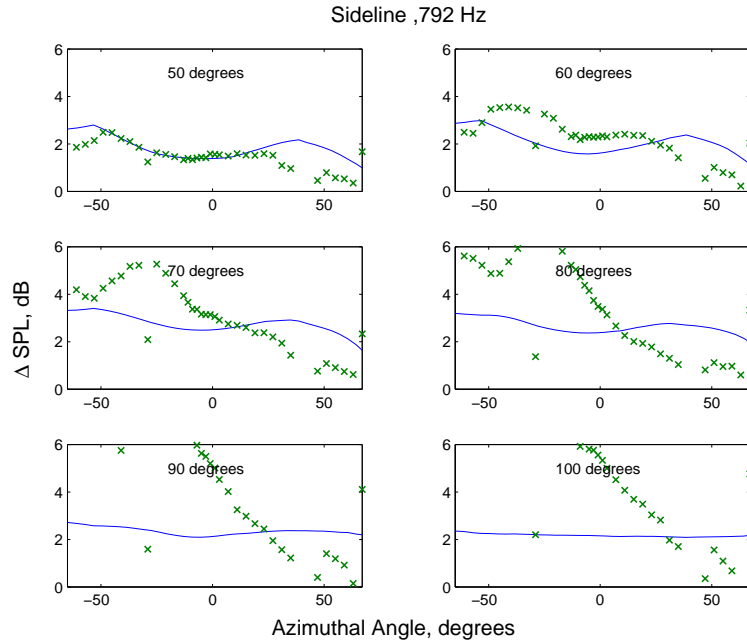


Figure 5.20 – Sideline Jet condition at 792Hz, comparison of a prediction versus measured data, ΔSPL is plotted against azimuthal angle for a range of six polar angles.

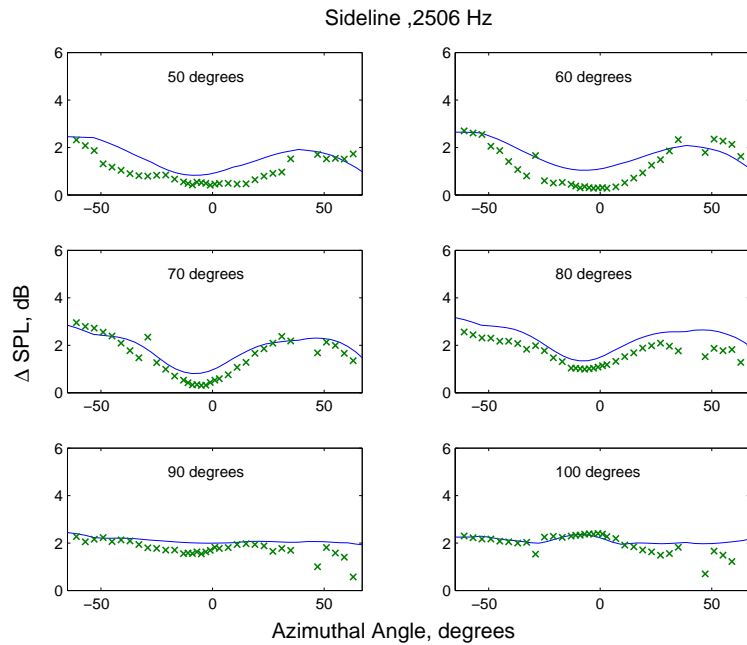


Figure 5.21 – Sideline Jet condition at 2.5kHz, comparison of a prediction versus measured data, ΔSPL is plotted against azimuthal angle for a range of six polar angles.

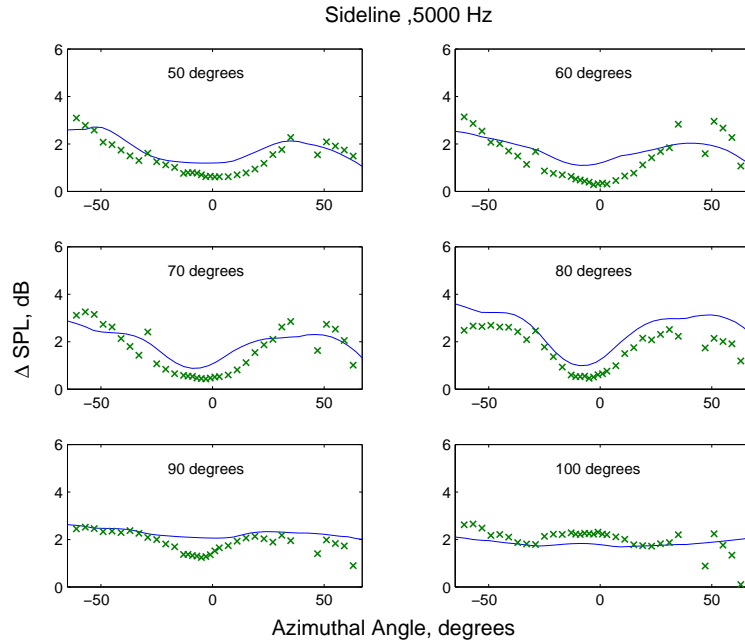


Figure 5.22 – Sideline Jet condition at 5kHz, comparison of a prediction versus measured data, ΔSPL is plotted against azimuthal angle for a range of six polar angles.

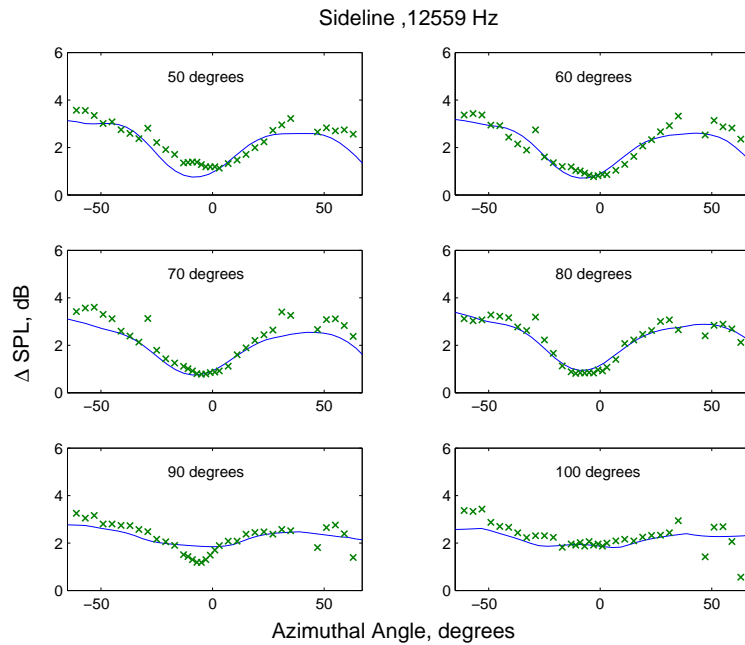


Figure 5.23 – Sideline Jet condition at 12.5kHz, comparison of a prediction versus measured data, ΔSPL is plotted against azimuthal angle for a range of six polar angles.

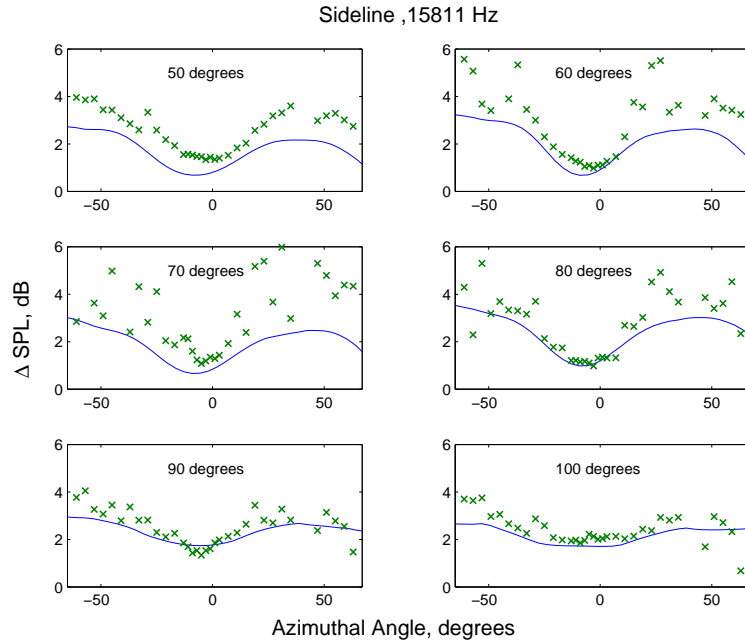


Figure 5.24 – Sideline Jet condition at 15kHz, comparison of a prediction versus measured data, ΔSPL is plotted against azimuthal angle for a range of six polar angles.

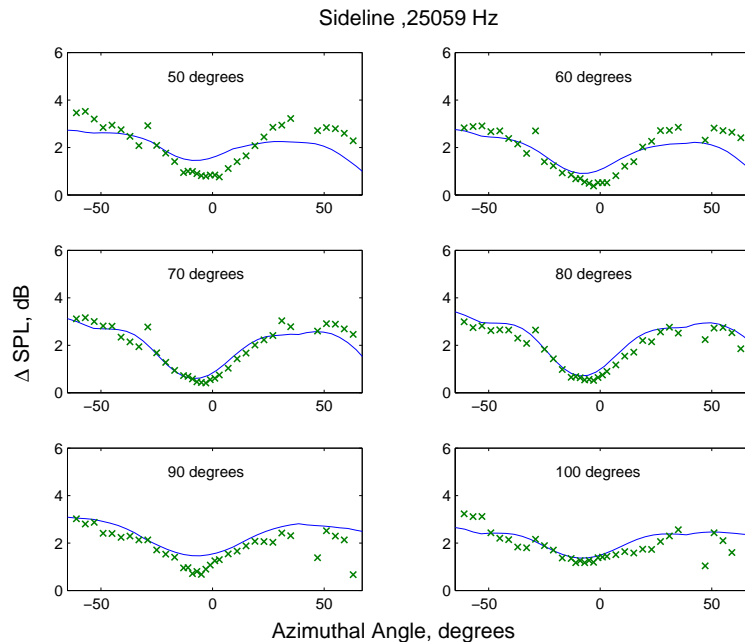


Figure 5.25 – Sideline Jet condition at 25kHz, comparison of a prediction versus measured data, ΔSPL is plotted against azimuthal angle for a range of six polar angles.

5.9 Further Validation

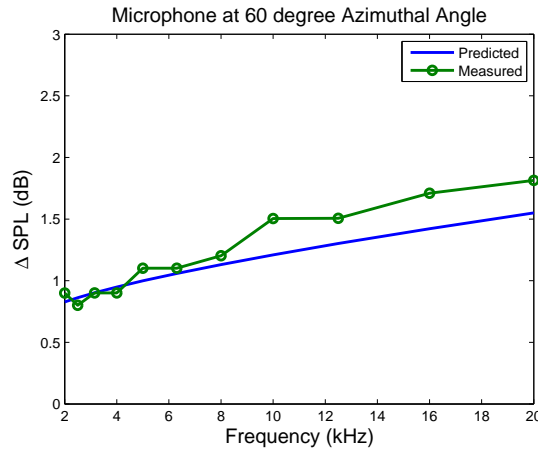


Figure 5.26 – Using a new data set - a comparison of prediction verses measured, ΔSPL is plotted for a single microphone, at 90 degrees polar angle, and 60 degrees azimuthal angle, for a range frequencies.

The semi-empirical point source blockage model was based on data measured using the same nozzle with same jet conditions as jet wing experiments, with which we validated the installation effects prediction method. To provide further validation for the semi-empirical prediction method we now apply the model to a different set of experimental data, using a different nozzle. We use data from Mead and Strange [11] 1/18th scale model tests from 1998. The experimental setup was similar to the ANDANTE experiment 2, outlined in chapter 2, in that they measured the change in SPL, on an azimuthal array, due to placing a model wing above a jet.

The wing was an 1/18th scale plan form cut out of typical two-engine aircraft. The azimuthal microphone array was at 90 degrees polar angle to the jet. Details of the wing and array are outline in the paper [11].

The nozzle geometry used for the test was of a typical modern aeroengine with a by pass ratio of four, where the core and by pass streams merge before being exhausted. Results where obtained for a range of jet flow conditions. For the purpose of validation of the method presented in this chapter we will

consider the data from the flow conditions simulating a static single stream jet. The velocity of the jet, U , is 326.6m/s , and the diameter of the nozzle, D , is 0.081m .

The source distributions are based on the single stream jet formula proposed by Szewczyk [46], using measured centroid data supplied by Rolls Royce.

Fewer microphones were used in this set of tests. Figure 5.26 shows predictions and measured data for a single microphone, at a polar angle of 90 degrees, and an azimuthal angle of 60 degrees. The change in SPL due to placing the wing above the jet is plotted against frequency. At this particular microphone we can see the predictions are within 0.25dB of the measured data over a full range of model scale frequencies.

Figure 5.27 has four sub-plots each for a different model scale frequency. Each sub-plot show measured and predicted delta SPL's for a range of azimuthal angle. The data was measured on the azimuthal array which was at 90 degrees polar angle to the jet. The predictions are within 0.25dB of the measurements, with the exception of the 2kHz plot, where the reflection data is possibly being contaminated with lower frequency jet wing interaction effects.

5.10 Conclusions

The development of an engineering tool for the prediction of 3-dimensional installation effects on aero-engine jet mixing noise in the presence of a wing has been described. Ray theory has been used to account for the reflection due to a multi-panel approximation to the wing geometry in the presence of an axi-symmetric noise-source distribution. The model includes a new 3-D semi-empirical jet blockage model and empirical jet directivity function for a high-powered coaxial jet operating at realistic flight conditions.

Validation of the prediction method has been shown in the form of

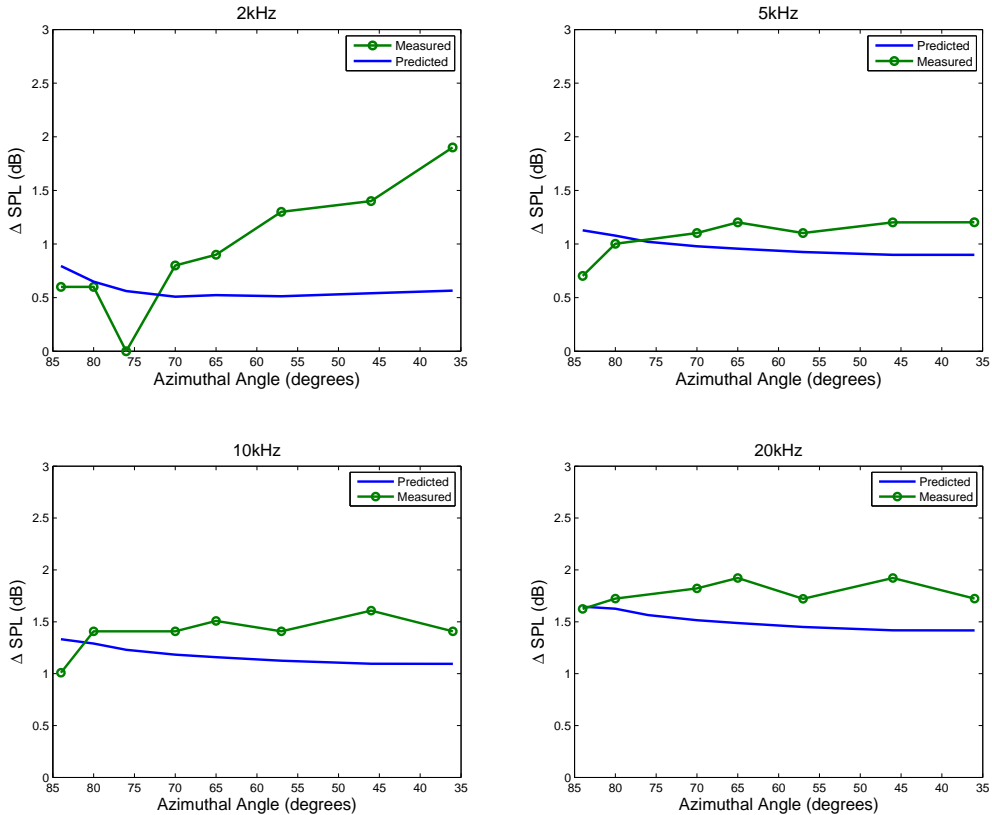


Figure 5.27 – Using a new data set - a comparison of predicted versus measured, ΔSPL is plotted against azimuthal angle for four different model scale frequencies, equivalent full scale frequencies are 111Hz, 277Hz, 555Hz, and 1.1kHz respectively.

comparisons with novel jet-noise installation effects experimental data from static model-scale rig tests. We have demonstrated that by discretising the jet into a number of point sources and applying a point source empirical blockage model we can make fast and accurate predictions over a range of angles.

Further validation of the method has been provided using an additional set of experimental data. In doing this we have shown that by using the relevant scaling parameters of the different aspects of the model, we can use this method to make accurate predictions for different sizes of nozzles, using different wing geometries.

Some limitations of the method have also been exposed, as predictions at lower polar angles are inferior to those around ninety degrees, i.e. in the cone of silence. This is possibly due to the fact that the empirical models are based on far field measurements which do not accurately represent the source, and the proximity of the wing to the jet may in fact alter the source even at high frequencies.

Of course the most significant limitation of the method is that it is semi-empirical and so it is restricted by the extent to which the data fits may be extrapolated. It relies on accurately measured jet source distributions and blockage data. The model cannot be extrapolated to wildly different nozzle geometries or jet conditions. However it has been shown to make fast and accurate predictions for a complex problem.

Chapter 6

Propagation through Jets - Ray Approach

In this chapter a numerical approach to ray propagation is adopted. The background literature on ray theory and sound propagation through jets is reviewed, and a derivation of the ray tracing equations from the convected wave equation is included. The ray tracing equations are then used to develop a 2-D jet propagation method, which is bench marked against an analytical solution for a full wave equation. This 2-D approach is used to develop a fully 3-D jet noise propagation code. The 3-D method is bench marked using an analytical solution of the Lilleý equation. The 3-D method is further enhanced by combining it with realistic CFD jet velocity profiles, and bench marked using the Andante external point source experiments. In this way we are able to develop a fully computational jet blockage model, which is integrated with the jet installation noise prediction method outlined in chapter 5. Finally the integrated ray propagation jet installation method is benchmarked using the Andante data from the jet wing installations effects experiment.

6.1 Background to Ray Theory

The idea of modeling a wave field using rays is one which is borrowed from optics, were a ray “is the idealization of a very narrow beam of light”[47] ; similarly we can think of an acoustic ray as a narrow beam of sound. Much of the acoustic ray theory stems from optics and electromagnetics, as do many of the references.

Ray theory dates back to the 17th century when Snell and Descartes first used three simple rules to determine how rays propagate - straight-line propagation in homogeneous media, a rule for reflection, and the rule for refraction. These simple rules became known as the law of sines, and allowed for the design of lenses and optical instruments. These ideas were generalized to inhomogeneous media and became known as Fermat’s principle (1654), or the principle of least time, which is the idea that the path taken between two points by a ray of light is the path traversed in the least time. It should be noted ray theory is of course only an approximation. Furthermore, in its basic form ray theory it neglects diffraction and interference. It is valid when the frequency is high, i.e. when the wavelength is small compared to significant dimensions of the objects with which the field interacts.

The relationship between waves and rays is well understood today, however, it was not until 1911 when Sommerfeld and Runge [48] showed how the laws of optics could be derived from a homogeneous reduced wave equation or Helmholtz equation.

The application of ray theory provides a particularly useful approximation when considering a moving inhomogenous medium, i.e. when solutions of the full wave equation become difficult. It was Blokhintzev [49] who first derived acoustic geometric approximations for propagation of sound in a moving and inhomogeneous medium, effectively deriving ray theory from a more generalised wave equation.

Significant advances in the field of ray theory were made by J.B Keller in the 1950s, with a series of papers which greatly increased the domain of the application of ray methods [50–53]. Keller extension of ray theory included a generalisation of the concept of rays to include additional rays which follow the surface of smooth objects (creeping rays) and rays which scatter on a sharp edge (edge diffracted rays). This became known as the ‘geometric theory of diffraction’.

In the following section existing work on acoustic propagation through jets, including ray methods, is reviewed.

6.2 Acoustic Propagation Through Jets

Propagation through the jet represents an important part of the jet noise installation effects problem, and a number of different approaches to it have been adopted in the past.

A previous comprehensive and extensive study on this particular problem, outlining a number of approaches, is given by Powles and Tester [28], [45]. In this study Powles and Tester adopt four different approaches to the problem of modeling the scattering by a cylindrical jet of the sound radiated by a single-frequency monopole source. The first approach calculates a numerical Green’s function for the Lilley equation [22]. This method is based on previous work by Tester and Morfey [27], similar approaches have also been published by Wundrow and Khavaran [54]. However, the Powles and Tester work differs from these previous publications in that the solution is generalized to include sources both inside and outside the jet. The second approach is a high-frequency WKB analysis, which is an adaption of Wundrow and Khavarans WKB analysis on single stream jets [54]. Also a low frequency model based on Gehold’s [55] work on jet by jet shielding is given, and a ray model which is a generalization of Morfey and Joseph’s [56] work on shear layer refraction effects. One assumption in all four of

the methods developed was that the jet fluid parameters did not vary in the axial direction, i.e. that the jet was an infinite parallel flow and not spreading.

Significant work on ray tracing through jets in the past includes that of Suzuki and Lele [57], where a ray theory model is used to predict far acoustic pressure from source in transversely sheared mean flow. Other work includes a paper by Freund and Fleischman [58], where a ray theory method to include unsteady flow effects is developed, and used to quantify the significance of the effect of turbulence on propagation through jets. Spalart et al. [59] trace rays through the mean flow of jet, based on LES simulations, and confirm that ray tracing through the mean flow can give good farfield prediction.

In keeping with the high frequency installation effects prediction method developed in chapter 2, it was decided to adopt a ray approach to the problem. Unlike the ray model developed by Powles and Tester [28], where the shear layer of the jet is approximated by a vortex sheet, i.e. a plug jet flow assumption, and the rays are straight lines, we develop a ray code capable of propagating through a steady inhomogeneous moving medium. This will allow for finite thickness shear layer and jet spreading effects.

In this chapter we develop our own ray theory jet propagation method for sources in a steady inhomogeneous moving medium. This method is validated using Powles and Tester [28] numerical calculation of a Green's function for the Lilley equation, for a parallel sheared flow. Yu and Fratello [60] attribute significant differences between measured data and parallel jet models to the effects of the spreading. Using an idealised spreading jet profile Durbin [61], [62] also reported that the spreading jet tends “to eliminate the ‘zone of silence’, or at least replace it by a ‘quieting zone’.

6.3 Rays In a Moving Medium

In this section a mathematical approach to the derivation of the basic ray equations is presented. Consider a homogeneous medium with a uniform mean flow along the the x axis in the positive x direction. The wave equation [63], which governs acoustic propagation, is

$$\frac{1}{c^2} \left(\frac{\partial}{\partial t} + \mathbf{U} \cdot \nabla \right)^2 p = \nabla^2 p. \quad (6.1)$$

For harmonic time dependence this equation reduces to

$$c^2 \nabla^2 p + (i\omega - U \frac{\partial}{\partial x})^2 p = 0. \quad (6.2)$$

This is effectively a convected Helmholtz equation. Given that the Mach number $M = U/c$, we can rewrite the convected Helmholtz equation as,

$$\frac{\partial^2 p}{\partial x^2} + \frac{\partial^2 p}{\partial y^2} + \frac{\partial^2 p}{\partial z^2} + \left(\frac{\omega}{c} \right)^2 p - \frac{2i\omega M}{c} \frac{\partial p}{\partial x} - M^2 \frac{\partial^2 p}{\partial x^2} = 0. \quad (6.3)$$

We seek a time independent solution for the pressure p , in form of the WKB ansatz,

$$p(x, y) = e^{i\omega u(\mathbf{x})} \sum_{n=0}^{\infty} \frac{i^n}{\omega^n} A_n(\mathbf{x}), \quad (6.4)$$

where from herein u is the phase function. The spatial derivatives of p are given by

$$\frac{\partial p}{\partial x_i} = e^{i\omega u} \sum_{n=0}^{\infty} \frac{i^n}{\omega^n} \left(i\omega \frac{\partial u}{\partial x_i} A_n + \frac{\partial A_n}{\partial x_i} \right), \quad (6.5)$$

$$\frac{\partial^2 p}{\partial x_i^2} = e^{i\omega u} \sum_{n=0}^{\infty} \frac{i^n}{\omega^n} \left(-\omega^2 \left(\frac{\partial u}{\partial x_i} \right)^2 A_n + 2i\omega \frac{\partial u}{\partial x_i} \frac{\partial A_n}{\partial x_i} + i\omega A_n \frac{\partial^2 u}{\partial x_i^2} + \frac{\partial^2 A_n}{\partial x_i^2} \right), \quad (6.6)$$

where x_i is the i^{th} component of the vector $\mathbf{x} = (x, y, z)$. Substituting these

into 6.3 gives

$$\begin{aligned} e^{i\omega u} \sum_{n=0}^{\infty} \frac{i^n}{\omega^n} \left\{ -\omega^2 A_n \left[\left(\frac{\partial u}{\partial x} \right)^2 + \left(\frac{\partial u}{\partial y} \right)^2 + \left(\frac{\partial u}{\partial z} \right)^2 \right] + i\omega A_n \left[\frac{\partial^2 u}{\partial x^2} + \frac{\partial^2 u}{\partial y^2} + \frac{\partial^2 u}{\partial z^2} \right] \right. \\ + 2i\omega \left[\frac{\partial u}{\partial x} \frac{\partial A_n}{\partial x} + \frac{\partial u}{\partial y} \frac{\partial A_n}{\partial y} + \frac{\partial u}{\partial z} \frac{\partial A_n}{\partial z} \right] + \frac{\partial^2 A_n}{\partial x^2} + \frac{\partial^2 A_n}{\partial y^2} + \frac{\partial^2 A_n}{\partial z^2} + \left(\frac{\omega}{c} \right)^2 A_n \\ - \frac{2i\omega M}{c} \left(i\omega \frac{\partial u}{\partial x} A_n + \frac{\partial A_n}{\partial x} \right) - M^2 \left[-\omega^2 \left(\frac{\partial u}{\partial x} \right)^2 A_n \right. \\ \left. \left. + i\omega A_n \frac{\partial^2 u}{\partial x^2} + 2i\omega \frac{\partial u}{\partial x} \frac{\partial A_n}{\partial x} + \frac{\partial^2 A_n}{\partial x^2} \right] \right\} = 0. \end{aligned}$$

Given the above power series we can equate the coefficients of powers of ω .

Firstly equating the highest powers ω , which are the ω^2 terms, gives,

$$\left(\frac{\partial u}{\partial x} \right)^2 + \left(\frac{\partial u}{\partial y} \right)^2 + \left(\frac{\partial u}{\partial z} \right)^2 = \frac{1}{c^2} - \frac{2M}{c} \frac{\partial u}{\partial x} + M^2 \left(\frac{\partial u}{\partial x} \right)^2 \quad (6.7)$$

writing the LHS in vector notation, and factorizing the RHS gives

$$(\nabla u)^2 = \frac{1}{c^2} \left(1 - U \frac{\partial u}{\partial x} \right)^2. \quad (6.8)$$

This is the eikonal equation [64] for a moving medium. This is an exact equation which determines the phase function u in the field, i.e. it tells us what the about the wavefronts. This equation will be used to derive the ray equations in the following section. One can also equate coefficients of ω^1 from the power series gives

$$\begin{aligned} A_0 \left[\frac{\partial^2 u}{\partial x^2} + \frac{\partial^2 u}{\partial y^2} + \frac{\partial^2 u}{\partial z^2} \right] + 2 \left[\frac{\partial u}{\partial x} \frac{\partial A_0}{\partial x} + \frac{\partial u}{\partial y} \frac{\partial A_0}{\partial y} + \frac{\partial u}{\partial z} \frac{\partial A_0}{\partial z} \right] \\ - \frac{2M}{c} \frac{\partial A_0}{\partial x} - M^2 A_0 \frac{\partial^2 u}{\partial x^2} + 2M^2 \frac{\partial u}{\partial x} \frac{\partial A_0}{\partial x} = 0 \end{aligned}$$

which gives

$$2M \left[\frac{1}{c} - M \frac{\partial u}{\partial x} \right] \frac{\partial A_0}{\partial x} + 2(\nabla u \cdot \nabla A_0) = A_0 \left[M^2 \frac{\partial^2 u}{\partial x^2} - \nabla^2 u \right], \quad (6.9)$$

this is the first transport equation for a moving medium, an equation which is determines the leading order amplitude term, from the WKB power series expansion. Solutions of the transport equation for an inhomogenous moving medium are difficult. In subsequent section a method for amplitude determination using ray theory is described.

6.4 Ray Equations

When we consider rays in a moving medium, we can think of the local velocity vector of sound traveling along these rays as a superposition of convection and propagation relative to the fluid,

$$\mathbf{v} = \frac{d\mathbf{x}}{dt} = U + \mathbf{n}c. \quad (6.10)$$

We can define a a vector parallel to the wave normal \mathbf{n} , called the ‘wave slowness’ vector \mathbf{s} as

$$\mathbf{s} = \nabla u = \left(\frac{\partial u}{\partial x}, \frac{\partial u}{\partial y}, \frac{\partial u}{\partial z} \right) = (s_x, s_y, s_z). \quad (6.11)$$

Thus we can rewrite the eikonal equation as

$$\mathbf{s}^2 = \left(\frac{\Omega}{c} \right)^2, \quad \text{where} \quad \Omega = 1 - U \frac{\partial u}{\partial x}. \quad (6.12)$$

The normal to the wavefronts \mathbf{n} can be written as,

$$\mathbf{n} = \frac{\nabla u}{|\nabla u|} = \frac{\mathbf{s}}{|\mathbf{s}|} = \frac{\mathbf{s}c}{\Omega}, \quad (6.13)$$

hence

$$\frac{d\mathbf{x}}{dt} = U + \frac{\mathbf{s}c^2}{\Omega}. \quad (6.14)$$

We know that,

$$\begin{aligned}\frac{d\mathbf{s}}{dt} &= \frac{\partial s}{\partial x} \frac{dx}{dt} + \frac{\partial s}{\partial y} \frac{dy}{dt} + \frac{\partial s}{\partial z} \frac{dz}{dt} \\ &= \left(\frac{d\mathbf{x}}{dt} \cdot \nabla \right) \mathbf{s}.\end{aligned}\quad (6.15)$$

Now substituting this into equation 6.14 and expanding,

$$\begin{aligned}\frac{d\mathbf{s}}{dt} &= ((\mathbf{U} + \mathbf{n}c) \cdot \nabla) \mathbf{s} \\ &= (\mathbf{U} \cdot \nabla) \mathbf{s} + c(\mathbf{n} \cdot \nabla) \mathbf{s} \\ &= (\mathbf{U} \cdot \nabla) \mathbf{s} + c\left(\frac{c\mathbf{s}}{\Omega} \cdot \nabla\right) \mathbf{s} \\ &= (\mathbf{U} \cdot \nabla) \mathbf{s} + \frac{c^2}{\Omega} (\mathbf{s} \cdot \nabla) \mathbf{s}.\end{aligned}\quad (6.16)$$

Using the following vector identities

$$\begin{aligned}(\mathbf{s} \cdot \nabla) \mathbf{s} &= -\mathbf{s} \times (\nabla \times \mathbf{s}) + \frac{1}{2} \nabla \mathbf{s}^2 \\ (\nabla \times \mathbf{s}) &= \nabla \times (\nabla u) = 0\end{aligned}\quad (6.17)$$

the final term in equation 6.16 can now be written as

$$(\mathbf{s} \cdot \nabla) \mathbf{s} = \frac{1}{2} \nabla \mathbf{s}^2, \quad (6.18)$$

which can be combined with the eikonal equation 6.8 to give

$$(\mathbf{s} \cdot \nabla) \mathbf{s} = \frac{1}{2} \nabla \left(\frac{\Omega^2}{c^2} \right), \quad (6.19)$$

noting that, $\Omega = 1 - Us_x$ ($\Omega = 1 - \mathbf{U} \cdot \mathbf{s}$ for flow in any direction), we rewrite

$$\begin{aligned}
 (\mathbf{s} \cdot \nabla) \mathbf{s} &= \frac{1}{2} \left[\Omega^2 \nabla \left(\frac{1}{c^2} \right) + \frac{1}{c^2} \nabla (\Omega^2) \right] \\
 &= \frac{1}{2} \left[\frac{2}{c^2} \Omega \nabla \Omega - \frac{2\Omega^2}{c^2} \nabla c \right] \\
 &= \frac{\Omega}{c^2} \nabla \Omega - \frac{\Omega^2}{c^3} \nabla c \\
 &= -\frac{\Omega}{c^2} \nabla (\mathbf{U} \cdot \mathbf{s}) - \frac{\Omega^2}{c^3} \nabla c. \tag{6.20}
 \end{aligned}$$

Substituting this result back into 6.16 gives

$$\frac{d\mathbf{s}}{dt} = (\mathbf{U} \cdot \nabla) \mathbf{s} - \nabla (\mathbf{U} \cdot \mathbf{s}) - \frac{\Omega}{c} \nabla c. \tag{6.21}$$

The following vector identity can be used to give a further reduction,

$$\nabla (\mathbf{U} \cdot \mathbf{s}) = \mathbf{U} \times (\nabla \times \mathbf{s}) + \mathbf{s} \times (\nabla \times \mathbf{U}) + (\mathbf{U} \cdot \nabla) \mathbf{s} + (\mathbf{s} \cdot \nabla) \mathbf{U} \tag{6.22}$$

where the first term is zero because \mathbf{s} is a gradient. Using this identity gives the ray tracing equations

$$\frac{d\mathbf{x}}{dt} = \mathbf{U} + \frac{\mathbf{s}^2 c}{\Omega} \tag{6.23}$$

$$\frac{d\mathbf{s}}{dt} = -\frac{\Omega}{c} \nabla c - \mathbf{s} \times (\nabla \times \mathbf{U}) - (\mathbf{s} \cdot \nabla) \mathbf{U} \tag{6.24}$$

or in cartesian coordinates

$$\begin{aligned}
 \frac{dx_i}{dt} &= U_i + \frac{s_i c^2}{\Omega} \\
 \frac{ds_i}{dt} &= -\frac{\Omega}{c} \frac{\partial c}{\partial x_i} - \sum_{j=1}^3 s_j \frac{\partial}{\partial x_i} U_j. \tag{6.25}
 \end{aligned}$$

These equations determine position along a ray and the direction in which it travels, and these are the equations which we shall proceed to solve.

6.5 Numerical Solution Of Ray Equations

The ray equations 6.25 are a system of coupled non-linear first order ordinary differential equations, thus they are amenable to standard numerical integration techniques. We can solve the equations as an initial value problem using a finite difference method. Initial values are determined using flow parameters at the source location, solving the eikonal equation to determine s_i .

High order Runge-Kutta methods are one of the most popular finite difference methods, due to their stability and consistency. A fourth order Runge-Kutta method can easily be implemented using mathematical software such as Matlab.

6.6 Amplitude Determination

Rather than attempting to solve the transport equation, a simple method of determining the amplitude along a ray path is to use the idea of a ray tube. A ray tube is a small packet of rays, launched at slightly different angles. In two dimensions we can trace the ray tube using two rays, approximating the ray tube area to the distance between the two rays at a fixed time step. Using the law of conservation of energy, we can relate the cross-section, A , of the ray tube to the pressure amplitude

$$p^2 \propto \frac{1}{A}. \quad (6.26)$$

When tracing rays, changes in density of the medium are not considered, as a change in density will not alter the path of an individual ray. However change in density does have an effect on the pressure amplitude. If we know the density at the start and end of the ray tube we are considering, we can use the Blokhintzev invariant [49] to account for this change in pressure

amplitude, it can be written

$$\frac{p^2 |\mathbf{v}_{ray}| A}{(1 - \mathbf{v} \cdot \mathbf{s}) \rho c^3} = \text{constant} \quad (6.27)$$

where,

$$|\mathbf{v}_{ray}| = \mathbf{v} + c\mathbf{n}. \quad (6.28)$$

Thus we can use this expression to account for variations in density, sound speed, and velocity of the medium when determining the pressure amplitude from the change in ray tube area.

6.7 Change in Sound Pressure Level

We can define the jet propagation effects as a ΔSPL to the source in the farfield, such that the change in sound pressure level is defined

$$\Delta\text{SPL} = 10 \log \left(\frac{p_{jet}}{p_{ff}} \right)^2 \quad (6.29)$$

where p_{jet} is the pressure due to the source in the jet, and p_{ff} is the pressure due to the source without the jet i.e. a free field pressure.

Using the Blokhintzev invariant [49] we can write

$$\frac{p(\mathbf{x}_2)^2}{p(\mathbf{x}_1)^2} = \frac{|\mathbf{v}_{ray}(\mathbf{x}_1)| A(\mathbf{x}_1)}{(1 - \mathbf{v}(\mathbf{x}_1) \cdot \mathbf{s}(\mathbf{x}_1)) \rho(\mathbf{x}_1) c(\mathbf{x}_1)^2} \frac{(1 - \mathbf{v}(\mathbf{x}_2) \cdot \mathbf{s}(\mathbf{x}_2)) \rho(\mathbf{x}_2) c(\mathbf{x}_2)^2}{|\mathbf{v}_{ray}(\mathbf{x}_2)| A(\mathbf{x}_2)}. \quad (6.30)$$

Thus assuming, at the source $A_{jet}\mathbf{x}_s = A_{ff}\mathbf{x}_s$, and $p_{jet}\mathbf{x}_s = p_{ff}\mathbf{x}_s$ we can rewrite

$$\Delta\text{SPL} = 10 \log \left(\left(\frac{(1 - \mathbf{v}(\mathbf{x}_s) \cdot \mathbf{s}(\mathbf{x}_s)) \rho(\mathbf{x}_s) c(\mathbf{x}_s)^2}{|\mathbf{v}_{ray}(\mathbf{x}_s)|} \right)_{jet} \frac{|\mathbf{v}_{ray}(\mathbf{x})|}{(1 - \mathbf{v}(\mathbf{x}) \cdot \mathbf{s}(\mathbf{x})) \rho(\mathbf{x}) c(\mathbf{x})^2} \right) \quad (6.31)$$

6.8 Multiple Ray Problem

The idea of a ray tube breaks down when the rays of the ray tube cross, as the theory would suggest that the amplitude tends to infinity. When tracing multiple rays through inhomogeneous moving media it is possible and often very likely to have more than one ray arriving at single location in the farfield. An appropriate method to sum the amplitude and over come the breakdown of the ray solution at caustics is required.

To demonstrate the multiple rays problem consider the following 2-D sound speed profile, based on that of Tester and Morfey [27]. The sound speed profile mimics the radial cross section of a heated jet, defined as

$$c(x, y) = c_\infty + \frac{(c_J - c_\infty)}{2} (1 - \text{erf}(\sqrt{\pi}\chi)) \quad (6.32)$$

where

$$\chi = \frac{r - \text{rad}}{\delta} - 0.168, \quad r = (x^2 + y^2)^{1/2}, \quad (6.33)$$

c_∞ is the sound speed at infinity, c_J is the sound speed at the centre of the jet, i.e. at $r = 0$, δ is the shear layer thickness, and rad is the jet radius. A contour plot of the sound speed profile is given in figure 6.1.

Ignoring the jet flow and simply propagating rays through this sound speed profile we can demonstrate multiple rays.

A point source is placed 2 jet radii above the jet. 60 rays are launched at evenly distributed angles ranging from 0 to 360 degrees, see figure 6.2. The increase in sound speed causes the rays to bend away from the centre of the jet. As can be seen from the ray diagram at some regions in the field we have multiple rays at one location, due to the focusing effect of the sound speed profile. At these caustics, a high-frequency approximation for amplitude calculated along a single ray will break down, as it will not account for multiple rays passing through a single point causing interference with each other.

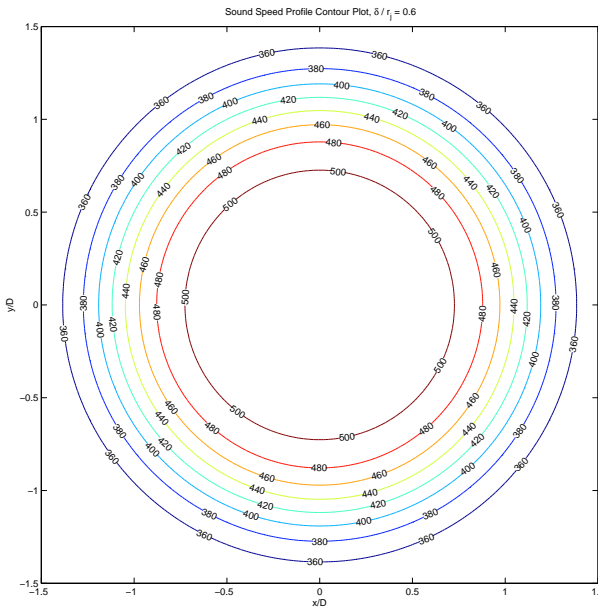


Figure 6.1 – Contour plot of jet sound speed profile.

Even for a simple sound speed or velocity profile determining the caustics can be difficult, thus a different approach to amplitude calculation is adopted.

A crude but effective way of dealing with this problem is to separate the farfield into an evenly distributed number of equally sized regions, or “ray bins”. One can then shoot a much greater number of rays from the source in all directions, and then incoherently sum the pressure amplitude in each ray bin. Which means for a particular ray bin, the last term in equation 6.31 can be approximated to

$$\frac{A_{ff}}{A'_{ff}} \approx \frac{\text{numRays}_{jet}}{\text{numRays}_{ff}} \quad \text{if } \text{numRays} \gg \text{numBins}, \quad (6.34)$$

which gives a useful approximation relating ray density to the pressure amplitude. This is a similar approach as to that adopted by Freund and Fleischman [58], who said -

“We assume that the volume of the caustic-affected region crossing the

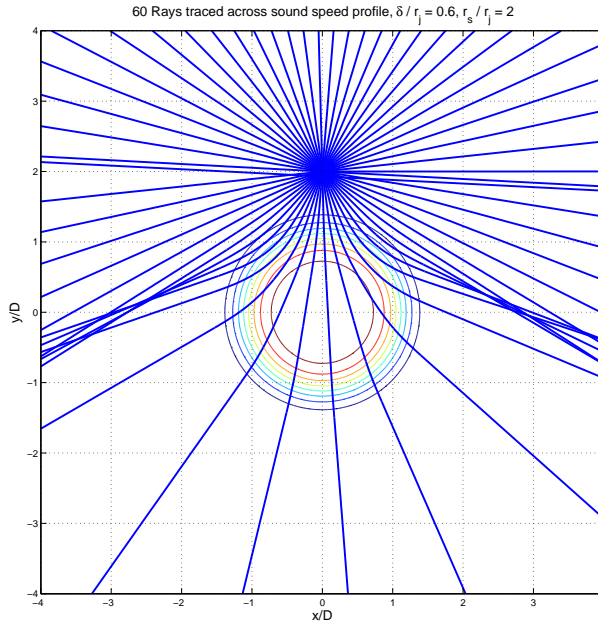


Figure 6.2 – Rays traced through sound speed profile, demonstrating multiple rays turning up in a location.

observation sphere is negligible and the positions of the caustics ever changing, as is indeed observed, and we can therefore neglect them in the statistical average. We also assume that behind the caustics the rays are decorrelated due to the stochastic action of the turbulence so we also neglect interference.”

The large number of rays needed to make this solution converge means this process can be computationally expensive.

6.9 A Two Dimensional Ray Solution

A 2D Matlab ray code - “rayJet2D” was developed, which integrates equations 6.25 and determines a farfield ΔSPL using ray density, as defined in equation 6.31.

In the following sub-sections we benchmark rayJet2D using an ISVR in house Lilley Equation Solution [65], using some idealized jet flow profiles.

We go on to use rayJet2D to assess the significance of assumptions generally made when modeling acoustic propagation through jets, i.e. the jet flow is not spreading, and that the velocity does not decay in the downstream direction.

6.9.1 Validation of 2D Ray Code

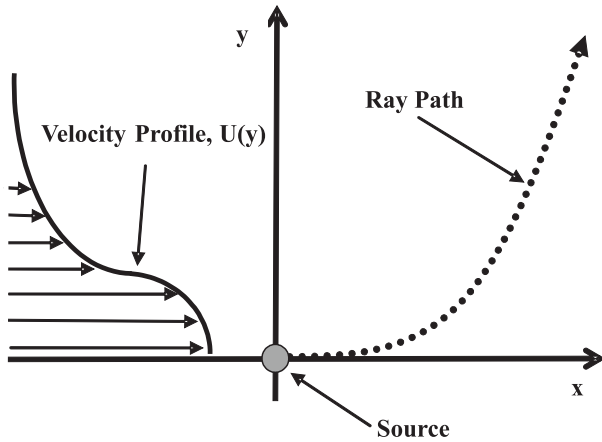


Figure 6.3 – Source in parallel shear flow.

To introduce a simple 2D example, in order to first solve the ray equations, consider a point source on axis in a parallel sheared flow, i.e. a source in a simple jet, see figure 6.3. This represents a sheared flow, with flow gradient only in the y or radial direction, i.e. an infinite 2-D jet.

The ray code is validated using the existing Lilley equation solution [65] for an isothermal parallel infinite jet. The radial velocity profile is defined using an error function, similar to that used by Tester and Morfey [27], where

$$U(y) = U_\infty + \frac{(U_J - U_\infty)}{2} (1 - \text{erf}(\sqrt{\pi}\chi)) \quad (6.35)$$

where

$$\chi = \frac{y - \text{rad}}{\delta} - 0.168, \quad (6.36)$$

U_∞ is the flow velocity at infinity, U_j is the velocity of at the centre of the jet, i.e. at $y = 0$, δ is the shear layer thickness, and rad is the jet radius. A plot of the function for two different shear layers is given in figure 6.4.

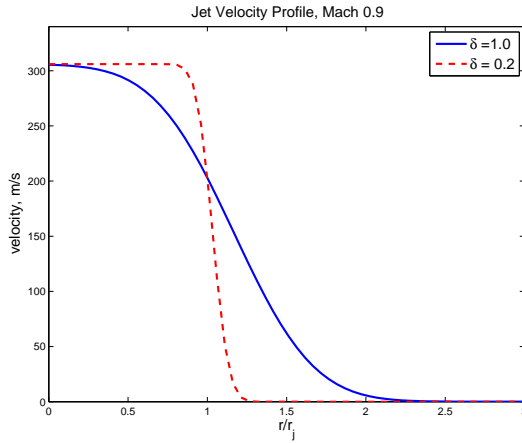


Figure 6.4 – Jet Velocity plotted using the error function profile, for two different shear layer thicknesses, $\delta = 1.0$ and $\delta = 0.2$.

A series of six initial test cases are defined in table 6.1, and the plots of results for equivalent cases can be seen in figure 6.5. A brief discussion of each test case follows.

| Test Case | Mach | δ/r_j | r_s/r_j |
|-----------|------|--------------|-----------|
| (i) | 0.9 | 0.2 | 0 |
| (ii) | 0.9 | 0.2 | 1 |
| (iii) | 0.9 | 0.2 | 2 |
| (iv) | 0.9 | 1 | 0 |
| (v) | 0.9 | 1 | 1 |
| (vi) | 0.9 | 1 | 2 |

Table 6.1 – Set of Test case Jet Conditions, used to validate the 2D ray code

Test case (i) the shear layer is thin, the source is on the jet centre line so solutions above and below the jet are equivalent, and so the solution is simply plotted for a range of polar angles above the jet. The ray solution matches the Lilley Equation solution at most polar angles, up to the cone of silence angle, beyond which point no ray solution exists, however the Lilley

solution falls away very quickly into the zone of silence for this test case.

Test case (ii) the source is in the thin shear layer. The solutions for polar angles above the jet match well up to the cone of silence angle. At the cone of silence angle the ray theory over predicts the level, as the energy that should get into the cone of silence is focused at this point. For the solutions below the jet, the ray theory matches the Lilley solution at all polar angles upstream of the the cone of silence angle. It also has good agreement at the cone of silence angle, as there is very little energy in the region beyond the cone of silence in the full wave equation solution for this test.

Test case (iii) the source is above the jet, just outside the thin shear layer. For solutions above the jet, for polar angles of greater than 60 degrees, both the ray and Lilley solution say that the jet has no effect. For polar angles below 60 degrees both solutions show that energy is being reflected from the jet. The Lilley solution is a coherent and so produces an interference pattern in this region. The ray solution assumes that each ray is fully incoherent, so if exactly two rays turn up in one location will give an increase of approximately 3dB, which is what can be seen in the region beyond 60 degrees. For the polar angles below the jet both solutions agree up to the cone of silence angle.

Test case (iv) is for a source on the centre line of the jet, with a thick shear layer. Solutions for above and below the jet are identical, and both ray theory and the Lilley solution agree up to the cone of silence angle.

Test case (v) is for a source in a thick shear layer just above the center line of the jet. This is similar to test case (ii), but with a thicker shear layer. Again for the solution above the jet the ray theory focuses the noise from the cone of silence region into the cone of silence angle, over predicting at this particular angle. Below the jet the solutions match outside of the cone of silence.

Test case (vi) is for a source outside the shear layer above the jet. Similar

to test case (iii), but with a thicker shear layer. For polar angles above the jet the ray solution gives an increase of 3dB where more than one ray turn up in the same location, and the Lilley solution shows an interference pattern.

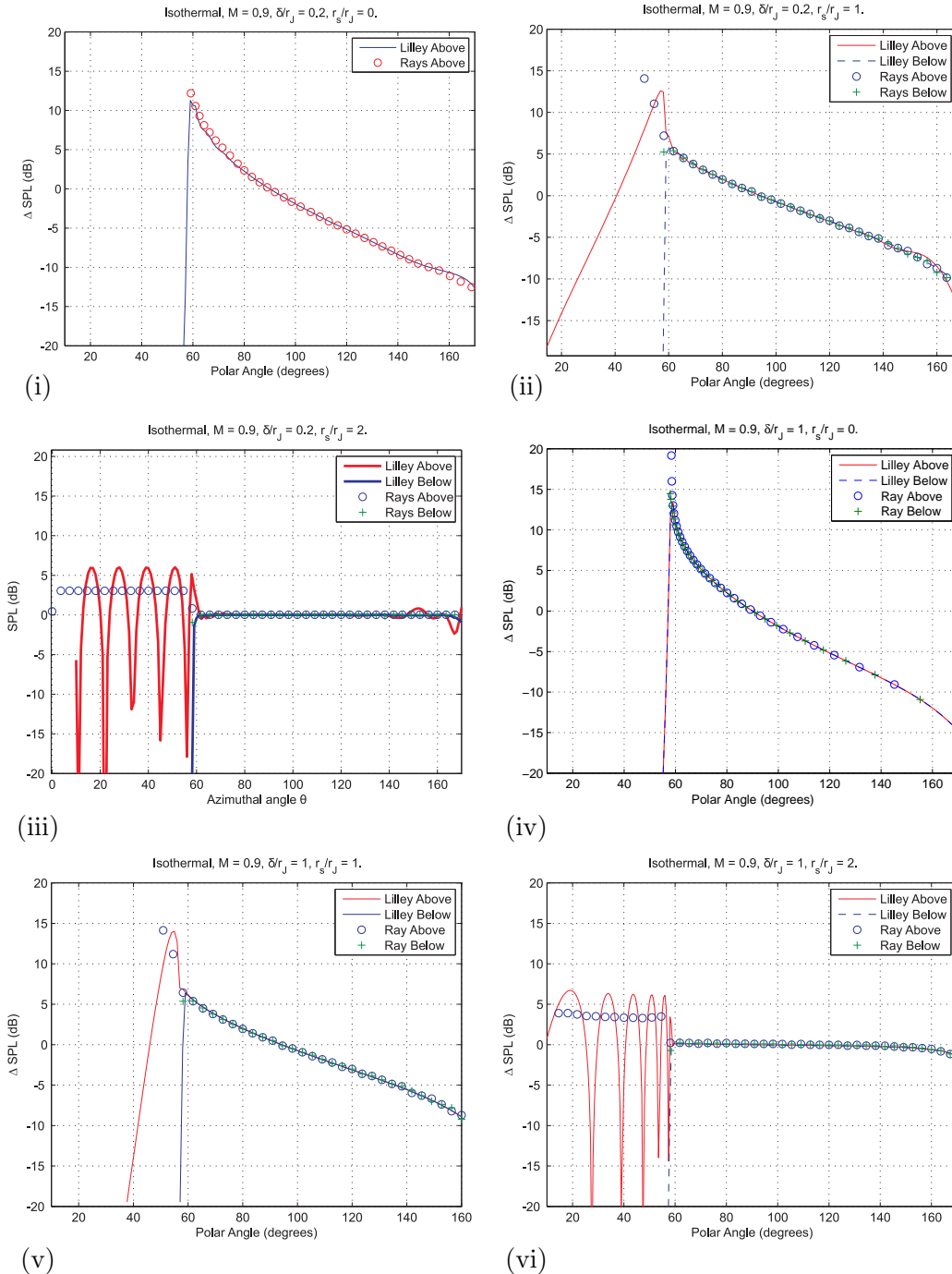


Figure 6.5 – Validation of the 2D ray code using Lilley Solver, for six listed test cases, see table 6.1. Plotted for polar angles above and below the jet, where sources off the radius are above the jet.

6.9.2 A 2D Spreading Jet Velocity Profile

In this sub-section a jet CFD profile is introduced, so that it may be integrated with the ‘rayJet2D’, to provide a more realistic jet profile.

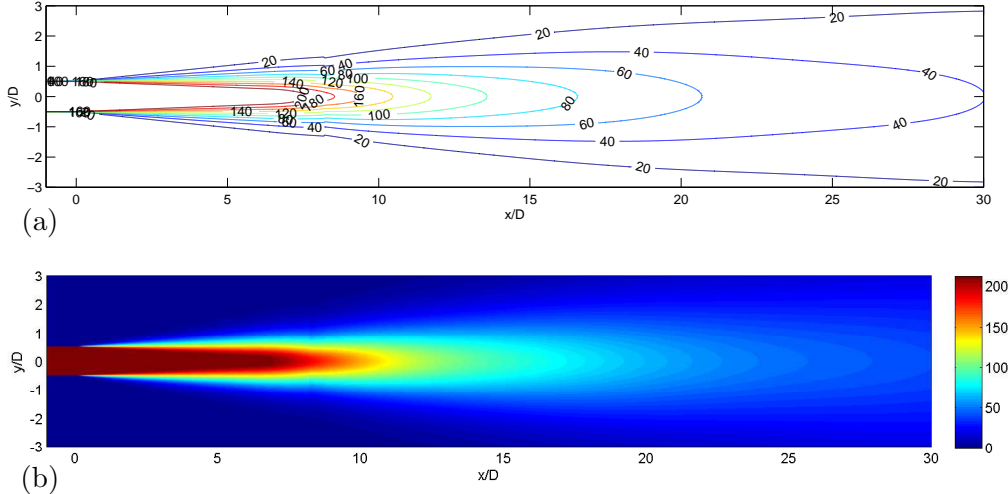


Figure 6.6 – 2D Jet Velocity profile for a single stream, Isothermal $M=0.6$. jet, generated using equation 6.37 a function fitted to a RANS CFD prediction. a) Contour Plot b) Color Map.

The jet velocity profile is based on CFD of an isothermal single stream jet with a Mach number of 0.6 was used. A function fitted to the CFD velocity profile by Azarpeyvand [66] was used to ensure that there were not any discontinuities in the flow, which could cause unwanted effects on ray paths, this also simplified the problem computationally, as it allowed the velocity to be defined in the code, ‘rayJet2D’, using an analytic function.

The jet velocity function is defined as:

$$\begin{aligned}
 U(x, y) = & U_j H(a - x) H\left(\frac{D_j}{2a}(a - x) - y\right) + \\
 & U_j H(a - x) H\left(\frac{D_j}{2a}(x - a) + y\right) \operatorname{sech}^2\left(\frac{D_j}{2a}(x - a) + y\right) / c2 + \\
 & U_j H(x - a) \operatorname{sech}^2(y/c1),
 \end{aligned} \tag{6.37}$$

where H denotes the Heaviside function, and sech denotes the hyperbolic secant function. The empirical coefficients are defined

$$c1 = 0.114x - 0.0111$$

$$c2 = 0.0890x + 0.0012$$

$$a = 7.5D_j,$$

and U_j is jet velocity along the centreline taken directly from the CFD data. These empirical coefficients were optimised such as to minimise the error between the analytic function and CFD data [66].

The velocity component in the radial direction was assumed to be negligible, thus the flow profile was parallel.

Upstream of the nozzle it is assumed that the velocity is equivalent to that at the nozzle exit. This assumption merits further consideration and is discussed in the following sub-section.

6.9.3 Trapped Rays

For the purposes of the ray calculations the radial velocity profile at the nozzle exit is assumed to be constant for all axial positions upstream of the nozzle, no solid body or edge effects of the actual nozzle are considered in the ray calculations. Figure 6.6 shows a contour plot and a colour map of the jet velocity used.

Using ‘rayJet2D’ to trace 60 rays at angles ranging from 0 to 360 degrees from a source position just beyond the end of the potential core, an axial distance of 8 nozzle diameters from the nozzle. The ray paths are plotted against the velocity contour lines of the jet in figure 6.7. As can be seen from the figure a large number of rays launched in the upstream direction become trapped in the infinite jet. Trapped rays are a feature of the infinite jet assumption. In reality a proportion of the noise with travel up the

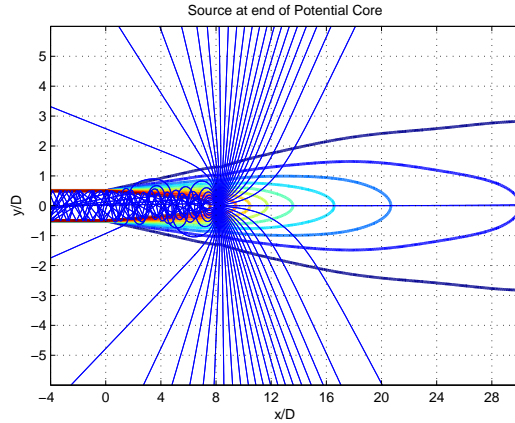


Figure 6.7 – Rays traced from source at end of the potential core. At certain angle rays become trapped by the velocity profile.

jet nozzle. For the purposes of the ray calculation the trapped rays are disregarded, if after a fixed time step they haven't escaped the jet.

6.9.4 An Infinite Parallel Jet versus Realistic Spreading Jet

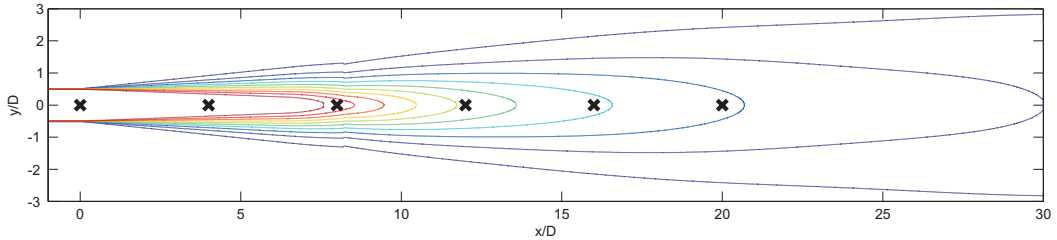


Figure 6.8 – Jet source positions for infinite versus spreading jet investigation, 0D, 4D, 8D, 12D, 16D, and 20D respectively.

One of the main motivation for the development of the this particular ray code, was that the ray tracing approach allows for change in flow in any direction, thus we can propagate sound through a spreading jet. Unlike other jet propagation codes previously developed at the ISVR, i.e. Lilley or WKB [28], the ray code is not based on the assumption that flow parameters vary in only one direction. This means that rays can be propagated through any moving inhomogeneous medium, given that one can determine the flow.

Initially the assumption of a parallel jet is investigated, by comparing results of a infinite parallel versus a more realistic spreading jet.

Using the single isothermal CFD jet flow profile defined in the previous section, sources were positioned on the centerline of the jet at six axial positions as shown in figure 6.8, exact locations of the source positions along the jet axis are 0D, 4D, 8D, 12D, 16D, and 20D respectively. Then for each source position 200 rays were traced from the source launched at a range of angles ranging from 0 to 180 degrees, tracing each ray through the CFD profile. Also at each source location the same number of rays were launched at the same angles through an infinite parallel jet, based on the radial cross section of the CFD flow profile at the location of the source. In this way a comparison can be made between the spreading solution and a solution obtained using a parallel flow assumption.

Figures 6.9 shows comparisons of the Δ SPL predictions for the infinite versus the spreading jet for the six source positions respectively. For the first two source positions there is very little difference between the two predictions, as the source is moved downstream, the solutions become significantly different particularly in the low polar angles, i.e in the around and beyond the cone of silence angle. Note that as the source is moved further downstream, so does the cone of silence, this is because the source effectively sees a slower jet. The spreading jet softens the cone of silence angle, allowing sound much further into what would be the shadow region for a parallel jet. Using a simple analytical jet profile Durbin [61, 62] also previously noted this effect, referring to the zone of silence as a ‘quietening zone’.

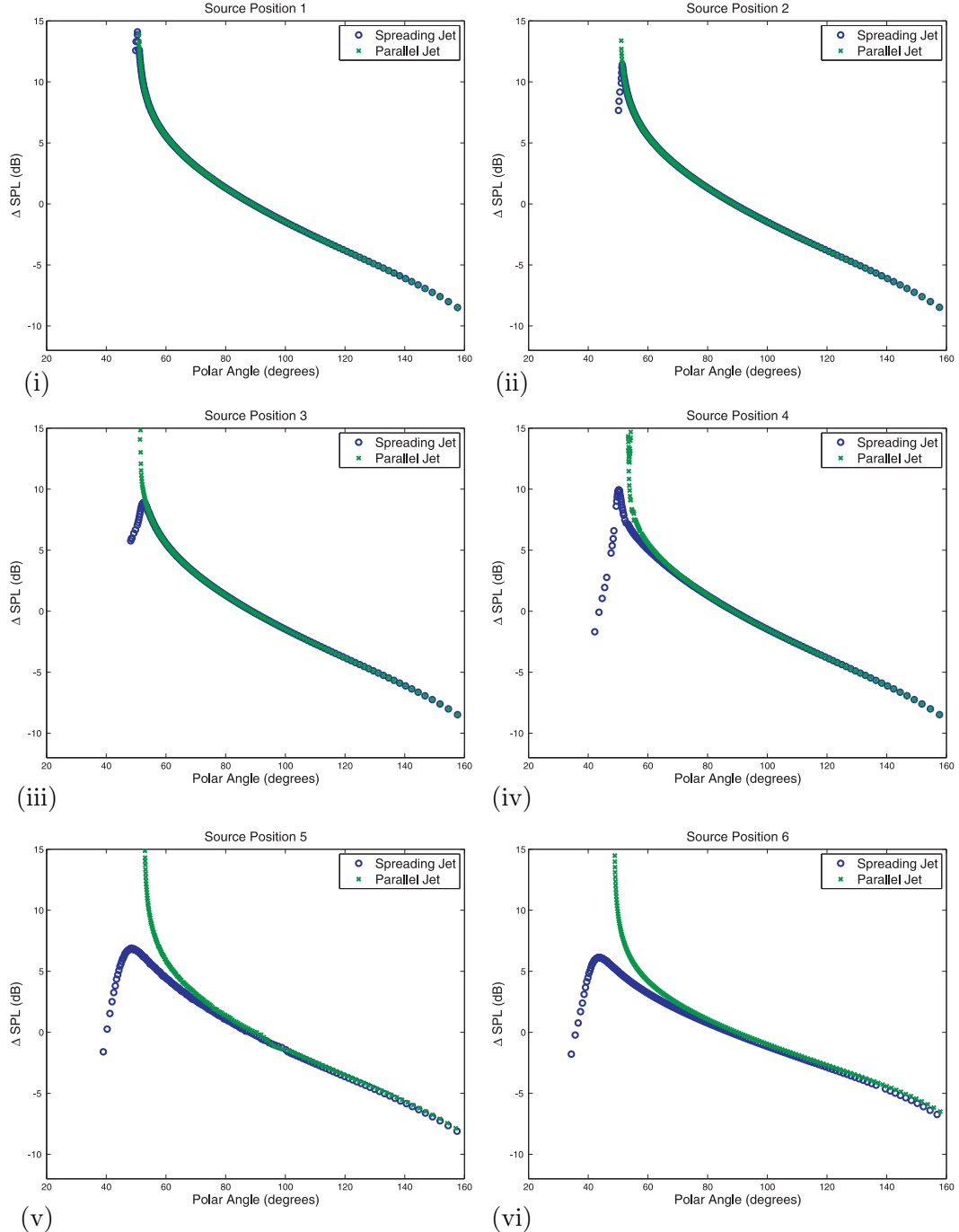


Figure 6.9 – Parallel versus spreading jet plots. In each sub-plot ΔSPL is plotted against polar angle for the six different source positions.

6.10 A Three Dimensional Ray Solution

For the 3D ray tracing solution the number of rays required greatly increases. So a fast Fortran ray tracing code was developed, ‘rayJet3D’. In this section we outline how this method differs from the 2D code. ‘rayJet3D’ is benchmarked against the ISVR Lilley equation solution [28].

6.10.1 Launching Rays in 3D

When launching rays to determine a full farfield solution in 3D, care needs to be taken as it is not as straight forward as launching rays in 2D. Given that amplitude is calculated using ray density, rays launched from a monopole point source should be separated from neighbouring rays by a constant angle. This is to say launch points should be evenly distributed around the sphere, to deliver unbiased ray coverage in 3D. Ray shooting from the vertices of regular polyhedrons is the only way to exactly satisfy this criteria [67, 68].

Since no regular polyhedron has more than twenty vertices, we need to use other geometries to get a high ray resolution.

The geodesic sphere arises by tessellating the faces of regular polyhedron. Figure 6.10 shows how each face of the icosahedron can be recursively sub-divided to effectively tessellate a sphere. Caution should be taken when calculating new vertices like this, as each face shares edges with neighbouring faces. However, it should be noted that the geodesic sphere only approximates uniformity, there are discrepancies in angular separation of the launched rays. Each ray emanating from the original vertices of the icosahedron has only five neighboring rays rather than the usual six, however this becomes insignificant for heavily tessellated spheres[68]. See figure 6.11.

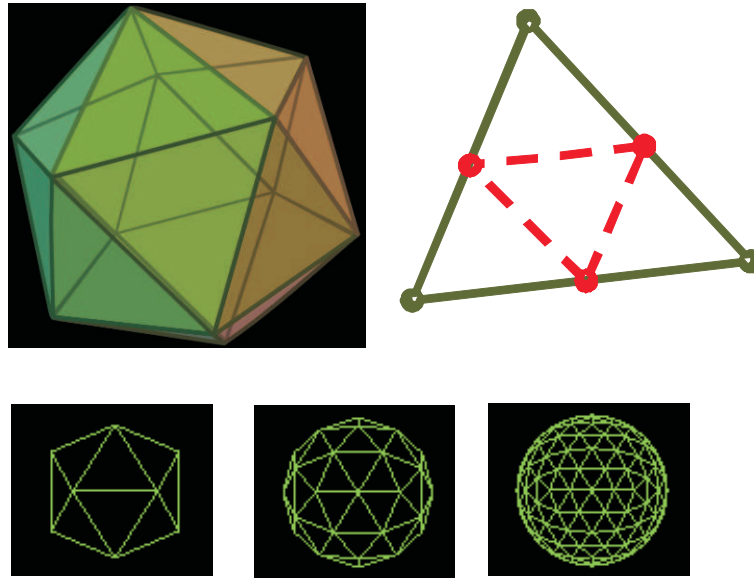


Figure 6.10 – An icosahedron can accurately tessellate a sphere, by recursively sub-dividing each of the faces.

6.10.2 Validation of 3D Ray Code

The 3D ray code, ‘rayJet3D’, is validated using the 3D Lilley solution [28]. A simple isothermal parallel jet velocity profile, where velocity is only in the positive x direction, is defined as

$$U_x(y, z) = U_\infty + \frac{(U_J - U_\infty)}{2} (1 - \text{erf}(\sqrt{\pi}\chi)) \quad (6.38)$$

where

$$\chi = \frac{r - \text{rad}}{\delta} - 0.168, \quad r = (y^2 + z^2)^{1/2}. \quad (6.39)$$

We consider a source outside the jet at two nozzle diameters above a Mach 0.8 jet, with shear layer thickness $\delta/r = 1.0$.

The farfield was discretized into 2562 ray bins, equally dispersed on the surface of a sphere. To get a good resolution on this many ray bins, 2,621,442 rays were launched at geodesic angles, which are the vertices of an icosahedron after 9 sub-divisions of the faces. Using the Fortran 90 code,

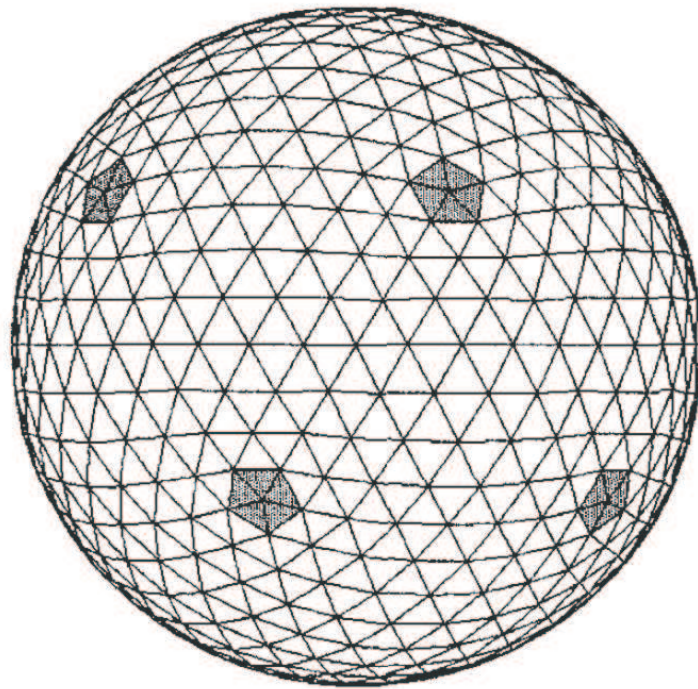


Figure 6.11 – An example of the five neighbour aberrations on a geodesic sphere, generated by sub-dividing an icosahedron 3 times to give geodesic sphere with 642 vertices.

providing a full far field solution takes around 47mins on a single 3GHz Intel Pentium 4 processor. It was found that increasing the number of rays launched did not affect the solution.

Figure 6.12 shows a surface plot of results for a full farfield ray solution. Also included is a surface plot of the same result using the Lilley solution. As can be seen from the plots the shape of solutions are similar, but the ray solution is undefined in the cone of silence region. The other significant difference is that an interference pattern can be seen on the Lilley solution, which is a fully coherent solution. The ray solution assumes that in the farfield the ray will be fully incoherent, and thus gives an effective average of the coherent solution.

Figure 6.13 show a number of slices of the surface plot for single az-

imuthal angles. ΔSPL , as defined in equation 6.31, is plotted against polar angle, for both the ray and Lilley solution. From the plot we can see the ray solution exactly matches the Lilley solution in regions where only one ray can reach any one point. In the regions where multiple rays appear the Lilley solution shows the interference pattern, whereas the ray solution gives the incoherent amplitude sum.

A comparison of the 2-D and 3-D code has also been included in figure 6.13, for azimuthal angles within the X-Z plane, i.e. 0 and 180 degrees, as it can be seen the 2D solution is significantly different. This is because in 3-D it would be equivalent to a line source, with jet flow extending to infinity in the y direction. This highlights the importance of the development of a fully 3D propagation method.

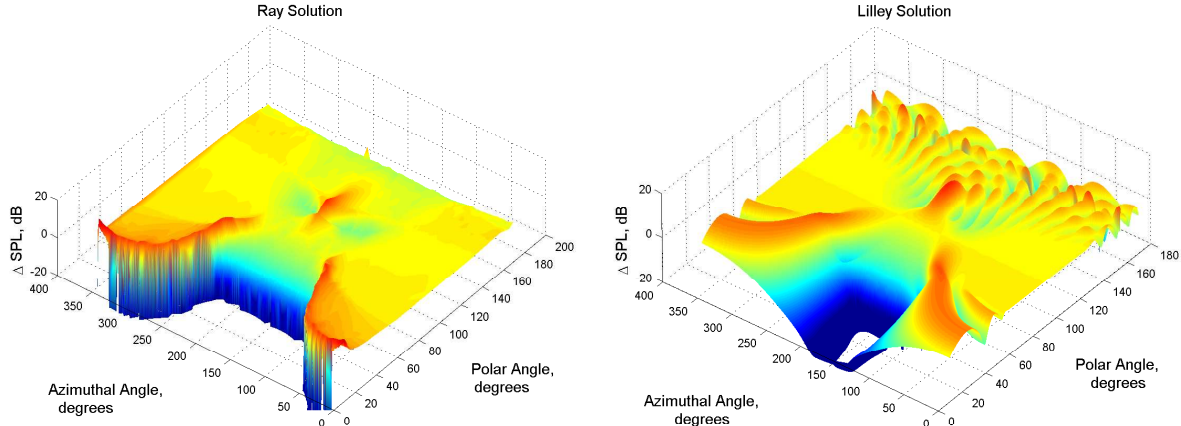


Figure 6.12 – Surface plots using Ray Code and Lilley Solver. Comparison of the two solutions for a source $2D_j$ above an isothermal jet.

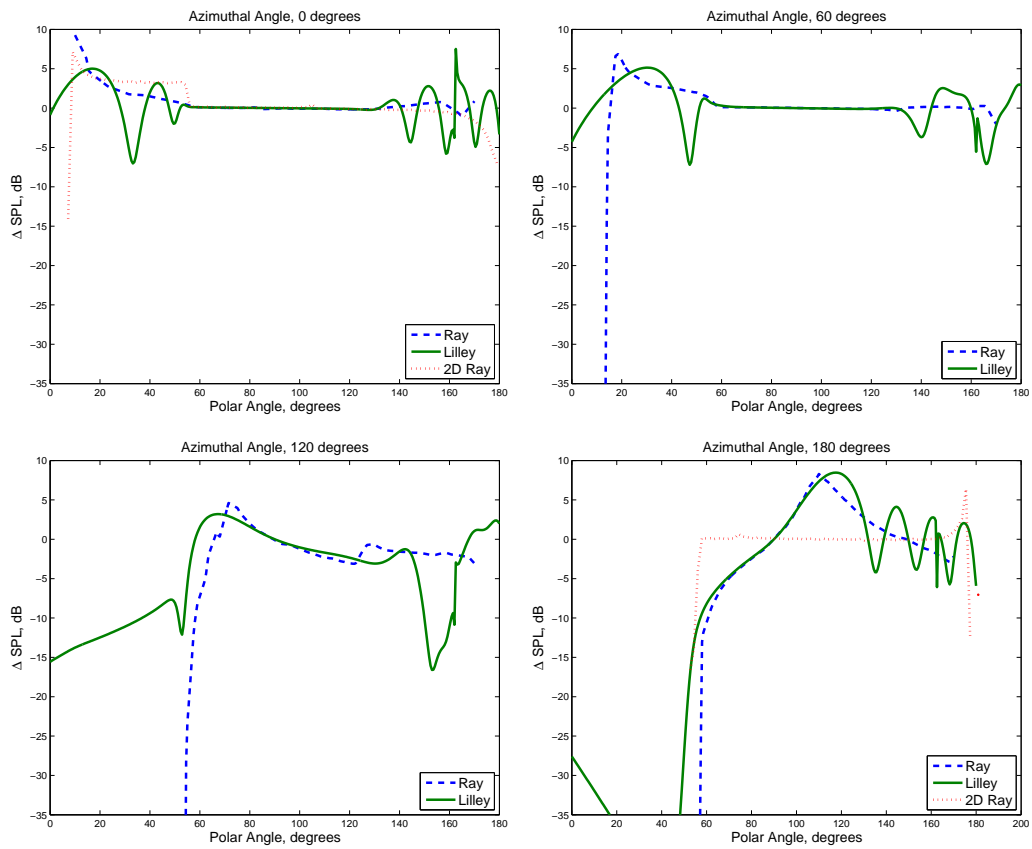


Figure 6.13 – Validation of the 3D ray solver. Delta SPL is plotted against polar angle, for a range of four azimuthal angle. Comparison of the two solutions for a source $2D$ above an isothermal jet.

6.11 Parallel versus Spreading Jet in 3D

The two dimensional ray code was previously used, in section 5.9.2, to investigate the parallel versus spreading jet assumption. Using the two dimensional code has been shown to be inadequate at capturing the fully 3D nature of the problem. The three dimensional ray tracing code, ‘rayJet3D’, makes it possible to now investigate the significance of the infinite parallel flow versus a more realistic spreading jet, looking at both polar and azimuthal variation.

Using the isothermal two dimensional jet profile outlined in section 5.9.2, we can define a isothermal three dimensional axi-symmetric jet velocity profile, that is

$$\begin{aligned} U(x, y, z) = & U_{axis} H(a - x) H\left(\frac{D_j}{2a}(a - x) - r\right) + \\ & U_{axis} H(a - x) H\left(\frac{D_j}{2a}(x - a) + r\right) \operatorname{sech}^2\left(\frac{D_j}{2a}(x - a) + r\right) / c2 + \\ & U_{axis} H(x - a) \operatorname{sech}^2(r/c1), \quad \text{where } r = \sqrt{y^2 + z^2}, \end{aligned} \quad (6.40)$$

the empirical coefficents, $c1, c2, a$, and jet velocity along the centreline, U_j , are the same as those defined in section 5.9.2.

Using this 3-D axi-symmetric isothermal jet velocity profile the parallel versus spreading jet numerical experiment is repeated in 3-D. A source is positioned at one nozzle diameter above the jet at position three nozzle diameters from the jet nozzle. The parallel jet profile was created using equation 6.40 with $x = 3D_j$, such that the velocity profile is independent of axial position.

The results can be seen in figure 6.14. The figure has six sub plots each one represents a single polar angle and each sub plot has the ΔSPL plotted against azimuthal angle, for both the spreading and parallel jet.

At 110 degrees polar angle it can be seen from the plot that the parallel prediction makes only a very slight difference to the level in the blockage

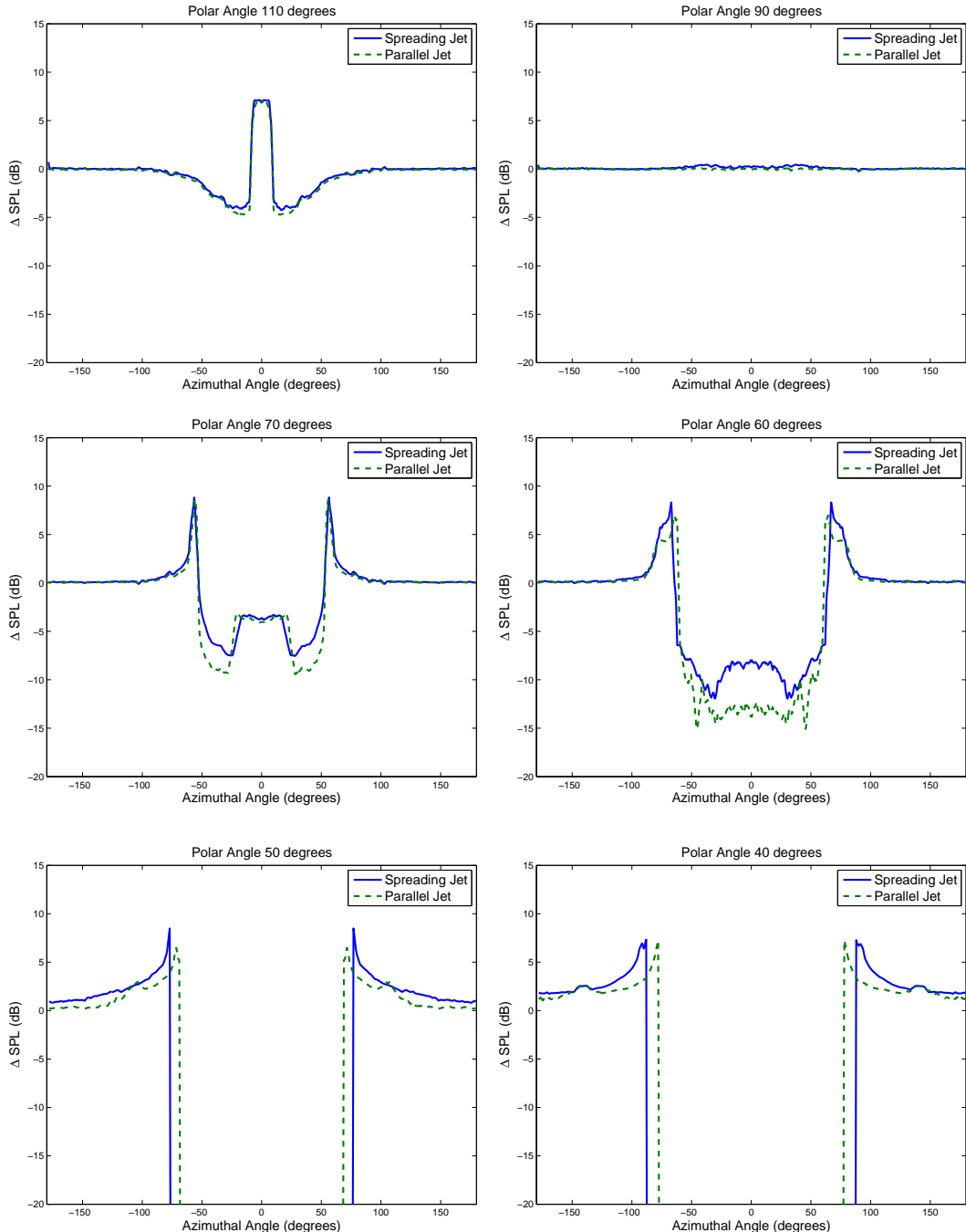


Figure 6.14 – Comparison of Δ SPL of a parallel versus spreading Mach 0.8 jet, for a point source one nozzle diameter above the jet, 3 diameters downstream from the nozzle.

region. At 90 degrees polar angle there is almost no difference at all, as one would expect, at this polar angle the approximation is perfect. Moving downstream to polar angles of 60 and 70 degrees, the difference become more distinct.

The polar plot at 70 degrees particularly highlights the significance of the azimuthal variation which can be seen using the 3-D ray code. Simply looking at the 0 degree azimuthal angle, where the rays will have passed through the potential core, there is almost no difference between solutions. Off centre between 30 and 50 degree azimuthal angles, there is a significant difference in levels, which is a result of the rays having passed through the different shear layers.

In the polar plot at 60 degrees the blockage region for the parallel jet is deeper, as the rays will pass through a faster jet, the differences becomes more significant at lower polar angles.

At the lowest polar angles, 40 and 50 degrees, the cone of silence is observed to be wider for the spreading jet as one would expect.

6.12 Blockage Model Assumptions

When developing the semi-empirical blockage model in chapter 5 section 5.4, it was assumed that radial variation of the source location could be accounted for using a simple scaling factor, and it was assumed that axial variation of the source location was insignificant. In the following two subsections these assumptions will be investigated using ‘rayJet3D’.

6.12.1 Radial variation of the source location

Using the Mach 0.6 isothermal jet velocity profile defined in equation 6.40 with ‘rayJet3D’, three sources were positioned at a range of radial source locations, at 2, 3 and 4.5 nozzle diameters, at a fixed axial position of 3

nozzle diameters downstream of the nozzle. This range of radial positions was chosen to represent the range of jet noise image source positions one would expect to see on a typical under wing installation, e.g. the Andante installation experiment outlined in chapter 3.

Using the data from source position two, which is in a similar position as to the loud speaker in the Andante test, the scaling factor, α , from chapter 4 section 4.4.1 was applied to see how the data would scale to source positions 1 and 3.

Figure 6.15 contains six sub-plots, each plotting Δ SPL against azimuthal angle. The plots on the left compares how data from source position 2 is scaled to 1, while the right compares how data from source position 2 is scaled to 3.

Upstream at polar angle 110 degrees the simple scaling does not work particularly well as it does not account for a change in levels but simple stretches or compresses the shape of the blockage and focus regions. At polar angle of 80 degrees the scaling works almost perfectly. Downstream at a polar angle of 60 degrees the scaling accurately captures the variation in width of the blockage region, however outside of the blockage region the change in the width of the focus region is not accounted for.

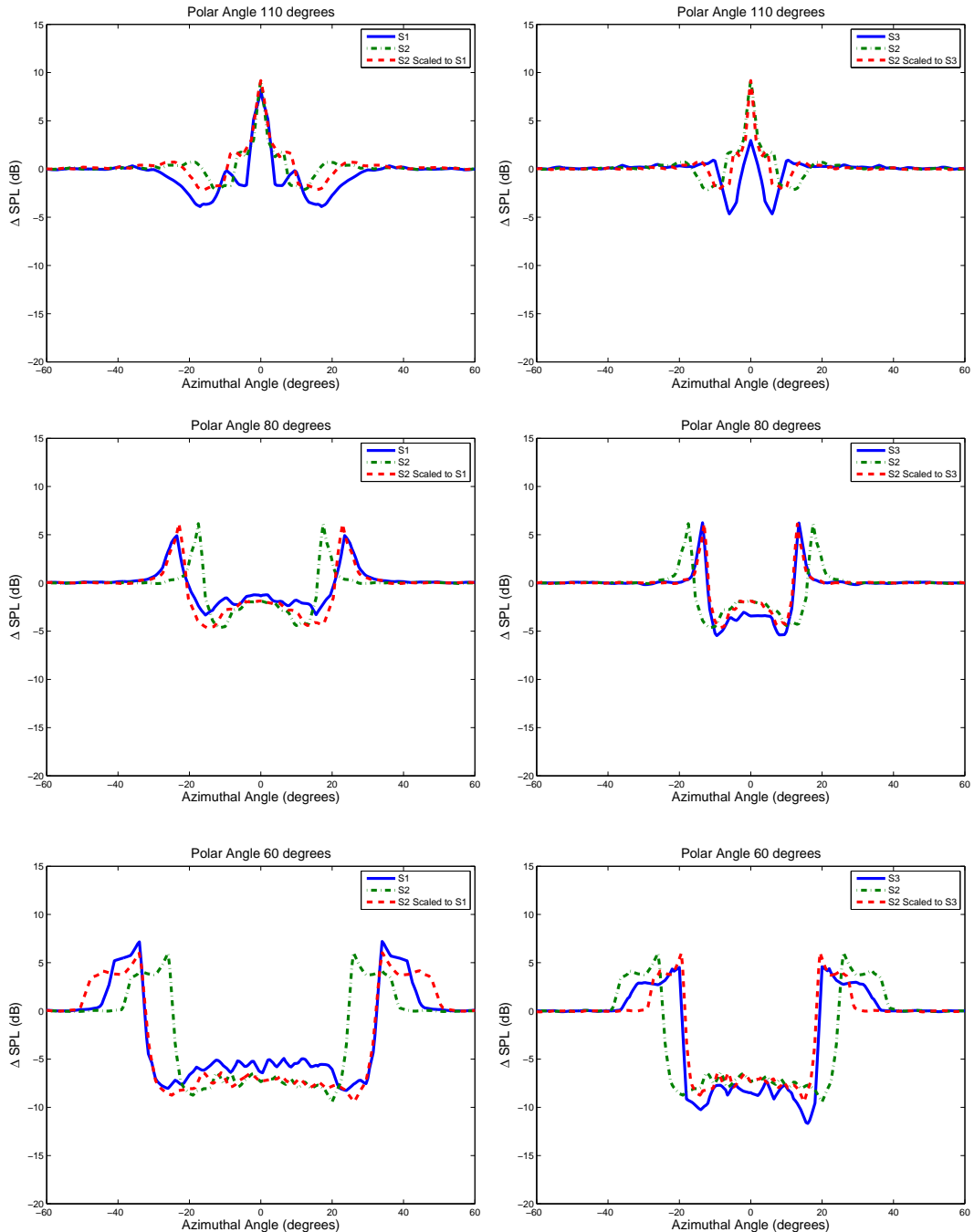


Figure 6.15 – Test of data scaling factor for sources at fixed axial location with source 1, 2, and 3 at radial distances of 2, 3 and 4 nozzle diameters from the jet axis. ΔSPL is plotted against azimuthal angle for a range of 3 polar angles.

6.12.2 Axial variation of the source location

When the semi-empirical blockage model was developed in chapter 5, one of the assumptions that was made was that axially varying the source location above the jet would not make a significant difference to the blockage levels. This assumption was made due the fact that the data restricted us to one source position. Having developed the 3-D ray code this assumption can now be investigated by conducting a simple numerical experiment.

Using the Mach 0.6 isothermal jet velocity profile defined in equation 6.40 with the 3-D ray code, a source was placed above the jet at a range of source locations one nozzle diameter above the jet. The source was placed at axial locations of one, two, three and four nozzle diameters above the jet. The source locations represent the range of axial positions one would expect to see jet noise sources being reflected from a wing.

Figure 6.16 contains six sub-plots, each representing a single polar angle. Each sub-figure plots ΔSPL against azimuthal angle for each of the four source positions.

Upstream at polar angle 110 degrees there is a marked difference in the four solutions, the further downstream the source the greater the focusing effect at zero degree azimuthal angle. At the 90 degree polar angle propagation through the isothermal jet has no effect as expected, so all source locations look the same. The 1D source solution has not converged as well as the other solutions due to the fact that the shear layer is much thinner at this source location, which could be corrected for by decreasing the time step size in the ray tracing code. Downstream at polar angles of 60 and 70 degrees there is a slight difference in the width of the blockage regions, which becomes more prominent at lower polar angles, this is a result of the fact that sources which are further downstream are closer to the jet. Outside the blockage region the increases for the downstream sources are much higher than those of the upstream source, up to 3 or 4 dB, as the energy is being

focused to narrower range of azimuthal angles, which is a result of the fact that the source is closer to jet, due to the jet spreading.

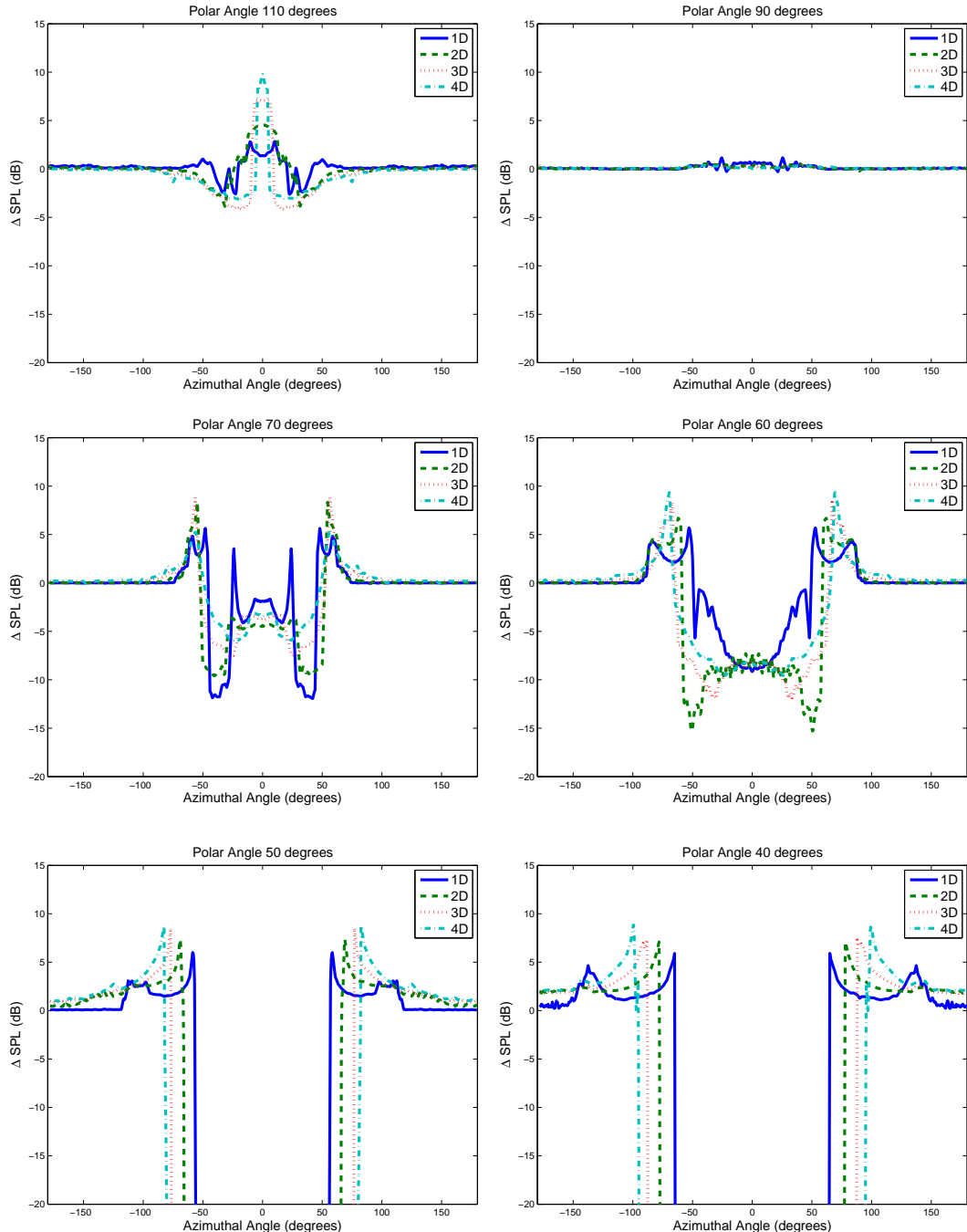


Figure 6.16 – Comparison of Δ SPL of spreading jet, for a point source at $1D_j$ above the jet for a range of axial position(1,2,3 and $4D_j$).

6.13 Experimental Validation of ‘rayJet3D’

To provide further validation of the ‘rayJet3D’, the code is validated using the ANDANTE point source jet blockage experiment data. To provide the ray code with an accurate jet velocity profile the code is coupled with mean flow data from a RANS CFD jet flow simulation.

Initially the jet profiles are outlined in sub-section 5.13.1, and results using ‘rayJet3D’ with coupled with the realistic CFD jet profiles are compared with experimental data in the following sub-section.

6.13.1 Jet Profiles

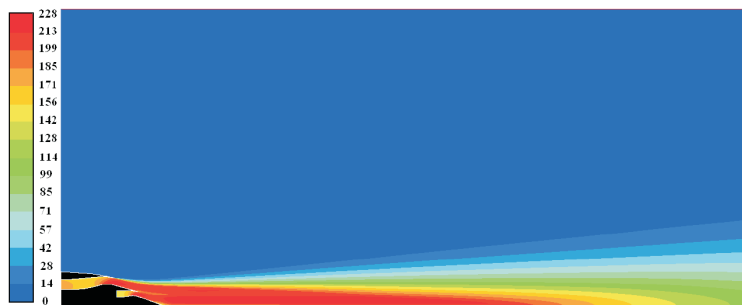


Figure 6.17 – CFD for isothermal short cowl nozzle with VR 1.0.

The jet velocity profiles were generated using the commercial CFD package, FLUENT. A schematic of the nozzle used in the simulations is included in appendix A figure A.3. The nozzle used was Short-cowl nozzle, similar to that used in the ANDANTE experiments in chapter 3, with an equivalent by-pass ratio.

For jet conditions ‘Isothermal’ and ‘Intermediate’, see table 4.2, both with a velocity ratio close to unity, the following function provided a fit to CFD data for axial positions downstream of the tip of the nozzle bullet. The

function fitted to the data by Azarpeyvand [66] is defined

$$\begin{aligned}
 U(x, y, z) = & U_{axis}H(a - x)H\left(\frac{D_s}{2a}(a - 1.5x) - r\right) + \\
 & U_{axis}H(a - x)H\left(r - \frac{D_s}{2a}(a - 1.5x)\right)\operatorname{sech}^2\left(r - \frac{D_s}{2a}(a - 1.5x)\right)/c2) + \\
 & U_{axis}H(x - a)H\left(r - \frac{D_s}{2a}(a - 1.5x)\right)\operatorname{sech}^2\left(r/c1\right), \\
 \text{where } r = & \sqrt{y^2 + z^2},
 \end{aligned} \tag{6.41}$$

where the function is optimized to minimise the difference with the CFD data by varying parameters $a, c1, c2$. The following values were found to give a good fit to the data;

$$\begin{aligned}
 a &= 7.0D_s, \\
 c1 &= -0.0101 + 0.0980x, \\
 c1 &= 0.00123 + 0.8907x.
 \end{aligned}$$

Note that jet condition ‘Intermediate’, has a temperature ratio 0.4. Due to lack of readily available CFD data using this nozzle for a hot jet, it is assumed that the temperature profile will match the velocity profile, for this test condition only. This means the temperature profile used is wider than it should be, thus predictions for this test case may be less accurate as a result.

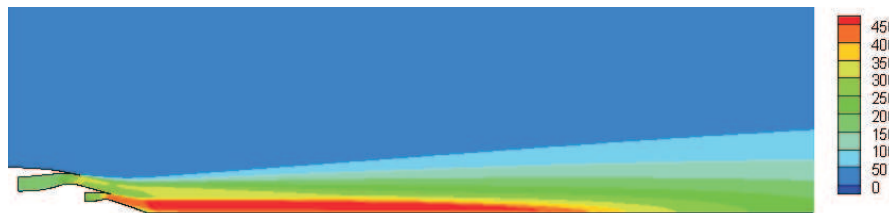


Figure 6.18 – Velocity profile from CFD for sideline jet condition with short cowl nozzle, VR = 0.7.

For jet condition ‘Sideline’ CFD data for a heated coaxial jet with the

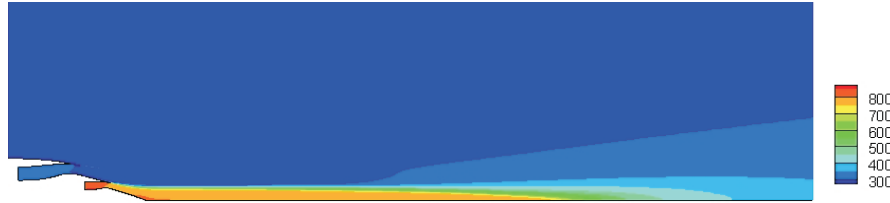


Figure 6.19 – Temperature profile from CFD for sideline jet condition with short cowl nozzle, TR=4.0.

same velocity and temperature ratio, using the nozzle in appendix A, was generated. The CFD data downstream from the bullet was projected on a course mesh. A schematic of the mesh used can be seen in appendix A, refining this mesh was found to have no effect on ray tracing results.

The CFD data projected onto this course mesh was used in combination with a bilinear interpolation routine [69] to provide the 3-D ray code with a smooth velocity and sound speed profile. See figures 6.18, 6.19 for velocity and temperature profiles respectively.

6.13.2 Results

Results using the three profiles can be seen in the following three figures 6.20, 6.21, 6.22. Ray predictions and experimental data are plotted for a range of polar angles. Δ SPL is plotted against azimuthal angle in each sub-figure.

There is a considerable scatter on the experimental data, some of which may be a result of reflections from the structure supporting the traversing microphone array. The results however capture the shape of the distribution.

The results for ‘Isothermal’ jet condition in figure 6.20 show the ray tracing model predicts the experimental results with reasonable accuracy. The width and depth of the blockage region is captured accurately, particularly at polar angles of 50, 60 and 70 degrees.

In figure 6.21 results for ‘Intermediate’ jet condition are shown. The cone of silence angle can be seen to increase, i.e. move further up stream. The

ray method does not provide a solution within the blockage region for polar angles of 50 and 60 degrees. Given that only an approximate sound speed profile was used for this jet condition, the width of the blockage region is not captured as accurately, however the results reasonably capture the redistribution of energy.

Finally results using the velocity and sound speed profiles projected onto a mesh can be seen in figure 6.22, for ‘Sideline’ jet condition. The core of the jet is hotter than the ‘Intermediate’ jet, again causing the cone of silence angle to increase, and move further upstream. The results capture the shape of the energy distribution well. Using the more accurate sound and velocity profiles can be seen to accurately capture the width of the blockage region more accurately.

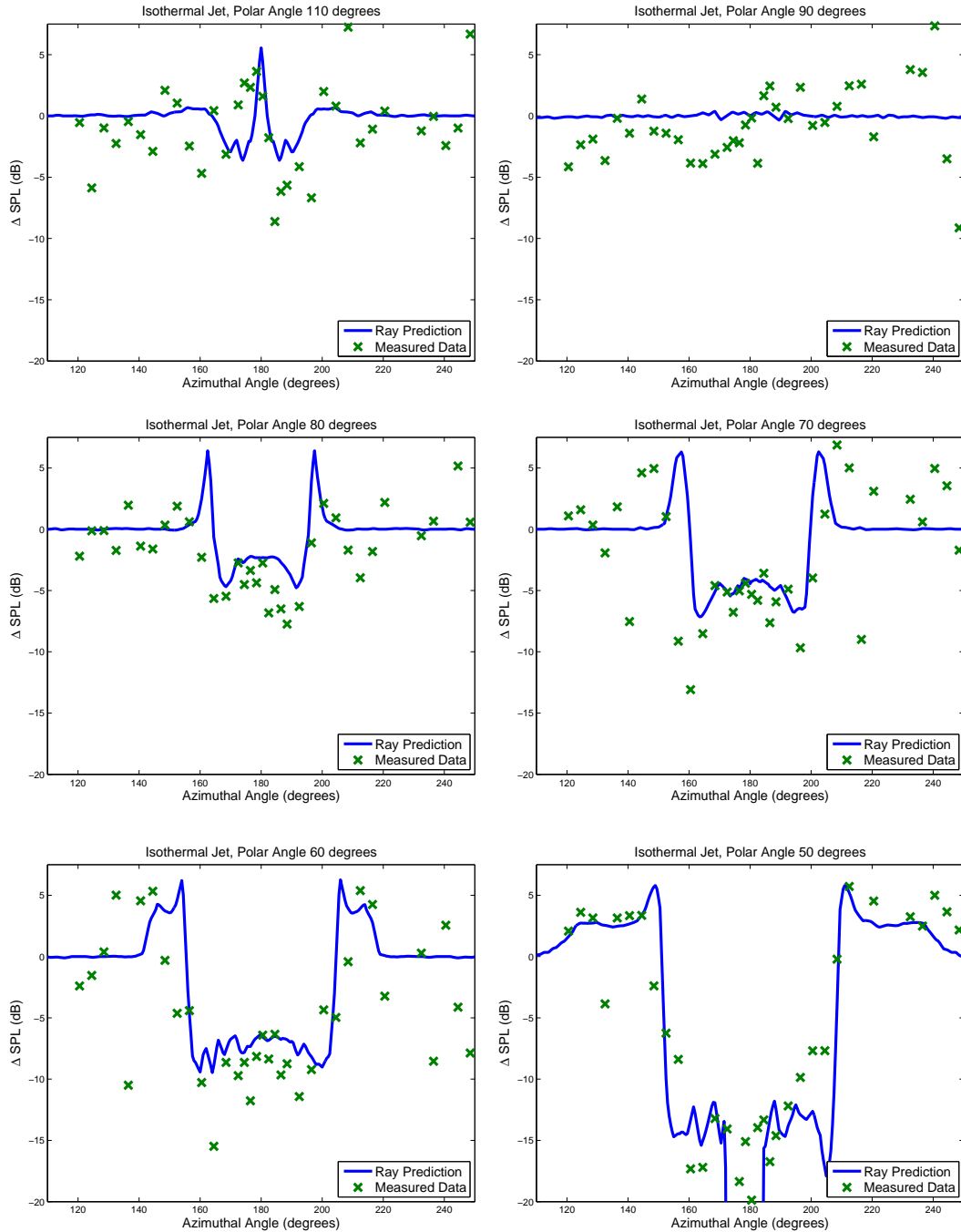


Figure 6.20 – Comparison of 'rayJet3D' with data from ANDANTE experiment 1, for 'Isothermal' Jet.

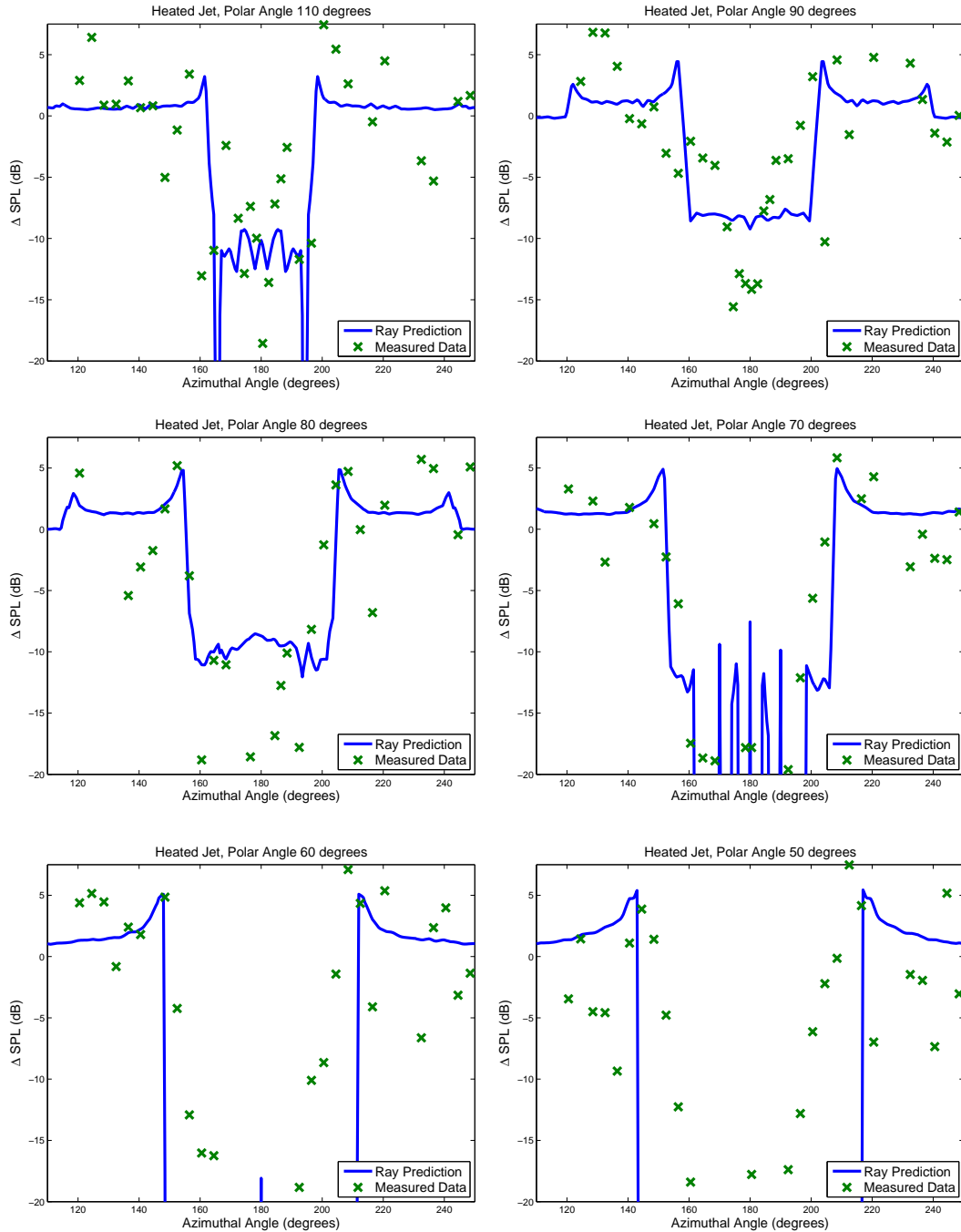


Figure 6.21 – Comparison of 'rayJet3D' with data from ANDANTE experiment 1, for 'Intermediate' Jet.

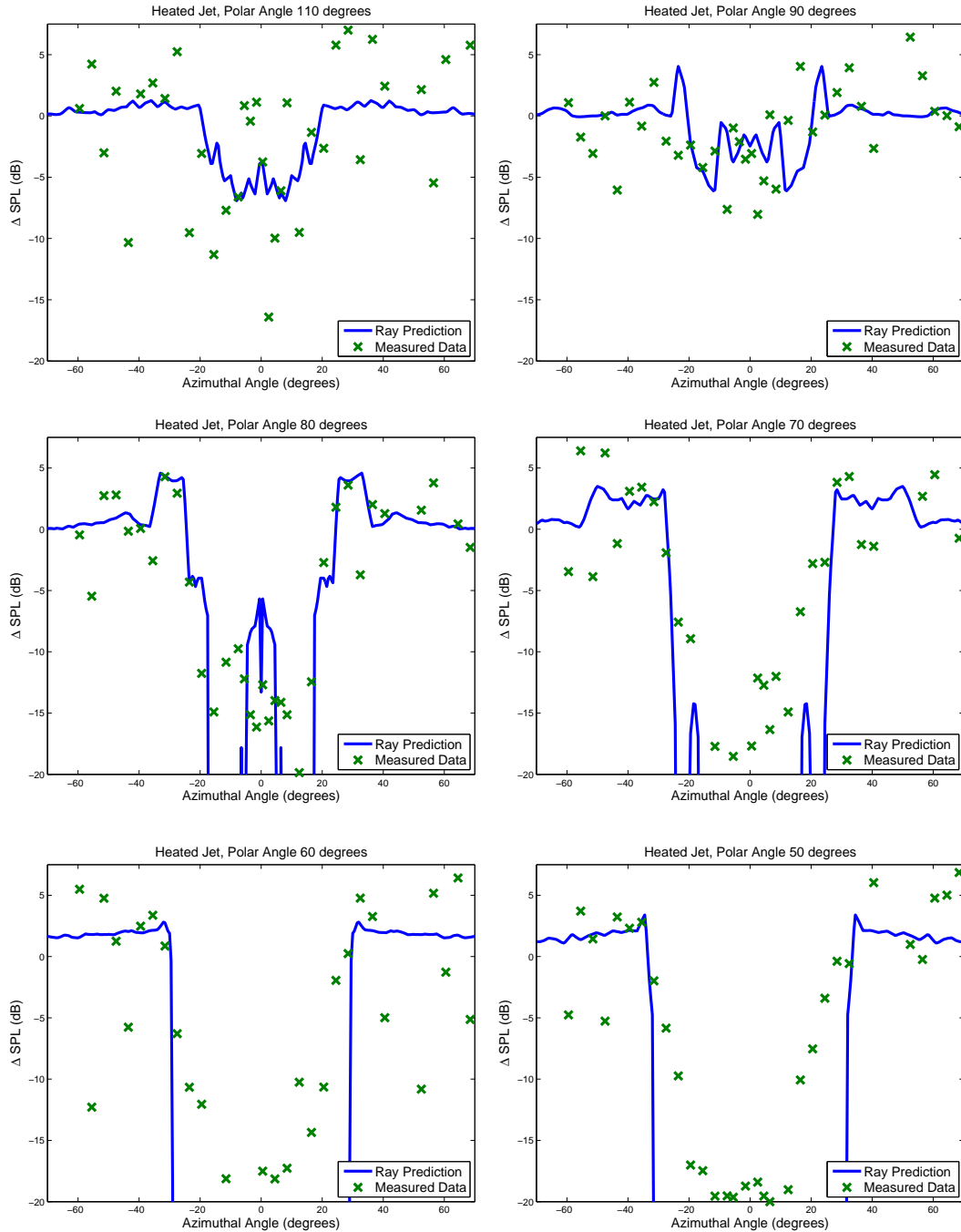


Figure 6.22 – Comparison of 'rayJet3D' with data from ANDANTE experiment 1, for 'Sideline' Jet.

6.14 Jet Reflection Prediction

‘rayJet3D’ has been combined with the installation prediction method from chapter 5. ‘rayJet3D’ is used to replace the semi-empirical blockage model from the jet wing reflection prediction method.

In order to reduce computation time one major assumption is made. It is assumed that the image source is that which would be seen from an observer positioned at 90 degrees polar angle, zero degrees azimuthal angle. Of course the image source, i.e. the portion of the jet reflected from the wing, is dependent on the observer position. However, as the jet source is close to wing, this should be a good approximation to image source for azimuthal angles between ± 40 degrees, and polar angles of 110 to 50 degrees. The number of sources approximating the jet was also reduced to six sources per ring and twenty ring sources to improve computation time.

The new jet wing reflection method is validated using data from the jet wing experiment described in chapter 4. Predictions are compared with data for jet conditions ‘Intermediate’ and ‘Sideline’. No experimental data was measured for ‘Isothermal’ jet condition in the jet wing experiment.

Figures 6.23 and 6.24 compare prediction with experimental data for jet condition ‘Intermediate’ and ‘Sideline’ respectively. ΔSPL is plotted against azimuthal angle, each sub-plot represents a single polar angle. Also included in each figure is a prediction using the semi-empirical blockage model.

The predictions are generally within a few decibels of the measured data. The prediction method works particularly well at 90 degree polar angle for both ‘Intermediate’ and ‘Sideline’ jet conditions. For ‘Intermediate’ jet condition the blockage region is predicted as wider than the data, this is likely to be a result of the approximate temperature profile used for the prediction of this jet condition. The width of the blockage region is captured more accurately predicting for the ‘Sideline’ jet condition, were a more accurate jet profile is used.

Beyond the cone of silence angle the predictions using the ray method become less accurate. This is to be expected as it is a feature of the high frequency approximation. This is more evident in the ‘Sideline’ jet condition predictions, were the cone of silence angle is further up stream, thus results are effected up to a larger polar angles.

There is a significant difference between the predicted and measured data at high positive azimuthal angles. This is due to the assumption that the image source is independent of observer position, and it is apparent on one side due to the dihedral angle of the wing. The number of sources per ring used in the computation was insufficient, causing the spikes in the solution. This could be easily corrected by increasing the number of sources per ring, however this would have required further computational power, i.e. a parallel processor, given that current computations took a number of days on single machine.

These results, however, demonstrate the principles of applicability of this technique as useful method for determining acoustic propagation through a realistic jet. Although computationally expensive the method has proven to give accurate results outside of the cone of silence.

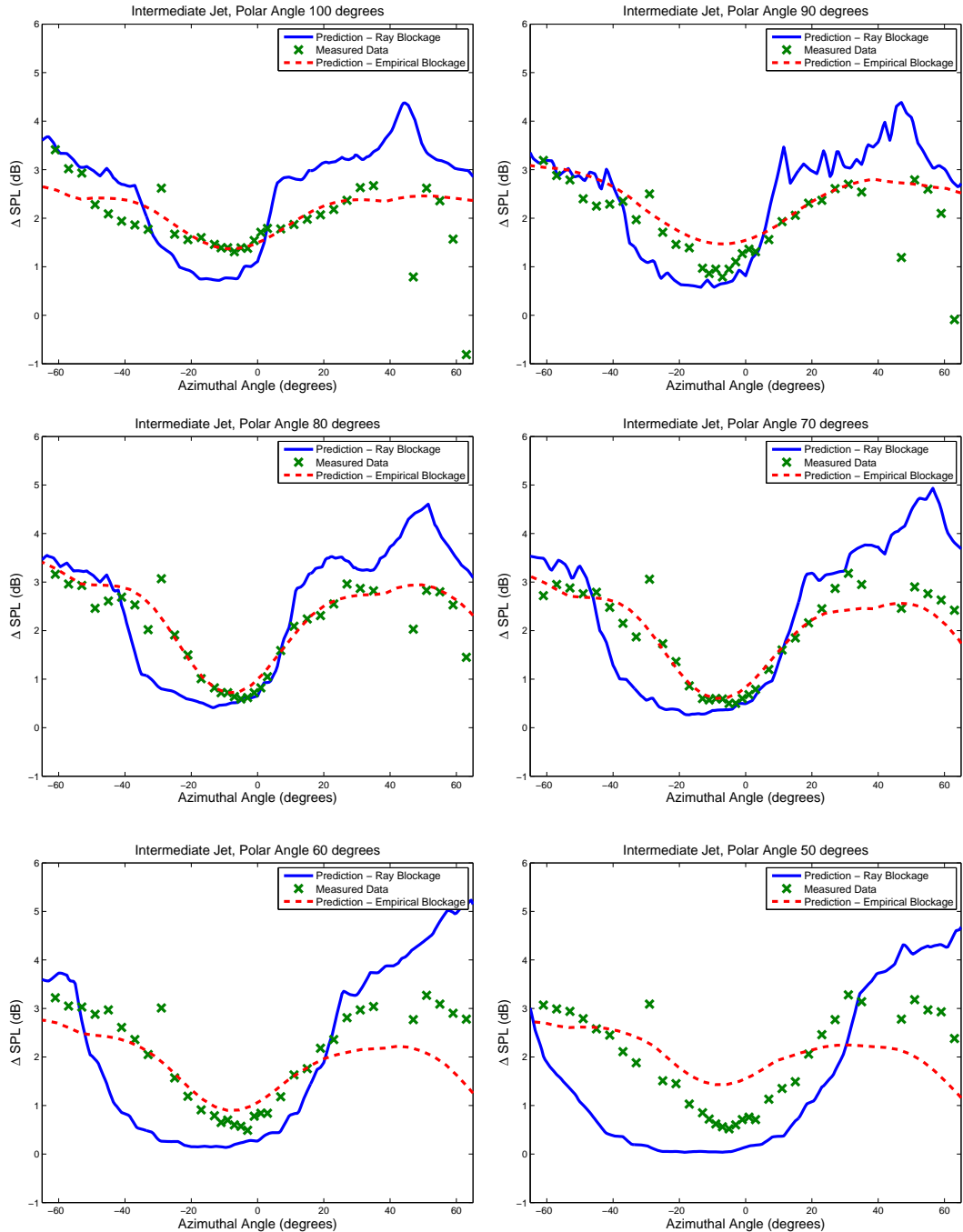


Figure 6.23 – Installation predictions with a ‘rayJet3D’ blockage model and an empirical blockage model compared with data from ANDANTE experiment 2, for ‘Intermediate’ Jet.

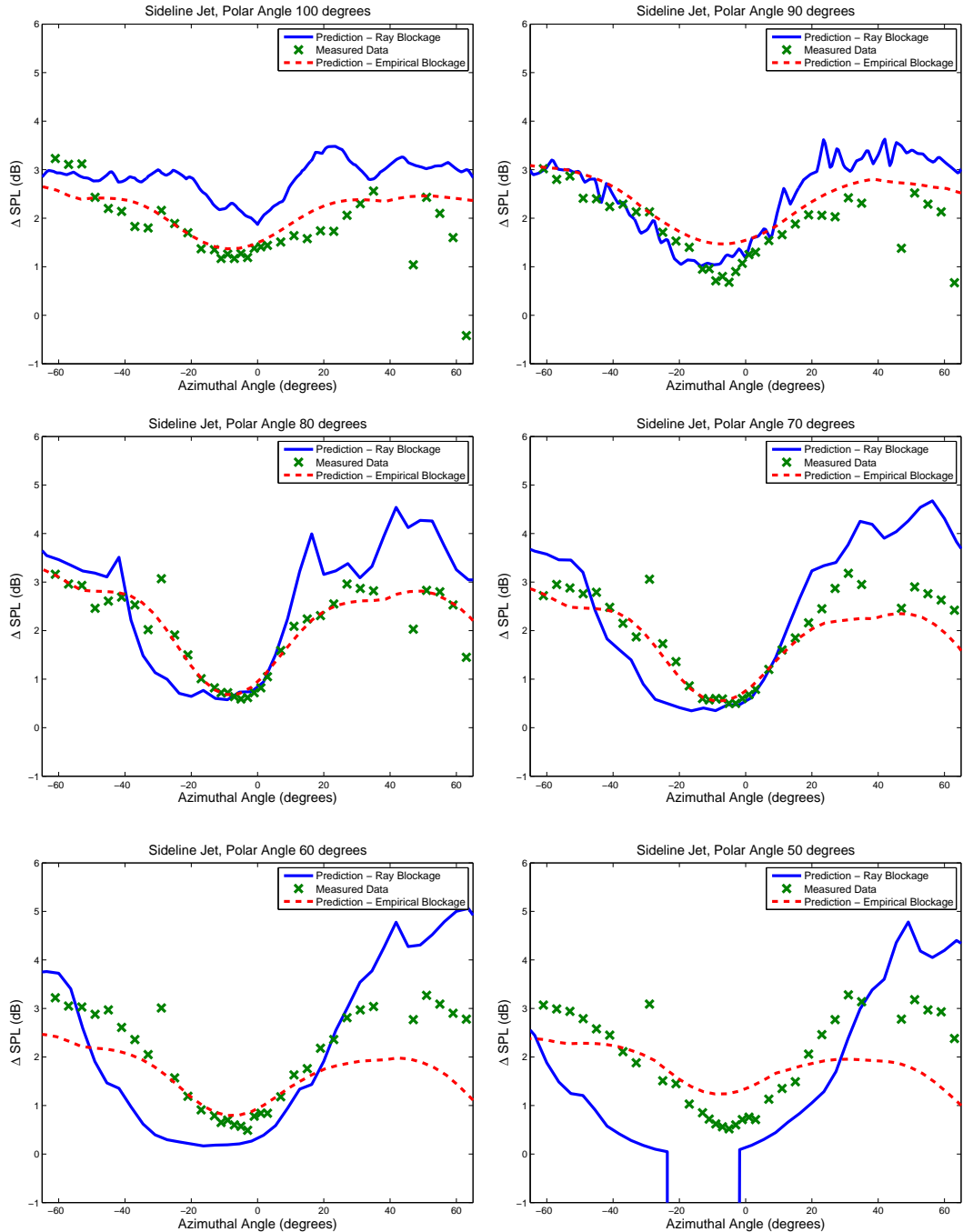


Figure 6.24 – Installation predictions with a ‘rayJet3D’ blockage model and an empirical blockage model compared with data from ANDANTE experiment 2, for ‘Sideline’ Jet.

6.15 Conclusions

In this chapter we have developed acoustic ray theory, by deriving the ray tracing equations from a wave equation. Ray theory is derived from the leading order term of a pressure power series, expanded in terms of inverse frequency, also known as a WKB ansatz. The power series is in terms of inverse frequency which makes using the leading order term, or ray theory, a good approximation to full wave equation solution at high frequencies, as it is known to break down when the length scale of the shear layer is comparable with the wavelength.

We have demonstrated how we can use ray theory to develop a acoustic propagation method for jet flows, using a monopole source which can be inside or outside the jet. The methodology has been developed using a 2-D ray code, which has been benchmarked using a Lilley equation solution, for a parallel sheared flow.

The advantage of the ray solution is that it makes fewer assumptions about the nature of the flow. The Lilley solution assumes that the flow is parallel, however the ray code we have developed can determine acoustic propagation through any type of mean flow.

Using the 2D ray code, we have investigated the significance of the parallel jet assumption, by tracing rays through a spreading jet and comparing the solution with an equivalent parallel jet, and found that the most significant difference was at low polar angles. In fact the spreading jet has a significant effect on the cone of silence angle.

A fully 3D jet propagation ray code has been developed and again benchmarked with the Lilley solution for a parallel isothermal jet. The 3D ray code is computationally expensive, however it has the advantage that it is a full farfield solution. The other major limitation of the ray code is that it is restricted to the high frequency limit, however this is something that we have to accept if we want to deal with realistic jets.

The 3-D jet propagation ray code has been integrated with a number of CFD profiles, using realistic jet nozzles, and benchmarked using data from the Andante external loud speaker experiment.

The 3-D ray code has been integrated with jet wing reflection prediction method from chapter 4, replacing the semi-empirical blockage model, and benchmarked using data from the Andante jet wing reflection experiments.

Chapter 7

Conclusions and Future

Work

In this thesis the problem of aircraft noise has been introduced and the importance of understanding jet noise installation effects has been highlighted. The requirement of this research project was to understand and predict jet noise installation effects for jets mounted below aircraft wings. This requires an understanding of the jet as a noise source. In chapter 2 the topic of jet flow and the jet noise source was reviewed. The jet source distribution, directivity and spectrum are examined. An original jet source model suitable for the purposes of modeling jet noise installation effects was derived in chapter 3.

In Chapter 4 existing installation effects experimental research was reviewed. Data from a novel set of model scale jet noise installation effects was reviewed. Data was measured on a traversing azimuthal array for a large range of polar and azimuthal angles. The effects of jet blockage and redistribution of energy due to refraction by the jet were examined using a point source external to the jet, for a range of realistic jet operating conditions. The change in radiated noise levels caused by placing a jet beneath a wing were examined, again for a range of realistic jet operating conditions.

In Chapter 5 existing engine noise installation effects models were reviewed. The development of an engineering tool for the prediction of 3D installation effects on jet noise in the presence of a wing has been described, using a ray based model. This chapter also includes the development of a semi-empirical jet blockage model for a point source. The installations model was validated using experimental data reviewed in Chapter 2. The model was shown to make fast and accurate predictions for a complex problem. However given that the method is semi-empirical the predictions are limited to the extent of the database.

In Chapter 6 acoustic ray theory was derived from a convected wave equation. The development of an acoustic propagation method for jet flows was described. The methodology was developed using a 2-D ray code, which was benchmarked using a Lilley equation solution. Based on this methodology a fully 3D acoustic propagation ray code was described and benchmarked for an infinite parallel isothermal jet using a Lilley equation solution. The ray code was then integrated with more realistic CFD jet flow profiles and benchmarked using experimental data. Finally the 3D ray code was used to provide a jet blockage model for the installations prediction method of Chapter 5.

Using the ray technique to account for refraction by the jet has proven to be a powerful tool, in that it can provide solutions for realistic complex jet flow profiles. On the down side the method is computationally expensive and limited to high frequency. This method is probably best suited as a tool to investigate novel jet flow profiles, or equally as method to extend the blockage database for the semi-empirical installation effects prediction tool.

7.1 Future Work

There are a number of possible avenues for continuation of the work that has been carried out for this thesis.

The semi-empirical method outlined in chapter 5 can be continued to be developed. The database upon which the jet source directivity, distribution and blockage model can be extended to include more jet conditions and different jet nozzles.

The model could be developed to include a more detailed aircraft geometry, including different flap setting and the fuselage. The surface curvature of the wing could be modeled.

One important development of the 3D ray method would be to include reflection from solid bodies. This would allow for inclusion of the jet nozzle, and we could investigate acoustic scattering by the nozzle. It would also allow us to do a installation effects calculation with the jet sources in the jet propagating out and reflecting from the wing and of course being refracted again by the jet.

The 3D jet propagation ray method developed in Chapter 6 has a number of different applications other than installation effects. At the ISVR this code is currently being used to develop noise models for non-axisymmetric jets using a RANS and acoustic analogy method. It also has application to jet shear propagation problems and flight stream parameter studies.

Appendix A

A.1 ANDANTE Wing

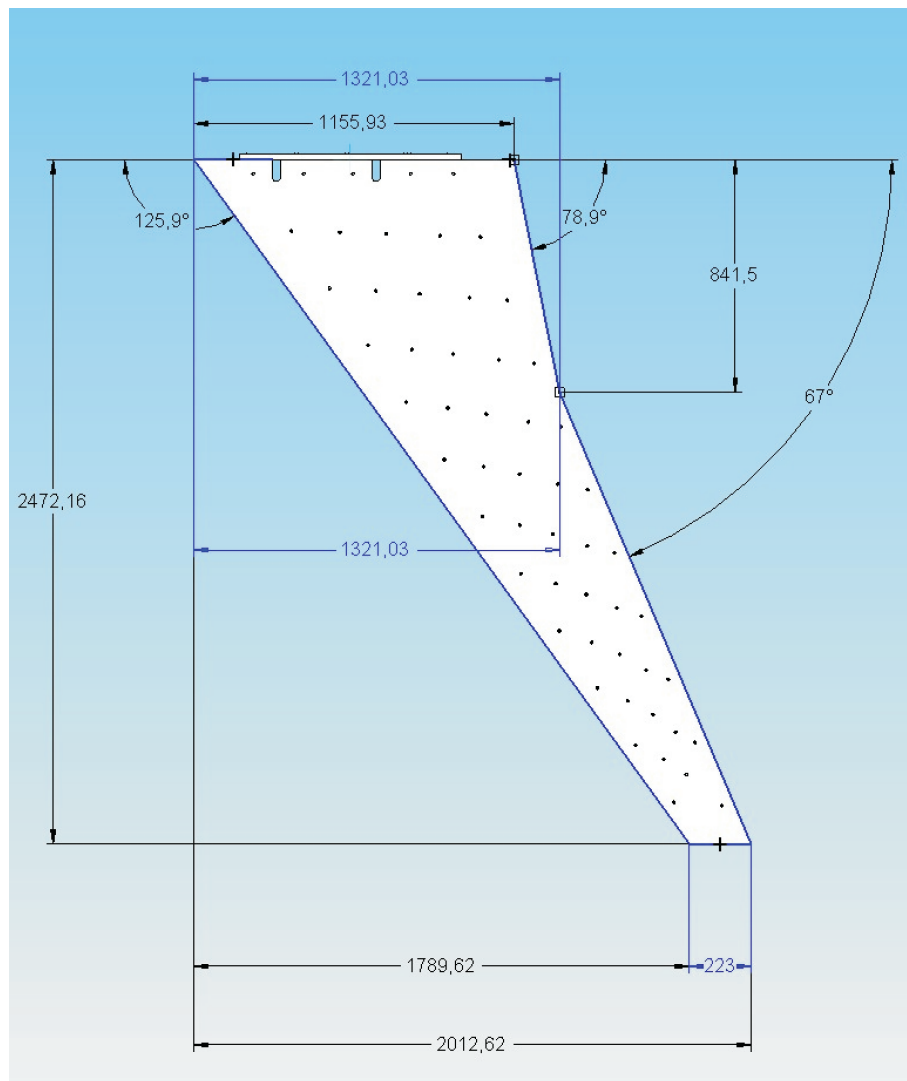


Figure A.1 – Schematic of Flat Plate Wing manufactured for and used in the Andante Installations Tests.

A.2 CFD

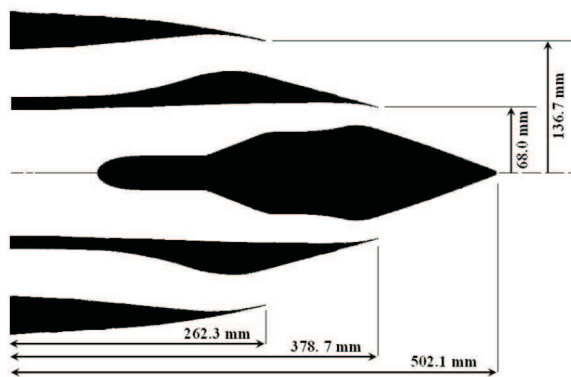


Figure A.2 – Short Cowl Nozzle used for CFD.

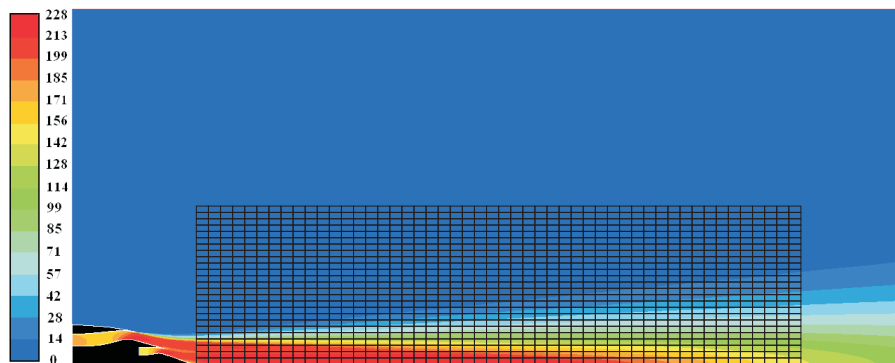


Figure A.3 – Grid on which CFD data is projected onto.

A.3 Sensitivity Study

To determine source sensitivity to discretization a study was conducted for both the line and ring source distributions. While undertaking the sensitivity study, it was noted that the numerical convergence was largely independent of microphone position and Strouhal number. Thus both sensitivity studies shown are for a jet with Strouhal number 2.48, using a microphone at azimuthal angle of 55°.

Firstly to determine the number of axial sources required, the jet was approximated to a line of point sources, distributed over ten nozzle diameters, along the centerline of jet axis. Figure A.4 shows the ΔSPL at a single microphone position for a simple reflection from a flat plate plotted against the number of sources used. As can be seen from the graph the solutions converge rapidly with minimal variation after about 80 sources. To err on the side of caution it was decided to approximate the jet axially by 100 discrete sources in subsequent calculations.

Next using 100 axial stations, the source at each of these was assumed to take the form of a continuous ring (diameter equal to the outer nozzle diameter) and each of these ring sources was then discretized. Figure A.5 plots the number of sources used per ring against ΔSPL for a single microphone position, note the different scales between figures A.4 and A.5.

As expected the number of axial stations used is an important parameter and it is necessary to use quite a high number in the discretization if accurate results are to be achieved, but somewhat surprisingly, the results are far less sensitive to the ring source distribution used. However, we recall that a classic exercise in potential theory shows that a spherical source distribution (spreading spherically) produces an exterior field identical to that produced when the entire source is concentrated at the centre point of the sphere, and a similar averaging principle applies here. This is important because it indicates that the axial distribution is far more important than the details of

the radial distribution and this in turn implies that measurement techniques such as Polar Correlation (that assume a 1-d distribution) can be used with confidence in calculations of this type. However, it should be noted that during this exercise hot jet blockage was not considered and this may negate this conclusion somewhat.

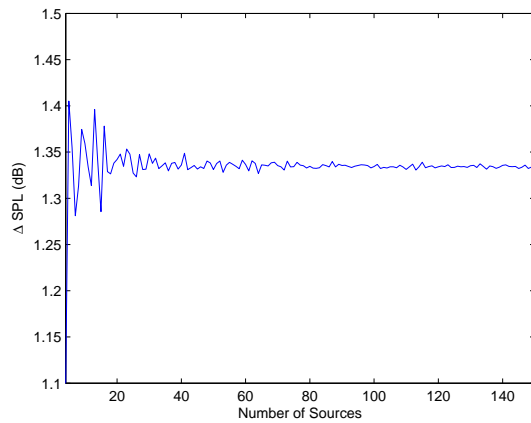


Figure A.4 – Example of convergence for a ring source distribution.

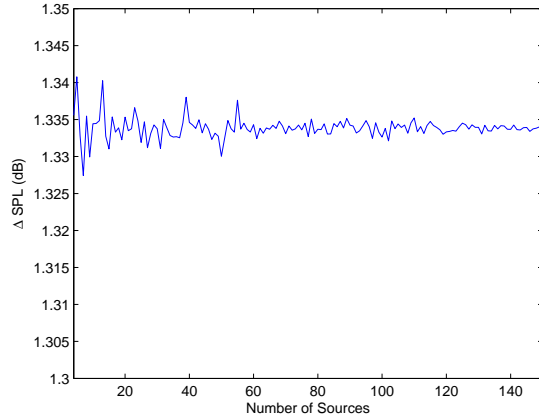


Figure A.5 – Example of convergence for a line source distribution..

Bibliography

- [1] Capp S. Hussein H.J. and W.K. George. Velocity measurements in a high-reynolds-number, momentum conserving, axisymmetric, turbulent jet. *Journal of Fluid Mechanics*, 258:31–75, 1994.
- [2] Wygnanski I. and H. Fielder. Some measurements in the self-preserving jet. *Journal of Fluid Mechanics*, 38:577–612, 1969.
- [3] International Civil Aviation Authority Environmental Report 2007. 2007.
- [4] R Mani. Noise due to interaction of inlet turbulence with isolated stators and rotors. *Journal of Sound and Vibration*, 17(2):251–260, 1971.
- [5] S Glegg. Broadband noise from ducted prop fans. *AIAA-1993-4402*, 1993.
- [6] Bushell K.W. Measurement and prediction of jet noise in flight. *AIAA*, 461, 1975.
- [7] Szewczyk V.M. Coaxial jet noise in flight. *AIAA*, 636, 1979.
- [8] Turner B.A. Way D.J. Model tests demonstrating underwing installation effects on engine exhaust noise. *AIAA*, 80-1048, 1980.
- [9] Wang M.E. Wing effect on jet noise propagation. *AIAA*, 80-1047, 1980.

- [10] Shivashankara B.N. and Blackner A.M. Installed jet noise. *AIAA*, 97-1601, 1997.
- [11] C. J. Mead and P. J. R. Strange. Under-wing installation effects on jet noise at sideline. *AIAA 98-2207*, June 1998.
- [12] A. Moore. A 3d prediction of the wing reflection of aero engine noise. *AIAA-2004-2865*, May 2004.
- [13] A. Moore and C. J. Mead. Reflection of noise from aero engines installed under an aircraft wing. *AIAA-2003-3151*, May 2003.
- [14] Berton J.J. Noise reduction potential of large, over-the-wing mounted, advanced turbofan engines. *NASA Publication*, 2000-210025, 2000.
- [15] Ricouard J. Chappuis J. and M. Roger. Aft fan noise shielding by a lifting surface: analytical, numerical and experimental results. *AIAA*, 2006-2617, 2006.
- [16] Gerhold C.H. Clark L.R. Inlet noise reduction by shielding for the blended-wing-body airplane. *AIAA*, 1999-1937, 1999.
- [17] Dunn M.H. Gerhold C.H., Clark L.R. and Tweed J. Investigation of acoustic shielding by a wedge-shaped airframe. *AIAA*, 2004-2866, 2004.
- [18] Shin H-C. Agarwal A., Dowling A.P. and Graham W. Ray-tracing approach to calculate acoustic shielding by a flying wing airframe. *AIAA*, 45(5):1080, 2007.
- [19] Z. angew. Prandtl, L. *Math. Mech.*, 5:136139, 1925.
- [20] B. Pope, S. *Turbulent Flows*. Cambridge University Press, Cambridge, 2000.

- [21] Panchapakesan N.R. and J.L. Lumley. Turbulence measurements in axisymmetric jets of air and helium. part 1. air jet. *Journal of Fluid Mechanics*, 246:197–223, 1993.
- [22] M.E. Goldstein. *Aeroacoustics*. McGraw-Hill, New York, 1976.
- [23] M.J. Lighthill. On sound generated aerodynamically. i. general theory. *Proc. R. Soc. Lond.*, 211(3):564–587, March 20, 1952.
- [24] R. Dorsch Karachmer, A. and R. Friedman. Acoustic Tests of 15.2 centimeters diameter potential flow nozzle. *NASA TR 1292*, 1974.
- [25] P.A. Lush. Measurements of subsonic jet noise and comparison with theory. *Journal of Fluid Mechanics*, 46(3):477–500, 1971.
- [26] Gutierrez Olsen, W.A. and R.G. Dorsch. The Effect of Nozzle Inlet Shape, Lip Thickness, and Exit Shape and Size on Subsonic Jet Noise. *NASA, TM X-68482*, 1973.
- [27] Tester B.J. and Morfey C.L. Developments in jet noise modeling theoretical predictions and comparisons with measured data. *Journal of Sound and Vibration*, 46:79–103, 1976.
- [28] C J Powles and B J Tester. Asymptotic and numerical solutions for shielding of noise sources by parallel coaxial jet flows. *AIAA-2008-2975*, May 2008.
- [29] ESDU. Computer-based estimation procedure for single-stream jet noise. including far-field, static jet mixing noise database for circular nozzles.s. ESDU 98019 B:0, 2007.
- [30] Stone J.R. and Montegani F.J. An improved prediction method for the noise generated in flight by circular jets. *NASA, TM - 81470*, 1980.

- [31] Preston G.A. Fisher M.J. and Bryce W.D. A modelling of the noise from simple coaxial jets, part i: With unheated primary flow. *Journal of Sound and Vibration*, 209:385–403, 1998.
- [32] Preston G.A. Fisher M.J. and Bryce W.D. A modelling of the noise from simple coaxial jets, part ii: With heated primary flow. *Journal of Sound and Vibration*, 209:405–417, 1998.
- [33] Ko N.W.M. and A.S.H. Kwan. The initial region of subsonic coaxial jets. *Journal of Fluid Mechanics*, 73:305–332, 1976.
- [34] R. H. Self and A. Bassetti. A rans based jet noise prediction scheme. *AIAA 2003-3325*, page 0, 2003.
- [35] M. Hossain R. H. Self G. J. Page, J. J. McGuirk and A. Bassetti. A cfd coupled acoustics approach for coaxial jet noise. *AIAA 2003-3286*, page 0, 2003.
- [36] A. Uzun. 3-d large eddy simulation for jet aeroacoustics. *PhD thesis, Purdue University*, 2003.
- [37] S. K. Lele J. B. Freund and P. Moin. Direct numerical simulation of a mach 1.92 turbulent jet and its sound field. *AIAA*, 38:2023–2031, 2000.
- [38] C. L. Morfey. Amplification of aerodynamic noise by convected flow inhomogeneities. *Journal of Sound and Vibration*, 31:391–397, 1973.
- [39] Ffowcs Williams J.E. Dowling A.P. *Sound and Sources of Sound*. Ellis Horwood Limited, Chichester, 1983.
- [40] S. A. L. Glegg. Jet noise source location. *PhD thesis, Southampton University*, 1979.
- [41] M. Harper-Bourne M. J. Fisher and S. A. L. Glegg. Jet engine noise source location: The polar correlation technique. *Journal of Sound and Vibration*, 51:23–54, 1977.

- [42] P J R Strange A Moore P Mc Laughlin, R H Self. A 3-dimensional installation effect prediction method for a distributed jet source. *AIAA-2007*, May 2007.
- [43] Christopher Wrighton. Installation effects tests report. *ANDANTE Work Package 4.2*, 2008.
- [44] E.N. Bazley. Sound absorption in air at frequencies up to 100 khz. *Nat. Phys. Lab., Teddington, UK*, 74:75, 1976.
- [45] C J Powles and B J Tester. Installation effects study: Isvr study on jet shielding effect. *TURNEX - project report: 516079*, Nov 2007.
- [46] V. M. Szewczyk. The role of flow acoustic interaction noise in jet noise studies. *PhD Thesis, ISVR, University of Southampton*, 1978.
- [47] Deschamps G.A. Ray thechniques in electromagnetics,. *Proceeding of the IEEE*,, 60(9):1022–1035, 1972.
- [48] Sommerfeld A. and J. Runge. Anwendung der vektorrechnung auf die grundlagen der geometrischen optik,. *Ann. Phys.*, 35:277–298, 1911.
- [49] Blokhintzev D. The propagation of sound in an inhomogeneous and moving medium i. *The Journal of the Acoustical Society of America*, 18(2):322–328, 1945.
- [50] Keller J.B. Seckler B.D. Asymptotic theory of diffraction in inhomogeneous media. *The Journal of the Acoustical Society of America*, 31(2), 1959.
- [51] Keller J.B. Diffraction by a convex cylinder. *Electromagnetic Wave Theory Symposium*, pages 312–321, 1956.
- [52] Keller J.B. Diffraction by an aperture. *Journal of Applied Physics*, 28: 426–444, 1957.

- [53] Keller J.B. The geometrical theory of diffraction. *Symposium on Microwave Optics*, 1953.
- [54] Wundrow D.W. and A. Khavaran. On the applicability of high-frequency approximations to lilleys equation. *Journal of Sound and Vibration*, 272:793–830, 2004.
- [55] Gerhold C.H. Analytical model of jet shielding. *AIAA*, 21:694–698, 1982.
- [56] C L Morfey and P F Joseph. Shear-layer refraction corrections for off-axis sources in a jet flow. *Journal of Sound and Vibration*, 239:819–848, 2001.
- [57] Suzuki T. and Lele S.K. Refracted arrival waves in a zone of silence from a finite thickness mixing layer. *Acoustical Society of America*, 111, 2002.
- [58] Freund J.B. and Fleischman T.G. Ray traces through unsteady jet turbulence. *International Journal of Aeroacoustics*, 1:83–96, 2002.
- [59] Shur M.L. Spalart P.R. and Strelets M.Kh. Identification of sound sources in large-eddy simulations of jet. *AIAA-2007-3616*, 2007.
- [60] Fratello D.J. Yu J.C. Measurement of acoustic shielding by a turbulent jet. *Journal of Sound and Vibration*, 98(2):183–212, 1985.
- [61] Durbin P.A. High frequency green function for aerodynamic noise in moving media, part i: General theory. *Journal of Sound and Vibration*, 91(4):519–525, 1983.
- [62] Durbin P.A. High frequency green function for aerodynamic noise in moving media, part ii: Noise from a spreading jet. *Journal of Sound and Vibration*, 91(4):527–538, 1983.

- [63] Ingard K.U. Morse P.M. *Theoretical acoustics*. Princeton University Press, Princeton, New Jersey, 1986.
- [64] Pierce. *Acoustics, An Introduction to its Physical Principles and Applications*. American Institute of Physics, New York, 3rd ed edition, 1994.
- [65] C Powles. Asymptotic and numerical solutions for shielding of noise sources by parallel coaxial jet flows. *ISVR, Technical Report*, Feb 2010.
- [66] M Azarpeyvand. Some aspects of rans based jet noise prediction. *PhD Thesis, University of Southampton, Faculty of Engineering, Science and Mathematics, Institute of Sound and Vibration Research*, October 2008.
- [67] Tan S.Y. and Tan H.S. Modelling and measurements of channel impulse response for indoor wireless communication system design. *IEE, Proceedings on Microwave, Antennas, and Propagation.*, 142(6):405–410, 1995.
- [68] G. Durgin, N. Patwari, and T.S. Rappaport. Improved 3d ray launching method for wireless propagation prediction. *Electronics Letters*, 33(16):1412–1413, 1997.
- [69] W.T. Vetterling B.P. Flannery W.H. Press, S.A. Teukolsky. *Numerical Recipes in Fortran 90*. Cambridge University Press, Cambridge, 1996.